論文 / 著書情報
Article / Book Information

題目(和文)	拡張節点勾配型有限要素法とその破壊力学問題への応用
Title(English)	Extended nodal gradient finite elements and their application to fracture mechanics problems
著者(和文)	コウ サクイ
Author(English)	Zuoyi Kang
出典(和文)	学位:博士(工学), 学位授与機関:東京工業大学, 報告番号:甲第10671号, 授与年月日:2017年9月20日, 学位の種別:課程博士, 審査員:廣瀬 壮一,天谷 賢治,三上 貴正,WIJEYEWICKREMA ANIL,佐々木 栄一,BUI QUOC TINH
Citation(English)	Degree:Doctor (Engineering), Conferring organization: Tokyo Institute of Technology, Report number:甲第10671号, Conferred date:2017/9/20, Degree Type:Course doctor, Examiner:,,,,,
学位種別(和文)	博士論文
Type(English)	Doctoral Thesis

Extended Nodal Gradient Finite Elements and Their Application to Fracture Mechanics Problems

by

KANG Zuoyi

Supervisor: Professor Sohichi Hirose

A dissertation submitted in partial fulfillment of the requirement for the degree of

Doctor of Engineering

Department of Mechanical and Environmental Informatics
Graduate School of Information Science and Engineering
Tokyo Institute of Technology
Tokyo, Japan

August 2017

ABSTRACT

Defects or cracks greatly affect the performance and strength of engineering structures and materials in many technical areas including civil, infrastructures, aerospace, automotive, and marine. A better understanding of fracture behaviors of engineering structures and materials is essential in the design, development and maintenance of engineering applications. Solutions of fracture problems are usually derived from experiments, analytical, and numerical methods. Experiments however often require a high cost while the analytical methods are valid only for problems with simple configuration and boundary and loading conditions. The numerical methods like the finite element method (FEM) are often chosen for practical purpose. Although the FEM has shown to be an effective method in solving problems with smooth solutions, mesh refinement is necessary along the crack which makes the FEM very time-consuming and ineffective in dealing with the evolution of cracks. Extended finite element method (XFEM) becomes a powerful computational method for modelling discontinuities without remeshing.

This research presents an effective finite element approach based on enrichment and consecutive-interpolation procedure (CIP) for solving fracture issues in 2D elastic. The approximation functions constructed based on the CIP, which differs from the traditional methods, involve both nodal values and averaged nodal gradients as interpolation conditions. The difficulty of meshing issues and the post-processing of stress recovery are hence no longer required. The accuracy and performance of the proposed XCQ4 and its numerical properties are illustrated through numerical examples, considering both single and mixed-mode problems with complicated configurations. Compared with reference solutions available in the literature and the conventional XFEM results, it is found that the accuracy of the XCQ4 is higher and the XCQ4 can manage the relative error below 1% even though the coarse mesh discretization.

Studies on the convergence rate of the stress intensity factors (SIFs) in relative errors also reveal a better performance of the XCQ4 over the classical XFEM. The fracture parameters are found to be stable for different areas of integration paths around the crack tip. Further applications of the developed XCQ4 to other complex problems are potential.

Upon the achievement of the performance of XCQ4 in mixed mode fracture problem, the implementation of the XCQ4 for crack propagation is evaluated. In this work, the discontinuous Heaviside function is taken to treat the discontinuity cut by crack, while the asymptotic crack-tip branch functions are embedded into the approximation functions to capture the singular field at the crack tips. As an alternative way of capturing the singular field at the crack tip, another version of enrichment function, called the ramp function, along with the Heaviside function is taken into account. We consider to integrate the ramp functions into both the standard XFEM using 4-node quadrilateral element (XQ4) and the developed XCQ4. The SIFs calculated by using both approaches, the ramp function with XCQ4 and with XQ4, are validated against reference solutions and can be found in the numerical examples. We integrate the interaction integral in terms of J-domain to estimate the fracture parameters, and adopt the maximum hoop stress criterion to determine the direction of crack evolution. Several representative examples in 2D elastic solids are considered to show the accuracy and performance of the present approach. Compared with the reference solution, the proposed XCQ4 method is capable of achieving high precision in SIFs calculation and predicting the crack paths accurately.

To develop the XCQ4 algorithm to analyze the dynamic fracture response in isotropic and anisotropic materials, the prediction of dynamic SIFs (DSIFs) time history for both single and mixed-mode fracture problems is investigated in this work based on the previous achievements. For orthotropic material, versatile crack tip enrichment functions spanning all possible displacement states are adopted and fracture mechanics for two-dimensional orthotropic material is briefly introduced. In addition, the time-dependent discrete equations are solved using Newmark time integration without considering damping matrix. The numerical values of DSIFs are extracted according to interaction integral taking into account inertial effect. The time history of DSIFs derived from XCQ4 for isotropic and anisotropic solids are verified with respect to reference solutions reported in open literature.

The new approach is further extended to the numerical analysis of fluid flow in fractured porous media. The coupled deformation and fluid flow in fractured porous media has been simulated by the present XCQ4 approach. Through introducing the transfer function that mathematically demonstrates the flow interaction between the porous matrix and existing fracture, the pore fluid pressure is simulated in terms of Biot’s theory which accounts for the fluid flow inside both matrix and fracture domain, and the numerical results show the robustness of XCQ4 for solving fracture behavior in saturated fractured porous media.

The applicability of developed XCQ4 technique was successfully verified through several numerical validations. It is found that the new numerical method is suitable for solving the fracture problems and the satisfactory numerical results can be achieved, which reflects the value and reliability of XCQ4.

ACKNOWLEDGEMENTS

I would like to express my sincere appreciation to Professor Sohichi Hirose for his considerable support and concern to my doctoral life. His constructive advices and fruitful instructions always keep me confident to overcome the difficulty on the road to a brilliant future. His patience and kindness directs me a way to grow and makes me determined. I am most grateful for the guidance, encouragement and discussion with Specially Appointed Associate Professor Quoc Tinh Bui. I was sustained by him to make progress with the coding of the extended finite element scheme and the comprehension regarding fracture mechanics. I pretty cherish the past four years and am honored to be a member of the laboratory.

I wish to thank Associate Professor Mao Kurumatani from the Department of Civil Engineering, Ibaraki University and Assistant Professor Yuki Onishi from the Department of Mechanical and Environmental Informatics, Tokyo Institute of Technology, with whom I have had an admirable Off-lab discussion related to the modification of my research content. Their exclusive viewpoints and perceptions make me fresh and broadened my horizons.

Furthermore, I gratefully acknowledge the defense committee members: Professor Kenji Amaya, Associate Professor Eiichi Sasaki, Associate Professor Anil C. Wijeyewickrema and Associate Professor Takamasa Mikami, for their time and effort on reviewing my doctor thesis and providing pragmatic comments and recommendations.

A great thanks to members of Hirose laboratory for many interesting discussion about academic research during the four year at Tokyo Tech. Particularly, Assistant Professor Akira Furukawa affords me plentiful concern and pleasure to me in the study and daily life. Also, a sincere thanks to Dr. Maruyama, Dr. Shen, Mr. Tuan and the secretary of the laboratory Ms. Sugawara for their assistances and efforts.

Without the external funding the stay at Tokyo Tech, my participation in international conference and paper publication could not have been realized. I therefore wish to thank the scholarship from Monbukagakusho.

Finally, I would like to express my heartfelt gratitude to my wife and parents for their endless love and keeping me company all the time.

List of Symbols

Symbol	Description
$\mathbf{x} = (\mathrm{x}, \mathrm{y})$	Point of interest in 2D space
$\widetilde{N}_f$	Consecutive-interpolation shape functions
$N_f^{[i]}, L_i$	Standard shape function at node i
$N_{f,x}^{[i][e]}$	Derivative of standard shape function at node i
$\overline{N}_{f,x}^{[i]}$	Average derivative of standard shape function at node i
$N_f^{[i]}$	Element
d_f	Nodal displacement
n_s	Total number of supporting nodes
w_e	Weight function of element
Δ_e	Area of element
$\phi_i, \phi_{ix}, \phi_{iy}$	Polynomial basis
I^s	Total nodes
J^{cut}	Enriched nodes in element cut by crack completely
K^{tip}	Enriched nodes in element containing crack tip
$\mathbf{u}_i$	Vector of standard nodal degrees of freedom
$\mathbf{a}_i$	Vector of additional nodal degrees of freedom
$\mathbf{b}_k^{\alpha}$	Vector of additional nodal degrees of freedom
$H(\mathbf{x})$	Heaviside function
$F^{\alpha}(\mathbf{x})$	Crack-tip branch function for displacement field
$B_{\alpha}(\mathbf{x})$	Crack-tip enrichment function for pressure field
$\bar{J}(\mathbf{x})$	Heaviside-junction enrichment of crack
$\phi(\mathbf{x})$	Signed distance function
$f^n(\mathbf{x})$	Signed distance function of the minor crack

$f^N(\mathbf{x})$	Signed distance function of the main crack
$R(\mathbf{x})$	Ramp function
$q(\mathbf{x})$	Smoothed weight function
Δt	Time interval
C_d	Longitudinal wave speed
σ_o	Initial stress
(K_I, K_{II})	Stress intensity factors
(K_I^*, K_{II}^*)	Normalized stress intensity factors
$\mathbf{K}_m$	Matrix Permeability
$\mathbf{K}_f$	Fracture Permeability
P^m	Water pressure of matrix domain
P^f	Water pressure of fracture domain
$\mathbf{m}$	Identity tensor
K_w	Bulk modulus of pore flow
K_s	Bulk modulus of grain material
K_T	Bulk modulus of skeleton
$\widetilde{N}_u$	Consecutive-interpolation shape function for displacement
$\widetilde{N}_p$	Consecutive-interpolation shape function for Pressure
n	Porosity of matrix rock
ρ	Density
T	Transfer function
μ_w	Pore fluid viscosity
α	Biot coefficient
(ξ, η)	Natural coordinate system
$(\tilde{\xi}, \tilde{\eta})$	Local natural coordinate system
(r, θ)	Polar coordinate at crack-tip
l_c	Segmental crack length
$\boldsymbol{\sigma}$	Total stress tensor
$\boldsymbol{\sigma}''$	Effective stress tensor
$\boldsymbol{\epsilon}$	Strain tensor
$\boldsymbol{C}$	Elastic material tensor
$\mathbf{K}$	Global stiffness matrix

$\mathbf{M}$	Global mass matrix
$\mathbf{F}$	Vector of external nodal force
$\mathbf{B}$	Strain matrix operator
$\dot{\mathbf{u}}$	Vector of nodal velocity
$\ddot{\mathbf{u}}$	Vector of nodal acceleration
$\bar{\mathbf{t}}$	Prescribed traction
$\bar{\mathbf{b}}$	Body force
$\mathbf{n}$	Unit normal vector
Re	Relative error
a/W	Crack-length-width ratio
$M^{(1,2)}$	Interaction integral
W_s	Strain energy density
R	J-integral domain radius
E	Young’s modulus
G	Shear modulus
ν	Poisson’s ratio
σ	Tensile load
τ	Shear load
θ_c	Crack growth direction
$\bar{r}$	Shape factor

TABLE OF CONTENTS

CHAPTER 1

INTRODUCTION

1.1 Background

Accurate numerical modeling of crack tip field remains a challenging problem in computational fracture mechanics. The accurate prediction of the singular stress fields near the crack tip plays a crucial role in maintenance, life prediction and safety assessment of advanced engineering materials and structures. Many approaches including analytical, semi-analytical, experimental, numerical methods, etc. have been introduced and developed for fracture modeling over the past few decades. In terms of the numerical approaches, the finite element method (FEM) is a powerful tool as it has been extensively used for solving a variety of engineering problems. By using special elements such as singular crack-tip elements [Kwon et al., 1989], enriched elements [Gifford et al., 1978], etc., the FEM can be applied for extracting the stress intensity factors, but it is found to be very cumbersome in modeling of the evolution of crack. One of the main reasons lies in the fact that the element edges must be conformed to the finite element meshes. However, it further requires the mesh to be re-meshing during the propagation of crack, by which the crack geometry can hence be captured consistently. In other words, the element topologies must be updated appropriately throughout the re-meshing procedure. In addition, a smoothing operation employed for stresses recovery at the post-processing state is often required by the FEM. Therefore, much efforts have been done to develop new or improved numerical techniques to facilitate or overcome the difficulties in the classical methods, for example, the extended finite element method (XFEM) [Moës et al., 1999; Yu et al., 2016; Bui et al. 2012], meshfree methods [Racz et al., 2012], smoothed FEM [Liu et al., 2012], extended isogeometric analysis [Bhardwaj et al., 2015; Bui et al., 2015; Yin et al., 2015], radial integration method-based BEM [Hematiyan et al., 2013], just to name a few. In this work, a novel accurate extended 4-node element with smooth nodal stresses is presented, which successfully addresses the difficult issues of the standard FEM.

The extended finite element method (XFEM) [Belytschko et al., 1999] becomes an effective and accurate technique for fracture modeling. The beauty of the XFEM lies in the fact that the discontinuity and singularity induced by crack are effectively treated as the mesh is completely independent of the crack geometry as shown in Fig. 1.1, and more interestingly the re-meshing in crack propagation is no longer required. Basically, it is achieved by accomplishing the coupling of both the discontinuous fields and the near tip asymptotic fields through a partition of unity method [Babuska et al., 1997; Fries et al., 2010]. The XFEM has been successfully applied to solve a wide range of engineering problems, and for more information interested readers may refer to a recently published monograph comprehensively made by [Khoei, 2015]. Despite it gains a clear general progress with the standard XFEM, there are still many technical issues pertaining to its further improvements and applications in modeling fracture problems. For instance, a modification of the standard enrichment method for better capturing the discontinuities cut by crack is developed by [Belytschko et al. 2003];

[Stazi et al., 2003] and [Bechet et al., 2005] introduced a new enrichment method, the geometrical enrichment, which is another enrichment technique in contrast to the standard topological enrichment [Moës et al., 1999]. Generally the XFEM using the geometrical enrichment can further enhance the accuracy of the stress fields near crack tip; or [Fries et al., 2008] proposed the so-called blending element, which is to overcome the less accuracy of the standard method to the enrichment area at the crack tips; and many others.

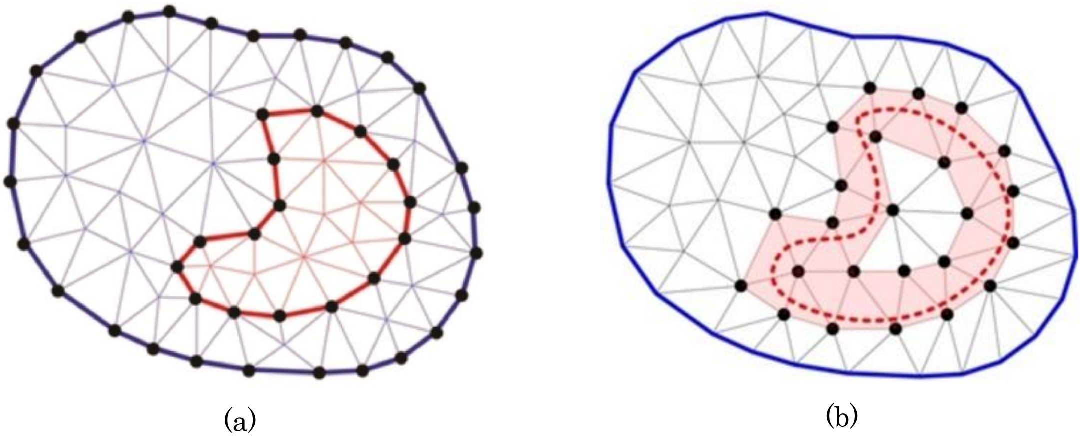
(a) (b)

Fig. 1.1 Process of fracture mesh inside the framework of (a) FEM and (b) XFEM.

Although the FEM has been successfully applied to a wide range of engineering problems in many fields, but it is well-known that the gradients of field variables by means of the FEM are discontinuous among internal element edges. Such discontinuity also happens at the nodes. In practice, an extra task of the smoothing operation to the nodal stress in the post-processing procedure is often required. In recent years, [Zheng et al., 2010] presented an improved triangular element for elastostatic problems in which the new concept of the twice-interpolation procedure acting on the interpolation functions is proposed. The new triangular element is very attractive and interesting as it owns various desirable features that are not available in the standard elements. By employing this new triangular element, not only the continuous nodal stress can be gained as the need for smoothing operation is not required, but the accuracy of the solutions is also found to be higher than that derived from the standard triangular element. The main idea behind the method comes from the approximation functions based on the twice-interpolation procedure. Basically the approximation functions handle both the nodal values and the averaged nodal gradients as interpolation conditions, see [Zheng et al., 2010] for detail. Later, a singular element by means of the twice-interpolation method is developed by [Wu et al., 2012] for crack propagation in 2D elastic solids. Recently, [Yang et al., 2014] proposed a three-node triangular element with continuous nodal stress. The element proposed by [Yang et al., 2014] is interesting but their formulation is completely different from the twice-interpolation based element [Zheng et al., 2010; Wu et al., 2012], as a result of applying the idea of the previous partition-of-unity based FE-Meshless quadrilateral element. It must be stressed here that the present extended 4-node element does not follow the approach addressed in [Yang et al., 2014].

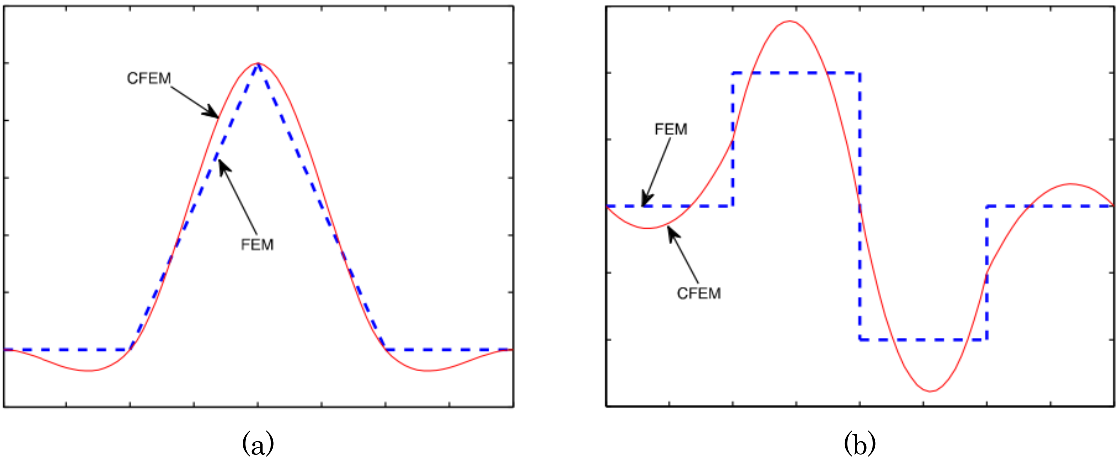

(a) (b)

Fig. 1.2 Comparison of the CFEM and FEM shape function (a) and their first-order derivatives (b).

Recently, [Bui et al., 2014] successfully formulated a new 4-node quadrilateral element with continuous nodal stress by applying the concept of the twice-interpolation procedure to the standard 4-node quadrilateral element for stress analysis of 2D elastic solids. Notice that the term “twice-interpolation” has been replaced by a different name as “consecutive-interpolation” in this work for a better representation as visualized in Fig. 1.2. Consequently the consecutive-interpolation 4-node quadrilateral element (CQ4) is thus born. In a similar fashion the CQ4 element also owns a number of desirable features of an accurate numerical method. Those advantages have already pointed out and curious readers may simply find them in [Bui et al., 2014]. Generally the basic functions for the CQ4 element are constructed in two stages. The same interpolation function as in the common FEM for the 4-node quadrilateral element is first constructed. Subsequently, the interpolation function constructed by the first step is then extended to involve both the nodal values and averaged values of gradients of the unknowns at the nodes.

Nevertheless, the major motivation of applying the consecutive-interpolation procedure (CIP) is to make the trial solution and its derivatives continuous across inter-element boundaries, or in other words, stress in domain can be transited smoothly element by element. This could improve the accuracy of the computed gradients of the trial solution and avoid tackling smoothing operation technique generally utilized during the post-processing process. Another important issue should be noted that the CIP does not alter the total number of the degrees of freedom (DOFs) of the whole system. It implies that the total number of DOFs discretized by the CQ4 element is the same as that by the standard FEM.

1.2 Objectives

In this work, the objective is the application of integrating CQ4 element into the extended finite element method to implement the fracture analysis in solids. Upon achievements in previous step, it can be observed that the proposed XCQ4 performs well for the SIFs involving single and mixed-mode fracture problems, and that good results in stress intensity calculation and crack propagation can be obtained. It is because the XCQ4 approximation functions not only well capture the discontinuity and singularity induced by cracks through the enrichments, but also improve the accuracy of the stresses, consequently the stress intensity factors (SIFs). In the study, the discontinuous Heaviside function is taken to treat the discontinuity cut by crack, while the asymptotic crack-tip branch functions are embedded into the approximation functions to capture the singular field at the crack tips. An alternative way of capturing the singular field at the crack tip, another version of enrichment function, the ramp function, along with the Heaviside function [Xia et al., 2012; Kumar et al., 2016] is taken into account. To incorporate the ramp functions into both the standard XFEM using 4-node quadrilateral element (XQ4) and the developed XCQ4 is considered. The SIFs calculated by using both approaches, the ramp function with XCQ4 and with XQ4, are validated against reference solutions and can be found in the numerical examples.

Based on the fracture mechanics for two-dimensional orthotropic material and Newmark time scheme, the dynamic response in the cracked isotropic and orthotropic media is analyzed and the time history of normalized DSIFs is used to reflect the dynamic fracture behavior. By comparing the numerical results with reference solutions, the applicability of XCQ4 method in dynamic fracture analysis is verified.

The combination of XCQ4 method with fracture mapping procedure to simulate coupled deformation and fluid flow is developed to extend the application of XCQ4 in the cracked porous media. Three objectives need to be achieved: (1) Propose an effective algorithm for the implementation of Biot's theory in XCQ4 method. (2) Simulate the pressure field inside the fractured porous media without considering the interaction of the displacement and pressure field. (3) Taking advantage of transfer function, provide a mathematical description of the fluid flow interaction between the matrix and the fracture, then evaluate the time history of displacement and pressure field, respectively.

1.3 Framework of this Dissertation

Dissertation totally includes eight chapters to elaborate this study as shown in Fig 1.3.

Chapter 2 is assigned for reviewing some related literatures with respect to this work. It involves key points of theoretical knowledge and technical approaches which will be employed in this study. The related finite element method development and their recent applications are introduced, and several numerical approaches for solving fracture problem in elastic isotropic and anisotropic solids and their effects are briefly described.

Chapter 3 exhibits the formulation of XCQ4 enhanced by enrichment in terms of local partition of unity method to precisely model 2D linear elastic crack problems, taking advantages of the strengths and making use all the desirable features of both the CIP and enrichment methods. The approximation functions for the CQ4 element are extended to involve known enrichment functions, which are capable of accurately capturing the discontinuity and singularity induced by the crack. In this work, the discontinuous Heaviside function is adopted to describe the discontinuity cut by the crack faces, while the asymptotic crack-tip branch functions are integrated into the CQ4 approximation functions to capture the singular field at the crack tips.

Chapter 4 demonstrates the accuracy and performance of the proposed XCQ4 through numerical examples of 2D crack problems. Both the single and mixed-mode problems with complex configurations are considered. The interaction integral is adopted to extract the fracture parameters. The stress intensity factors (SIFs) calculated by the XCQ4 are validated against reference solutions. Examples having analytical solutions are taken, but numerical results derived from the standard XFEM using 4-node quadrilateral element (XQ4) is also employed for the comparison purpose. The convergence rate in relative errors of the SIFs is presented and investigated. The effect of the domain radius of the interaction integral on the

SIFs is explored as well.

Chapter 5 extends the XCQ4 element to the modeling of crack propagation problems in 2D solids. Upon achievements of CQ4 principle, it can be observed that the proposed XCQ4 performs well for the SIFs involving single and mixed-mode fracture problems, and the satisfactory numerical results in crack propagation are presented in this work. It is because the XCQ4 approximation functions not only well capture the discontinuity and singularity induced by cracks through the enrichments, but also improve the accuracy of the stresses, consequently the stress intensity factors (SIFs). In this work, the discontinuous Heaviside function is taken to treat the discontinuity cut by crack, while the asymptotic crack-tip branch functions are embedded into the approximation functions to capture the singular field at the crack tips. As an alternative way of capturing the singular field at the crack tip, another version of enrichment function called as, the ramp function, along with the Heaviside function is taken into account. The ramp functions are integrated into both the standard XFEM using 4-node quadrilateral element (XQ4) and the developed XCQ4. The SIFs calculated by using both approaches, the ramp function with XCQ4 and with XQ4, are validated against reference solutions and can be found in the numerical examples.

Chapter 6 is devoted for developing the XCQ4 algorithm to analyze the dynamic fracture response in isotropic and anisotropic materials, the prediction of DSIFs time history for both single and mixed-mode fracture problems is presented in this work according to previous achievements. The Heaviside function and asymptotic crack tip branch functions are integrated as enrichment to capture singular behavior near crack tips for isotropic material. For orthotropic material, versatile crack tip enrichment functions spanning all possible displacement states are adopted. In addition, the time-dependent discrete equations are solved using Newmark time integration without considering damping matrix. The numerical values of DSIFs are extracted according to interaction integral taking into account inertial effect. The time history of DSIFs derived from XCQ4 for isotropic and anisotropic solids are verified with respect to reference solutions reported in open literature.

Chapter 7 applies the XCQ4 element to simulate the fluid flow in fractured porous media without requiring the discretization to align with the geometry of the sealed fractures. The numerical model is based on a fully coupled hydro-mechanical analysis and local enriched element to represent discrete fractures. Besides, fracture mapping procedure combined with XCQ4 method is developed to model the flow interaction between the porous matrix and existing fractures by means of a transfer function.

Chapter 8 concludes the research with several points and gives some recommendations for the XCQ4 method on the frontier topics like the elasticity solution for isotropic biomaterial interface, numerical models for a contact problem and fracture analysis on multi-functional material etc. Finally future developments of XCQ4 methods are provided.

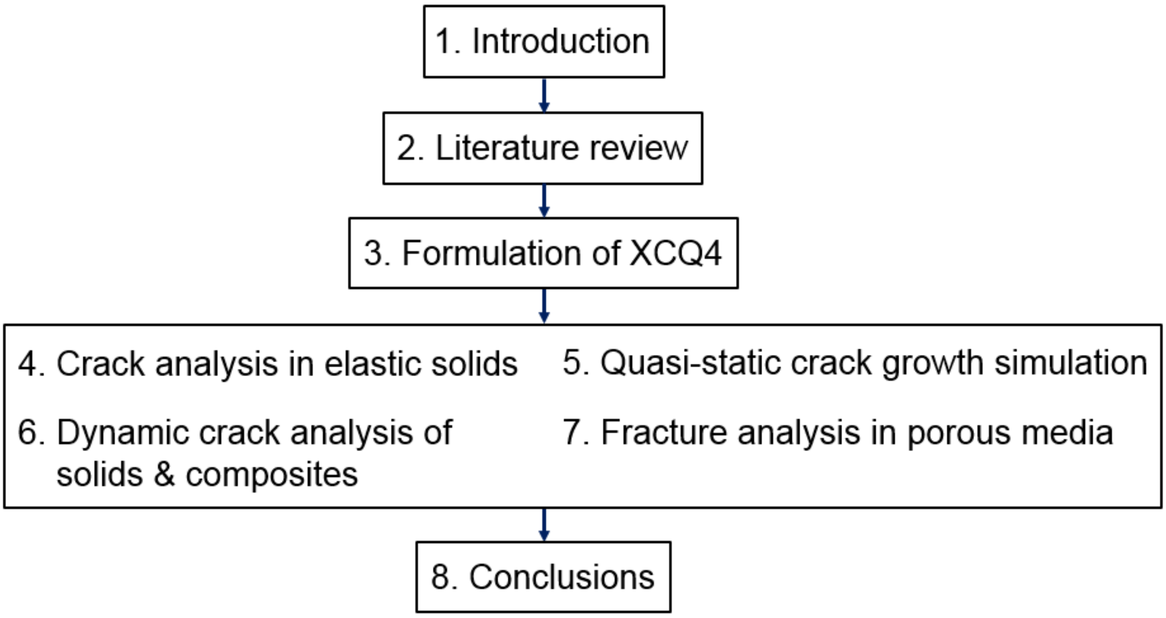

Fig. 1.3 The outline of the dissertation.

CHAPTER 2

LITERATURE REVIEW

2.1 Introduction

The classical finite element method (FEM) has been proven to be effective numerical methods for solving many engineering problems [Jacob et al., 2007]. Particularly to model crack propagation, however, remeshing is required in the FEM and that must be carried out during the evolution of crack. This task is cumbersome and it makes the method not effective in general. The extended finite element method (XFEM) and its variants, e.g., see [Belytschko et al., 1999; Zhang et al., 2015; Sharma et al., 2013; Kumar et al., 2015; Strouboulis et al., 2000; Fries et al., 2010], have been developed as its original goal is to overcome the drawbacks of the FEM. The partition of unity scheme [Babuska et al., 1997] is utilized in XFEM to facilitate the standard approximation of displacement by a set of local enriched elements to accurately acquire the fracture parameters of discontinuity, which make modeling the moving discontinuity without altering the initial prescribed mesh. Meanwhile the set of Heaviside and asymptotic crack tip enrichment functions increase the power of local solution by incorporating the arbitrary functions into the basis of the FEM.

Alternatively, extended meshfree methods [Nguyen et al., 2014; Tanaka et al., 2015], which handles only the nodal data to describe the crack, allow representation of crack topology with the aid of the vector level set technique without the finite element mesh. Recently, the edge-based strain smoothing technique using a special singular element [Liu et al., 2012] or the extended isogeometric analysis in terms of local partition of unity method [Bui et al., 2015] have also been introduced and applied to deal with fracture problems in solids as well as in multiphase materials. Other approaches such as the Lepp-Delaunay based on mesh refinement algorithm for triangular meshes [Azocar et al., 2010], and the scaled boundary finite element method (SBFEM) [Song et al., 1997; Ooi et al., 2015] are devoted to simulate crack propagation.

The new enrichment functions [Xia et al., 2012; Kumar et al., 2016] for crack tip field is proposed as only two additional degrees of freedom are added at each support node of the tip element to reduce the matrix size. For solving the quasi-static and mixed mode fracture problem several numerical research achievement can be followed [Saboori et al., 2016; Ayatollahi et al., 2015; Shi et al., 2015; Barati et al., 2016; Natarajan et al., 2014; Tabbara et al., 1998]. Further studies using the enrichments devoted to advanced composite materials and complicated configurations are also interesting to researchers majoring in computational fracture mechanics, see e.g., [Bayesteh et al., 2015; Bui et al., 2012; Yu et al., 2015; Bui et al., 2013; Bhardwaj et al., 2015; Yu et al., 2016].

2.2 Fracture Mechanics

A comprehensive investigation of a large number of catastrophic failures of structures indicates that the main reason of failure can be attributed to some kinds of geometric discontinuity or stress concentration. This form of discontinuity can be a sharp change of geometry, opening, hole, notch, crack, etc. To explain the fundamental differences of fracture mechanics and conventional theory of strength of material, some basic knowledge is introduced below.

2.2.1 Definition of Stress Intensity Factor

One important concept in fracture mechanics introduced by [Irwin, 1957] is stress intensity factors as a measure of the strength of the singularity. This method can evaluate the amount of energy available for the crack propagation in terms of asymptotic stress and displacement field. From his work, all elastic stress fields around a crack tip are distributed similarly, and $K \propto \sigma\sqrt{\pi r}$ controls the local stress quantity.

Fig. 2.1 illustrates three independent crack opening modes. Mode I is an opening mode and it corresponds to opening of the crack faces normal to each other under the action of tensile load. Mode II represents in-plane the shearing/sliding mode of movement of crack surfaces and shear stress is parallel to the plane of the crack and perpendicular to the crack front. Mode III is defined as plane tearing mode, in which the crack surfaces slid over each other in the z direction and shear stress acts parallel to the plane of the crack and crack front.

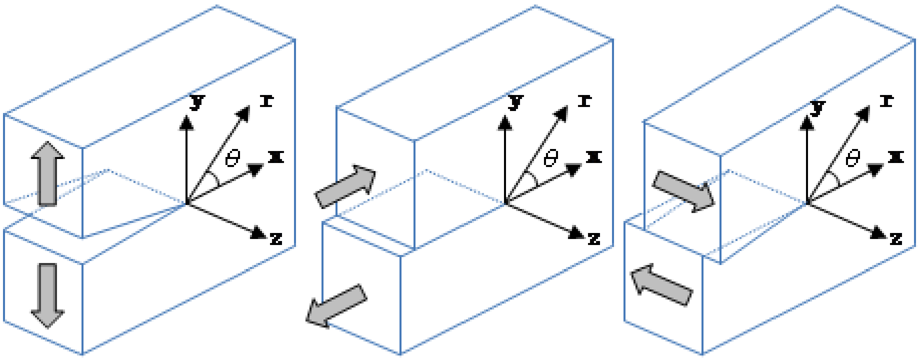

(a) (b) (c)

Fig. 2.1 Three cases of fracture mode: (a) Mode I: Opening; (b) Mode II: In-plane shear; (c) Mode III: Out of plane shear.

The stress field for linear elastic solid with respect to asymptotic stress in neighborhood of crack tip in the general form can be represented by [Mohammadi, 2008]

$$\sigma_{ij} = \frac{K_I f_{ij}^{I}(\theta) + K_{II} f_{ij}^{II}(\theta) + K_{III} f_{ij}^{III}(\theta)}{\sqrt{r}} + high\ order\ terms \tag{2.1}$$

where σ_{ij} is the Cauchy stress tensor and $K_I,\ K_{II},\ K_{III}$ are the stress intensity factors related to three independent failure modes of movement crack surfaces. r is radial distance of point of query from the crack tip. θ is the angle with respect to polar coordinate system from crack tip. $f_{ij}(\theta)$ are functions independent of loading and crack geometry.

For the first mode stress intensity factor can be simplified to:

$$K_I = \lim_{\substack{r\to 0\\ \theta=0}} \sigma_{yy}\sqrt{2\pi r} = \lim_{\substack{r\to 0\\ \theta=0}} \sigma_0\sqrt{\frac{a}{2r}}cos\frac{\theta}{2}\left(1 - sin\frac{\theta}{2}sin\frac{3\theta}{2}\right)\sqrt{2\pi r} = \sigma_0\sqrt{\pi a} \tag{2.2}$$

where a is half of the crack length.

Particularly, the asymptotic stress field for the three failure modes can be formulated as [Khoei, 2015]

$$\begin{aligned}
\sigma_{xx} &= \frac{K_I}{\sqrt{2\pi r}}\ cos\frac{\theta}{2}\left[1 - sin\frac{\theta}{2}sin\frac{3\theta}{2}\right] - \frac{K_{II}}{\sqrt{2\pi r}}\ sin\frac{\theta}{2}\left[2 + cos\frac{\theta}{2}cos\frac{3\theta}{2}\right]\\
\sigma_{yy} &= \frac{K_I}{\sqrt{2\pi r}}\ cos\frac{\theta}{2}\left[1 + sin\frac{\theta}{2}sin\frac{3\theta}{2}\right] + \frac{K_{II}}{\sqrt{2\pi r}}\ sin\frac{\theta}{2}cos\frac{\theta}{2}cos\frac{3\theta}{2}\\
\tau_{xy} &= \frac{K_I}{\sqrt{2\pi r}}\ sin\frac{\theta}{2}cos\frac{\theta}{2}cos\frac{3\theta}{2} + \frac{K_{II}}{\sqrt{2\pi r}}\ cos\frac{\theta}{2}\left[1 - sin\frac{\theta}{2}sin\frac{3\theta}{2}\right]
\end{aligned} \tag{2.3}$$

and the displacement field also can be represented as

$$\begin{aligned}
u_x &= \frac{K_I}{2\mu}\sqrt{\frac{r}{2\pi}}cos\frac{\theta}{2}\left[\kappa - 1 + 2sin^2\frac{\theta}{2}\right] + \frac{K_{II}}{2\mu}\sqrt{\frac{r}{2\pi}}sin\frac{\theta}{2}\left[\kappa + 1 + 2cos^2\frac{\theta}{2}\right]\\
u_y &= \frac{K_I}{2\mu}\sqrt{\frac{r}{2\pi}}sin\frac{\theta}{2}\left[\kappa + 1 - 2cos^2\frac{\theta}{2}\right] - \frac{K_{II}}{2\mu}\sqrt{\frac{r}{2\pi}}cos\frac{\theta}{2}\left[\kappa - 1 - 2sin^2\frac{\theta}{2}\right]
\end{aligned} \tag{2.4}$$

where parameter κ is defined as

$$\kappa = \begin{cases} \dfrac{3-\nu}{1+\nu} & plane\ stress\\ 3-4\nu & plane\ strain \end{cases} \tag{2.5}$$

2.2.2 J-integral

The J-integral method is introduced by [Rice, 1968] to represents a way to compute the strain energy release rate for the material where the deformation of crack tip does not comply with LEFM. This contour integral is path independent in terms of the theorem of energy conservation and identifies a line integral which possesses the same value for all integration paths surrounding the crack tip. Path independency of J-integral also allows for the evaluation of linear and nonlinear elastic energy release rate and elasto-plastic work in a far field around a crack tip according to the deformations near crack tip. In this way the complexity of analyzing the stress and displacement field in crack tip can be avoided by assessing the energy release rate in the domain where the results are available.

Thus, the two dimension form of Rice's integral can be written as [Mohammadi, 2008]

$$J = \oint_{\Gamma} W_s \, dy - \mathbf{t} \frac{\partial \mathbf{u}}{\partial x} ds \tag{2.6}$$

where Γ is a closed counter-clockwise contour surrounding the crack tip as shown in Fig. 2.2. $\mathbf{t}$ is traction vector on a plane defined by the outward normal $\mathbf{n}$, i.e., $\mathbf{t} = \boldsymbol{\sigma} \bullet \mathbf{n}$. $\mathbf{u}$ is the displacement vector and ds is the differential element of the arc length along Γ. W_s is the strain energy density given by

$$W_s = \int_0^{\varepsilon} \sigma_{ij} d\varepsilon_{ij} \tag{2.7}$$

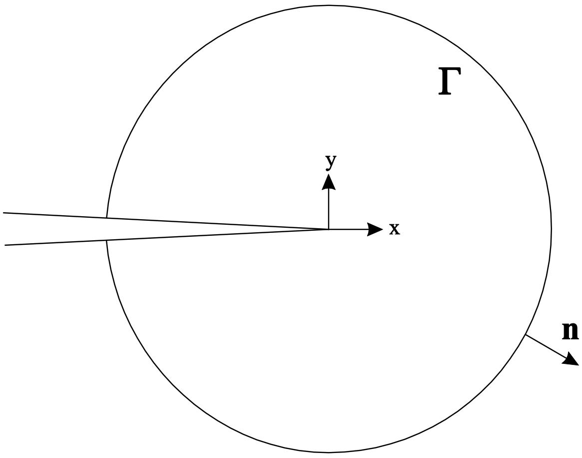

Fig. 2.2 J-integral surrounding a crack in 2D space.

2.2.3 Theoretical Knowledge of Interaction integral

In the interaction integral method, auxiliary field is adopted and combined with actual field satisfying the boundary value problem reported in [Sih et al., 1965]. These auxiliary fields are properly selected to tackle the problem that stress intensity factor for the two modes cannot be obtained independently of each other. With the purpose of finding relationship between the mixed mode stress intensity factors, two equilibrium states of the body are defined as state 1 for the actual state and state 2 for the auxiliary state. The corresponding variables for both states are denoted with superscript 1 and 2, respectively.

Therefore, the superposition of the two equilibrium states can be written as [Belytschko et al., 1999]

$$J^{(1+2)} = \int_{\Gamma} \left[\frac{1}{2}\left(\sigma_{ij}^{(1)} + \sigma_{ij}^{(2)}\right)\left(\varepsilon_{ij}^{(1)} + \varepsilon_{ij}^{(2)}\right)\delta_{1j} - \left(\sigma_{ij}^{(1)} + \sigma_{ij}^{(2)}\right)\frac{\partial\left(u_i^{(1)} + u_i^{(2)}\right)}{\partial x_j} \right] n_j \, d\Gamma \tag{2.8}$$

After the simple manipulation, the simplified form can be obtained as

$$J^{(1+2)} = J^{(1)} + J^{(2)} + M^{(1,2)} \tag{2.9}$$

where $M^{(1,2)}$ is the interaction integral and can be written as

$$M^{(1,2)} = \int_{\Gamma} \left[W^{(1,2)}\delta_{1j} - \sigma_{ij}^{(1)}\frac{\partial u_i^{(2)}}{\partial x_j} - \sigma_{ij}^{(2)}\frac{\partial u_i^{(1)}}{\partial x_j} \right] n_j \, d\Gamma \tag{2.10}$$

where $W^{(1,2)}$ is the interaction integral strain energy and can be given as

$$W^{(1,2)} = \sigma_{ij}^{(1)}\varepsilon_{ij}^{(2)} = \sigma_{ij}^{(2)}\varepsilon_{ij}^{(1)} \tag{2.11}$$

An alternative representation of the relationship between J-integral and mixed mode stress intensity factors can be defined as

$$J = \frac{1}{E^*}\left(K_I^{(1)} + K_I^{(2)}\right) \tag{2.12}$$

where

$$E^* = \begin{cases} E & plane\ stress \\ \dfrac{E}{1 - \upsilon^2} & plane\ strain \end{cases} \tag{2.13}$$

Combining the Eqs. (2.9) and (2.12), the interaction integral can be rewritten as

$$J^{(1+2)} = J^{(1)} + J^{(2)} + \frac{2}{E^*}\left(K_I^{(1)}K_I^{(2)} + K_{II}^{(1)}K_{II}^{(2)}\right) \tag{2.14}$$

that is to say

$$M^{(1,2)} = \frac{2}{E^*}\left(K_I^{(1)}K_I^{(2)} + K_{II}^{(1)}K_{II}^{(2)}\right) \tag{2.15}$$

Subsequently, the M-integral can be used to evaluate the stress intensity factors of actual state in the region far from the crack tip by assigning different value for auxiliary field. If consider auxiliary field as fracture mode I, $K_I^{(2)} = 1$ and $K_{II}^{(2)} = 0$ can be obtained; for mode II, the value should be $K_I^{(2)} = 0$ and $K_{II}^{(2)} = 1$. Substitute these known conditions into Eq. (2.15), the following relationship can be given as [Belytschko et al., 1999]

$$\begin{aligned} K_I^{(1)} &= \frac{E^*}{2}M^{(1,2,1)} \\ K_{II}^{(1)} &= \frac{E^*}{2}M^{(1,2,2)} \end{aligned} \tag{2.16}$$

where $M^{(1,2,1)}$ and $M^{(1,2,2)}$ denotes the evaluation of M-integral in first and second auxiliary state, respectively.

For the convenient implementation of the M-integral, the weight function $q(\mathbf{x})$ is adopted and it is an arbitrary smooth function varying in between zero and unity. Then, M-integral can be evaluated in a closed path $S = \Gamma \cup S^- \cup \Gamma_0 \cup S^+$ as shown in Fig. 2.3 with expression of

$$M^{(1,2)} = \int_S \left[W^{(1,2)}\delta_{1j} - \sigma_{ij}^{(1)}\frac{\partial u_i^{(2)}}{\partial x_j} - \sigma_{ij}^{(2)}\frac{\partial u_i^{(1)}}{\partial x_j}\right] q m_j \, d\Gamma \tag{2.17}$$

where m_j are components of unit normal vector to the closed curve S. It can be observed that the direction of $\mathbf{m}$ is identical with $\mathbf{n}$ on the outward boundary and inverse on the inward side.

With the assumption of traction free for crack faces, manipulate Eq. (2.17) using divergence theorem, the following equation can be obtained as [Belytschko et al., 1999]

$$M^{(1,2)} = \int_A \left[W^{(1,2)}\delta_{1j} - \sigma_{ij}^{(1)} \frac{\partial u_i^{(2)}}{\partial x_j} - \sigma_{ij}^{(2)} \frac{\partial u_i^{(1)}}{\partial x_j} \right] \frac{\partial q}{\partial x_j} dA \tag{2.18}$$

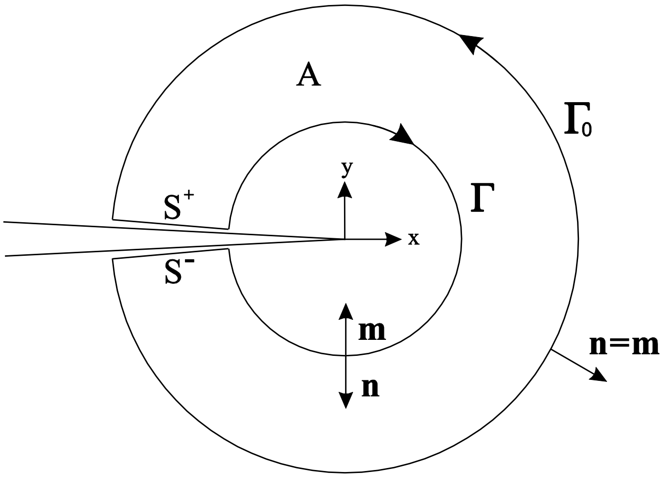

Fig. 2.3 A quadrilateral element in (a) global coordinate and (b) natural coordinate system.

2.3 Extended Finite Element Method (XFEM)

The basic idea of XFEM is to enrich the approximation space to reproduce certain features of the problem related to discontinuity such as crack and interface etc. Based on the partition of unity method, the enriched functions are used to describe the field behavior integrated locally into the finite element approximation space and the solution can fully reflect the actual response. Subsequently, the related knowledge of XFEM is demonstrated, which adopts local partition of unity to indicate the desired features of interest.

2.3.1 Partition of Unity

The partition of unity finite element method (PUFEM) is the use of partition of unity functions whose values sums up to unity at each point in the considered domain. The local approximation U^h has to integrate to assemble the global approximation space U to make the difference between U^h and U is minimum. Generally, this objective implements by bounding the local error $||U^h - U||$ using the function:

$$\sum_{i=1}^{N} \omega_i(\mathbf{x}) = 1 \quad \forall \mathbf{x} \in \Omega \tag{2.19}$$

the function $\omega_i(\mathbf{x})$ is called as partition of unity function and has a non-zero value only in the considered supports.

The concept of partition of unity has been employed in various computational methodology [Melenk and Babusk, 1996]. It can readily be shown selection of any arbitrary function $\psi(\mathbf{x})$, the following property is readily deduced:

$$\sum_{i=1}^{N} \omega_i(\mathbf{x})\psi(\mathbf{x}) = \psi(\mathbf{x}) \tag{2.20}$$

Let us use the classical finite element shape functions $N_j(\mathbf{x})$ to demonstrate the application of partition of unity. For an arbitrary point $\mathbf{x}$ within a finite element:

$$\mathbf{u}^h(\mathbf{x}) = \sum_{j=1}^{n} N_j(\mathbf{x})\mathbf{u}_j \tag{2.21}$$

where n is the number of nodes for each element. The notion of partition of unity provides a mathematical framework for the development of an enriched solution.

2.3.2 Level Set Method

The level set method is a method introduced by [Osher and Sethian, 1988] for figuring out the problem of a moving interface. The principle of the level set method is to represent the changing interfaces at any time t with a zero level set function i.e. $\phi(\mathbf{x}, t) = 0$.

For the modelling of the discontinuity such as flaw, define the level set function as a signed distance function. As the flaw has not split the domain into two separate parts completely, two level set functions, (i) normal level set function $\phi(\mathbf{x})$; (2) tangential level set function $\psi(\mathbf{x})$, are required to fully represent crack location. Both two level set functions are defined as a signed distance function which can be represented as [Khoei, 2015]

$$\phi(\mathbf{x}) = \left(\mathbf{x} - \mathbf{x}_f\right) \cdot \mathbf{n} \tag{2.22}$$

where $\mathbf{x}$ is arbitrary point and $\mathbf{x}_f$ is a closet point on the flaw surface. $\mathbf{n}$ is a unit normal vector to the crack face. Based on the work stated in [Stolarska et al., 2001], the specific value associated with different region in Fig. 2.4 can be obtained.

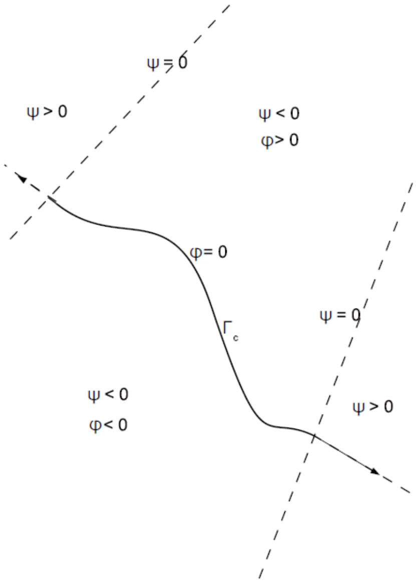

Fig. 2.4 Level set functions.

Generally, the following steps are considered to implement the level set approach:

a) Define the normal level set function ϕ and tangential level set function ψ as the signed distance function ζ and η:

$$\begin{aligned} \varphi(\mathbf{x}) &= \zeta(\mathbf{x}) \\ \psi(\mathbf{x}) &= \eta(\mathbf{x}) \end{aligned} \tag{2.23}$$

b) The flaw front is taken as zero level set $\varphi(\mathbf{x}) = 0$; $\psi(\mathbf{x}) = 0$.

c) Both level set functions are discretized according to the nodal values:

$$\begin{aligned} \varphi(\mathbf{x}) &= \sum_{i=1}^{N} N_j(\mathbf{x})\varphi(\mathbf{x}_j) \\ \psi(\mathbf{x}) &= \sum_{i=1}^{N} N_j(\mathbf{x})\psi(\mathbf{x}_j) \end{aligned} \tag{2.24}$$

2.3.3 Fundamental of XFEM Approximation

In the context of XFEM, usually the finite element mesh is created firstly. Then, in the consideration of the discontinuities, additional degrees of freedom are incorporated into the standard finite element method model in the selected nodes along the discontinuities to provide a higher level of accuracy for capturing the fracture behavior of physical field.

The basic approximation to calculate the displacement for the point $\mathbf{x}$ locating within the considered element is given by [Belytschko et al., 1999]:

$$\mathbf{u}^h(\mathbf{x}) = \mathbf{u}^{Std} + \mathbf{u}^{Enr} = \sum_{j=1}^{n} N_j(\mathbf{x})\mathbf{u}_j + \sum_{r=1}^{s} N_r(\mathbf{x})\chi(\mathbf{x})\mathbf{a}_r \tag{2.25}$$

where $\mathbf{u}_j$ is the displacement vector of standard DOFs in the finite element method, $\mathbf{a}_r$ is the additional set of DOFs and $\chi(\mathbf{x})$ is the discontinuous enrichment functions for the set of nodes that the discontinuity is in its support domain.

$\mathbf{u}^{Std}$ is the standard finite element approximation to compute the displacement field, while $\mathbf{u}^{Enr}$ is the enrichment approximation which takes into account the existence of any discontinuities. Also the enriched part of displacement approximation results in additional degrees of freedom to facilitate the modelling of discontinuities without the requirement of conformation to finite element mesh.

For multiple discontinuities inside domain, usually the displacement approximation can be further extended to:

$$\mathbf{u}^h(\mathbf{x}) = \mathbf{u}^{Std} + \mathbf{u}^{Enr} = \sum_{j=1}^{n} N_j(\mathbf{x})\mathbf{u}_j + \sum_{l=1}^{N}\sum_{r=1}^{s} N_r(\mathbf{x})\chi(\mathbf{x})\mathbf{a}_r \tag{2.26}$$

where N is the number of the discontinuity.

It is worth remarking that the extended finite element method can be regarded as a local version of the partition of unity finite element method (PUFEM) proposed by [Melenk and Babuska, 1996], which means only a region adjacent the discontinuities such as crack, void, inclusion, and material interface is enriched in terms of corresponding enrichment functions involving Heaviside function and asymptotic crack tip enrichment function, etc.

2.4 Crack Propagation Criteria

On account of the presence of the inclined or curvilinear crack, the fracture evolution in this case present more complex mechanism than the pure fracture mode I, which results in non-zero K_I and K_{II} stress intensity factors.

The analytical solution for an inclined crack in an infinite plate can be given as [Mohammadi, 2008]:

$$K_I = \sigma sin^2\theta_0\sqrt{\pi a}$$
$$K_{II} = \sigma sin\theta_0 cos\theta_0\sqrt{\pi a} \tag{2.27}$$

where θ_0 is the angle between crack direction and horizontal axis.

In general, the relationship for the collinear crack propagation criterion can be described with respect to SIFs (K_I and K_{II}) and fracture toughness factors (K_{Ic} and K_{IIc}):

$$f(K_I, K_{II}, K_{Ic}, K_{IIc}) = 0 \tag{2.28}$$

2.4.1 Maximum Circumferential tensile stress

The initial theory of the mixed mode stress intensity factor based on the solution of the stress field adjacent crack tip is developed by [Erdogan and Sih,1963]. According to the corresponding assumption, crack propagates from its tip in a radial direction within a plane vertical to the direction of maximum tension when the maximum circumferential tensile stress reaches a critical material constant.

The mixed mode criterion for crack propagation direction is given as: K_I and K_{II} stress intensity factors.

The analytical solution for an inclined crack in an infinite plate can be given as [Mohammadi, 2008]:

$$\frac{K_I}{K_{Ic}} cos^3\frac{\theta}{2} - \frac{3}{2}\frac{K_{II}}{K_{Ic}} cos\frac{\theta}{2} sin\theta = 1 \tag{2.29}$$

2.4.2 Minimum Strain Energy Density Criterion

The minimum strain energy density criterion indicates that a crack propagates along the minimum resistance path. Namely, the crack growth direction θ is determined along which the strain energy density at a critical distance is minimum. When the resistance reaches a critical value, crack evolution will start.

[Sih, 1973, 1974] defines the specific formulation of the criterion as:

$$\frac{8\mu}{(\kappa-1)}\left[a_{11}\left(\frac{K_I}{K_{Ic}}\right)^2+2a_{12}\frac{K_I K_{II}}{(K_{Ic})^2}-a_{22}\left(\frac{K_{II}}{K_{Ic}}\right)^2\right]=1 \tag{2.30}$$

where

$$a_{11}=\frac{1}{16\mu}[(1+cos\theta)(\kappa-cos\theta)]$$

$$a_{12}=\frac{sin\theta}{16\mu}[2cos\theta-(\kappa-cos\theta)] \tag{2.31}$$

$$a_{22}=\frac{1}{16\mu}[(\kappa+1)(1-cos\theta)+(1+cos\theta)(3cos\theta-1)]$$

2.4.3 Maximum Energy Release Rate

According to the achievement of SIFs for a major existing crack with an infinitesimal tip kink at an angle θ, the maximum energy release rate model was developed. The SIFs of the original crack K_I and K_{II} can be defined as:

$$\begin{aligned} K_I(\theta)&=g(\theta)\left(K_I cos\theta+\frac{3}{2}K_{II}sin\theta\right)\\ K_{II}(\theta)&=g(\theta)\left(K_{II}cos\theta-\frac{3}{2}K_I sin\theta\right)\end{aligned} \tag{2.32}$$

with

$$g(\theta)=\left(\frac{4}{3+cos^2\theta}\right)\left(\frac{1-\frac{\theta}{\pi}}{1+\frac{\theta}{\pi}}\right)^{\frac{\theta}{2\pi}} \tag{2.33}$$

The general form of the energy release rate based on the Irwin's generalized expression is

$$G(\theta)=\frac{1}{E'}(A_{11}K_I{}^2(\theta)+2A_{12}K_I(\theta)K_{II}(\theta)+A_{22}K_{II}{}^2(\theta)) \tag{2.34}$$

where

$$\begin{bmatrix} A_{11} \\ A_{12} \\ A_{22} \end{bmatrix} = g^2(\theta) \begin{bmatrix} 4 - 3sin^2\theta \\ -2sin2\theta \\ 4 + 5sin^2\theta \end{bmatrix} \tag{2.35}$$

2.5 Dynamic Fracture Behavior in Orthotropic Material

Composite materials featuring the light weight, high strength etc. have been widely applied to product design and engineering structure in recent decades. The investigation with respect to material property inside the anisotropic solids has arisen as one interesting topic and especially the fracture behavior of such kind material attracts much attention from researchers. The dynamic fracture issues of composite materials always occur in the fields of aviation, infrastructure, automotive and so on, which requires targeted study to clarify the complex mechanism of dynamic fracture behavior in the orthotropic material. On account of the increasing of the material constants, anisotropic fundamental solutions become more complicated to determine than those of isotropic media [Muskhelishvili et al., 1977]. The fracture mechanics of the composite material and elastodynamic behavior around a propagating crack in an anisotropic medium have been studied for solving anisotropic static and quasi-static crack problems [Cruse et al., 1971; Carloni et al., 2003; Nobile et al., 2005; Lowerey et al., 1993; Thomas et al., 2013]. Based on the analytical research, the stress and displacement formulation around linear crack in anisotropic solids can be obtained.

Due to the restriction of implementation of analytical methods for solving various static and dynamic problems, a numerical method is becoming preferable to simulate the fracture behavior in composite materials. Based on the implementation of time-harmonic, Laplace-domain or time-domain dynamic fundamental solutions, the frequency-domain BEM [Dineva et al., 2005] and time-domain BEM [Tan et al., 2005; Felipe et al., 2008] for dynamic crack analysis in anisotropic materials can be gained. [Nguyen et al., 2016] investigated the transient dynamic stress intensity factors (DSIFs) in orthotropic material using an extended meshfree radial point interpolation method (X-RPIM), which enriches the application of the meshfree method [Menouillar et al., 2010] in combination of a ramp function to enrich a crack tip. The edge-based strain smoothing technique [Liu et al., 2012] using a special singular element or the extended isogeometric analysis in terms of local partition of unity method [Melenk et al., 1996; Duarte et al.,1996] have also been introduced and applied to deal with fracture problems in multiphase materials. Other approaches related to anisotropic shell theory [Li et al., 2017], experimental implementation [Shan et al., 2017] are devoted to explore the influence of anisotropic mechanical properties on shear or buckling damage of plates.

Finite element method is famous for the capability of providing robust solutions for non-linear, plastic, dynamic problems and can treat arbitrary boundary conditions and complicated configuration of various cases [Mars et al., 2015] proposed an anisotropic plasticity model to obtain reliable prediction using a finite element method in an orthotropic plasticity model for sheet metal in impact simulation. For numerical fracture solutions, the extended finite element method (XFEM) [Belytschko et al., 1999; Bui et al., 2013] is more advantageous than the FEM that needs crack modelling align with finite element mesh and remeshing procedure in crack propagation problem. [Asadpoure et al., 2006, 2007] and [Hattori et al., 2012] explored fracture properties of the orthotropic models and proposed a new enrichment function for crack modelling in orthotropic solids using the interaction integral for calculating stress intensity factors under the framework of the extended finite element method.

Accurate estimation of DSIFs is imperative to analyze dynamic fracture mechanism of composite materials. Transient dynamic problems for stationary crack were conducted by [Nguyen et al., 2016; Bui et al., 2012, 2015, 2016; Song et al., 1997]. [Song et al., 2006] evaluated DSIFs by incorporating dynamic effects into homogeneous and non-homogeneous material and found out that M-integral is superior to the displacement correlation technique (DCT) comparing with J-integral [Albuquerque et al., 2004] computed DSIFs based on the crack opening displacements using a dual boundary element method. The elastodynamic response induced by an in-plane shear load was investigated in orthotropic material by [Rubio-Gonzalez et al., 1999].

The concept of dynamic stress intensity factors (DSIFs) can be directly derived from the conventional definition of stress intensity factors in linear elastic fracture mechanics [Mohammadi, 2008]:

$$\begin{aligned} K_I^{dyn} &= \lim_{\substack{r \to 0 \\ \theta = 0}} \sigma_{yy} \sqrt{2\pi r} \\ K_{II}^{dyn} &= \lim_{\substack{r \to 0 \\ \theta = 0}} \sigma_{xx} \sqrt{2\pi r} \end{aligned} \tag{2.36}$$

Validation of dynamic stress intensity factors depends on the computation of the J-integral using the domain integral method or the interaction integral approach. The latter one is based on two dependent actual and auxiliary fields proposed by [Piva et al., 2005]. The mixed mode crack propagation is studied in terms of similar forms of static criteria as given in Eq. (2.28), except for using dynamic stress intensity factors.

After realizing the direction of crack evolution and the corresponding dynamic stress intensity factors, the growth speed of the crack tip $\dot{a}$ can be determined from the dynamic fracture toughness K_C^{dyn}. Here, the maximum circumferential tensile stress is used as the crack propagation criterion for mixed fracture mode, the following simplified equation can be formulated [Mohammadi, 2008]:

$$K_{\theta\theta}^{dyn} = K_C^{dyn} = \frac{K_{IC}}{1 - (\dot{a}/C_r)} \tag{2.37}$$

where C_r is the Rayleigh wave speed.

2.6 Mechanics of Saturated Porous Media

The description of multiphase systems in interpenetrating continuous bodies, such as porous media, is based on the mixture theory combined by the notion of volume fractions or averaging theories in conjunction with Biot’s theory [Biot, 1941]. As the averaging theories provide possibilities for a better understanding with respect to microscopic state and the relationship between microscopic and macroscopic that represents the natural domain of all continuum mechanical models. Based on the spatial averaging operators from averaging theories, taking advantage of macroscopic variables associated with real measureable quantities links to practical application such as soil mechanics [Lewis et al., 1998].

2.6.1 Averaging Principles

Microscopic level: Consider the actual non-homogeneous structure of the porous medium domain. The scale of the inhomogeneity is of the same order of magnitude as the dimensions of a pore or a grain. For the practical description of the processes taking place in a porous medium, the level of detail given is not required.

Macroscopic level: The actual multiphase system that takes up the porous medium domain is depicted by a model in which each phase is assumed to fill up the entire domain. In this way, all phases are supposed to present at each point even for overlapping continua in the porous solid. This is the level of interest of continuum mechanics, where the continuous distribution of the components through a macroscopic control space is investigated. At this level, homogeneous material is usually considered, but non-homogeneities may still exist, e.g. strata. Their scale is of an order of magnitude comparable with the order of magnitude of the entire domain.

Megascopic level: For this level, the similar conditions is used referring to previously defined level. The slight difference is the fact that part of macroscopic inhomogeneity is eliminated by averaging and the mathematical model is built in a domain which has fewer dimensions than the actual domain. In other words, one two dimensional issue with field values usually is averaged over the thickness. Typical applications of this level can be found in the simulation of land subsidence problems on a regional scale.

2.6.2 Microscopic Balance Equations

To describe the microscopic situation of any π phase, the classical balance equations of continuum mechanics are briefly introduced. At the interfaces with other constituents, the material attributes and thermodynamic quantities may present step discontinuities [Lewis et al., 1998].

For a generic conserved variable ψ, the conservation equation within the π phase is given as

$$\frac{\partial(\rho\psi)}{\partial t} + \operatorname{div}(\rho\psi\dot{\mathbf{r}}) - \operatorname{div}(\mathbf{i}) - \rho b = \rho G \tag{2.38}$$

where $\dot{\mathbf{r}}$ is the local value of the velocity field of the π phase at a fixed point in space, $\mathbf{i}$ is the flux vector related to ψ, b is the external supply of ψ and G is the net production of ψ.

At the interface between two constituents π phase and α phase, the jump condition is represented as [Lewis et al., 1998]

$$[\rho\psi(\mathbf{w} - \dot{\mathbf{r}}) + \mathbf{i}]|_{\pi} \cdot \mathbf{n}^{\pi\alpha} + [\rho\psi(\mathbf{w} - \dot{\mathbf{r}}) + \mathbf{i}]|_{\alpha} \cdot \mathbf{n}^{\alpha\pi} = 0 \tag{2.39}$$

where $\mathbf{w}$ is the velocity of the interface, $\mathbf{n}^{\alpha\pi}$ is the unit normal vector pointing out of the π phase.

It is worth noting that this assumption has no consideration of the thermo-mechanical properties and does not exclude the possibility of exchange of mass, momentum or energy between the constituents.

2.6.3 Macroscopic Balance Equations

A general average macroscopic balance equation is obtained from the microscopic balance equation and in this equation, macroscopic quantities are obtained through the previously defined averaging operators. Note that the balance equations are written in a material-free manner.

A detailed form of the general balance equation associated with the macroscopic thermodynamic property $\bar{\psi}^{\pi}$ and the mass averaged velocity $\bar{\mathrm{V}}^{\pi}$ for the π phase is given as

$$\int_{\mathrm{V}} \left[\frac{\partial}{\partial t}[\langle\rho\rangle_{\pi}\bar{\psi}^{\pi}] + \mathrm{div}[\langle\rho\rangle_{\pi}\bar{\psi}^{\pi}\bar{\mathrm{V}}^{\pi}] - \mathrm{div}(\mathbf{i}^{\pi}) - \langle\rho\rangle_{\pi}\left[\bar{b}^{\pi} + \bar{e}^{\pi}(\rho\psi) + I^{\pi}\right]\right] dV = \int_{\mathrm{V}} \langle\rho\rangle_{\pi}\,\bar{G}^{\pi} dv \tag{2.40}$$

where $\langle\rho\rangle_{\pi}$ is the volume-averaged value of mass density, $\mathbf{i}^{\pi}$ is the flux vector associated with $\bar{\psi}^{\pi}$, $\bar{b}^{\pi}$ is the external supply of the $\bar{\psi}^{\pi}$ and other involved parameters has been introduced by [Lewis, 1998] in detail.

2.7 Summary

Based on the fundamental of relevant fracture mechanics involved in this dissertation, some literatures have been reviewed in this chapter. In the following work, those basic theories and achievements will be cited as the initial basis to advance further research, which are considerably helpful to this dissertation.

CHAPTER 3

FORMULATION OF XCQ4

3.1 Introduction

Recently, the new formulated 4-node quadrilateral element with continuous nodal stress by applying the concept of the twice-interpolation procedure [Zheng et al., 2010; Wu et al., 2012] to the standard 4-node quadrilateral element was developed for stress analysis of 2D elastic solids. Notice that the term “twice-interpolation” has been replaced by a different name as “consecutive-interpolation” in this work for a better representation. Consequently the consecutive-interpolation 4-node quadrilateral element (CQ4) is thus born. In a similar fashion the CQ4 element also owns a number of desirable features of an accurate numerical method. Generally the basis functions for the CQ4 element are constructed in two stages. The same interpolation function as in the common FEM for the 4-node quadrilateral element is first constructed. Subsequently, the interpolation function constructed by the first step is then extended to involve both the nodal values and averaged values of gradients of the unknowns at the nodes.

Nevertheless, the major motivation of applying the consecutive-interpolation procedure

(CIP) is to make the trial solution and its derivatives continuous across inter-element boundaries, or in other words, stress in domain can be transited smoothly element by element. This could improve the accuracy of the computed gradients of the trial solution and avoid tackling smoothing operation technique generally utilized during the post-processing process. Another important issue should be noted that the CIP does not alter the total number of the degrees of freedom (DOFs) of the whole system. It implies that the total number of DOFs discretized by the CQ4 element is the same as that by the standard FEM.

3.2 Basic Theory

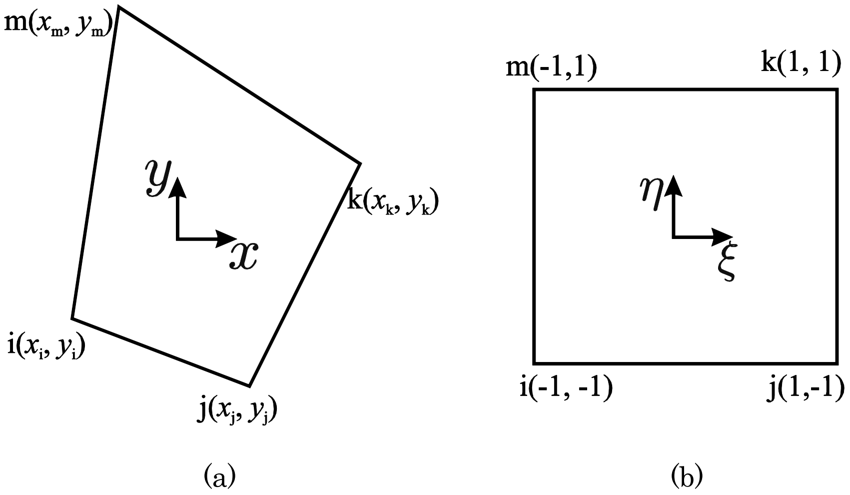

Fig. 3.1 A quadrilateral element in (a) global coordinate and (b) natural coordinate system.

In this section, the quadrilateral element with four-node based on the CIP procedure is formulated. The four-node quadrilateral element in the global coordinate system can be mapped to the four-node rectangular element in the natural one as shown in Fig. 3.1. The geometry of the quadrilateral element can be expressed explicitly by:

$$\begin{aligned} x &= L_i(\xi,\eta)x_i + L_j(\xi,\eta)x_j + L_k(\xi,\eta)x_k + L_m(\xi,\eta)x_m \\ y &= L_i(\xi,\eta)y_i + L_j(\xi,\eta)y_j + L_k(\xi,\eta)y_k + L_m(\xi,\eta)y_m \end{aligned} \tag{3.1}$$

where $L_i(\xi,\eta), L_j(\xi,\eta), L_k(\xi,\eta)$ and $L_m(\xi,\eta)$ are taken as standard interpolation functions as

$$
\begin{aligned}
L_i(\xi,\eta) &= \frac{1}{4}(1-\xi)(1-\eta) \\
L_j(\xi,\eta) &= \frac{1}{4}(1+\xi)(1-\eta) \\
L_k(\xi,\eta) &= \frac{1}{4}(1+\xi)(1+\eta) \\
L_m(\xi,\eta) &= \frac{1}{4}(1-\xi)(1+\eta)
\end{aligned}
\tag{3.2}
$$

and the partial derivatives can also be calculated through the inverse Jacobian matrix $\mathbf{J}^{-1}$ by

$$
\begin{Bmatrix} \dfrac{\partial}{\partial x} \\ \dfrac{\partial}{\partial y} \end{Bmatrix} = \mathbf{J}^{-1} \begin{Bmatrix} \dfrac{\partial}{\partial \xi} \\ \dfrac{\partial}{\partial \eta} \end{Bmatrix}
\tag{3.3}
$$

with

$$
\mathbf{J} = \begin{bmatrix} \dfrac{\partial x}{\partial \xi} & \dfrac{\partial y}{\partial \xi} \\ \dfrac{\partial x}{\partial \eta} & \dfrac{\partial y}{\partial \eta} \end{bmatrix} = \begin{bmatrix} \dfrac{\partial L_i}{\partial \xi} & \dfrac{\partial L_j}{\partial \xi} & \dfrac{\partial L_k}{\partial \xi} & \dfrac{\partial L_m}{\partial \xi} \\ \dfrac{\partial L_i}{\partial \eta} & \dfrac{\partial L_j}{\partial \eta} & \dfrac{\partial L_k}{\partial \eta} & \dfrac{\partial L_m}{\partial \eta} \end{bmatrix} \begin{bmatrix} x_i & y_i \\ x_j & y_j \\ x_k & y_k \\ x_m & y_m \end{bmatrix}
\tag{3.4}
$$

From Eqs. (3.1) and (3.2), the (3.4) can be rewritten as

$$
\mathbf{J} = \frac{1}{4} \begin{bmatrix} -(1-\eta) & (1-\eta) & (1+\eta) & -(1+\eta) \\ -(1-\xi) & -(1+\xi) & (1+\xi) & (1-\xi) \end{bmatrix} \begin{bmatrix} x_i & y_i \\ x_j & y_j \\ x_k & y_k \\ x_m & y_m \end{bmatrix}
\tag{3.5}
$$

The inverse of Jacobian matrix can be obtained as

$$
\mathbf{J}^{-1} = \frac{1}{4\det(\mathbf{J})} \begin{bmatrix} J_1 & J_2 \\ J_3 & J_4 \end{bmatrix}
\tag{3.6}
$$

with

$$
\begin{aligned}
J_1 &= -y_i(1-\xi) - y_j(1+\xi) + y_k(1+\xi) + y_m(1-\xi) \\
J_2 &= y_i(1-\eta) - y_j(1-\eta) - y_k(1+\eta) + y_m(1+\eta) \\
J_3 &= x_i(1-\xi) + x_j(1+\xi) - x_k(1+\xi) - x_m(1-\xi)
\end{aligned}
\tag{3.7}
$$

$$J_4 = -x_i(1-\eta) + x_j(1-\eta) + x_k(1+\eta) - x_m(1+\eta)$$

3.3 Consecutive-interpolation technique

The improved XCQ4 is enhanced by enrichment functions in terms of the partition of unity method for possibly modeling singular fields at the crack tips. The proposed XCQ4 is not only particularly suitable for cracks modeling, but the accuracy of the computed gradients of the trial solution is also improved. The smoothing operation in the post-processing process is no longer required. More interesting, the total number of DOFs of the whole system discretized by the XCQ4 does not change. It means that the XCQ4 and the common XQ4 offer the same number of DOFs for the whole system.

In modeling crack problems using the conventional FEM, one of the most important issues is to reproduce the $1/\sqrt{r}$ stress singularity in the vicinity of the crack tip. Obviously, a special element, e.g., singular crack-tip element or enriched element, is often required to serve the interpolation, and more importantly to ensure the singular stress field at the crack-tip. Despite the accuracy of the results obtained by the aforementioned special elements can be acceptable for some particular cases, but the mesh-dependent crack geometry is one of their limitations. It is even more cumbersome when dealing with crack propagation problems since the crack configuration and its relevant parameters must be updated, or in other words, a re-meshing task must be taken into account. However, all the difficult issues of the traditional FEM pertaining to the mesh problems are completely avoided in the new XCQ4 as the singularity and discontinuity induced by the crack is captured by enrichment functions.

In this section, the construction of the CQ4 shape functions and their properties are briefly given. The extended CQ4 finite element approximation for crack and derive the XCQ4 discrete equations is presented.

3.3.1 Formulation of Consecutive-interpolation Quadrilateral

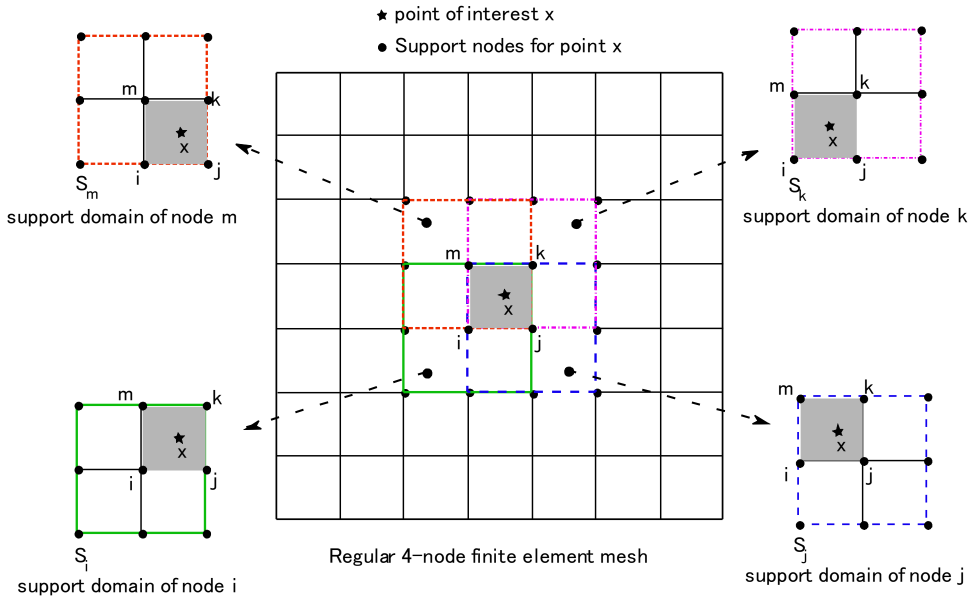

Fig. 3.2 Illustration of a consecutive-interpolation 4-node quadrilateral element in 2D and its support domain.

For the sake of completeness, a brief establishment of the CQ4 shape functions is presented here. Let $\mathbf{x} = (\mathrm{x}, \mathrm{y})$ be a point in a quadrilateral element with nodes i, j, k, m as schematically sketched in Fig. 3.2. Here denote $\mathrm{S}_i, \mathrm{S}_j, \mathrm{S}_k, \mathrm{S}_m$ elements that share nodes i, j, k, m, respectively. The supporting nodes for the point $\mathbf{x}$ in the CQ4 element involve all nodes of elements $\mathrm{S}_i, \mathrm{S}_j, \mathrm{S}_k, \mathrm{S}_m$.

The CQ4 support domain for point $\mathbf{x}$ is much larger than the standard FEM support domain, and the trial solution at point $\mathbf{x}$ can be written as

$$u^h(\mathbf{x}) = \sum_{f=1}^{n_s} \tilde{N}_f(\mathbf{x}) d_f = \tilde{\mathbf{N}}(\mathbf{x})\mathbf{d} \tag{3.8}$$

In Eq. (3.8), the consecutive-interpolation shape function $\tilde{N}_f$ is determined by

$$\begin{aligned} \tilde{N}_f = {} & \underbrace{\phi_i N_f^{[i]} + \phi_{ix} \bar{N}_{f,x}^{[i]} + \phi_{iy} \bar{N}_{f,y}^{[i]}}_{\text{node } i} + \underbrace{\phi_j N_f^{[j]} + \phi_{jx} \bar{N}_{f,x}^{[j]} + \phi_{jy} \bar{N}_{f,y}^{[j]}}_{\text{node } j} \\ & + \underbrace{\phi_k N_f^{[k]} + \phi_{kx} \bar{N}_{f,x}^{[k]} + \phi_{ky} \bar{N}_{f,y}^{[k]}}_{\text{node } k} + \underbrace{\phi_m N_f^{[m]} + \phi_{mx} \bar{N}_{f,x}^{[m]} + \phi_{my} \bar{N}_{f,y}^{[m]}}_{\text{node } m} \end{aligned} \tag{3.9}$$

where d_f denotes the nodal displacement vector, while $N_f^{[i]}$ is the shape functions with respect to node i, and n_s is the total number of the supporting nodes in regard to the point of interest **x**. In the following interpretation, the formulation of average derivative of the shape functions at node i is given (similar for other nodes).

The average derivative of the shape functions at node i can be written as

$$\bar{N}^{[i]}_{f,x} = \sum_{e\in S_i}\left(w_e N^{[i][e]}_{f,x}\right) \; ; \; \bar{N}^{[i]}_{f,y} = \sum_{e\in S_i}\left(w_e N^{[i][e]}_{f,y}\right) \tag{3.10}$$

where the term $N^{[i][e]}_{f,x}$ is the derivative of $N^{[i]}_f$ computed in element e, and w_e is the weight function of element $\in S_i$, which is defined by

$$w_e = \frac{\Delta_e}{\sum_{\tilde{e}\in S_i}\Delta_{\tilde{e}}} \tag{3.11}$$

with Δ_e being the area of the element e.

In Eq. (3.9), the functions $\phi_i, \phi_{ix}, \phi_{iy}$ forming the polynomial basis associated with node i must satisfy the following conditions and the derivatives of the geometric interpolation functions can be defined as

$$\begin{aligned}
\frac{\partial \phi_i}{\partial L_i} &= 1 + 2L_iL_j + 2L_iL_k + 2L_iL_m - L_j^2 - L_k^2 - L_m^2 \\
\frac{\partial \phi_i}{\partial L_j} &= L_i^2 - 2L_iL_j \\
\frac{\partial \phi_i}{\partial L_k} &= L_i^2 - 2L_iL_k \\
\frac{\partial \phi_i}{\partial L_m} &= L_i^2 - 2L_iL_m \\
\frac{\partial \phi_{ix}}{\partial L_i} &= -\left(x_i - x_j\right)\left(2L_iL_j + pL_jL_k + pL_jL_m\right) \\
&\quad -(x_i - x_k)\left(2L_iL_k + pL_kL_m + pL_kL_j\right) \\
&\quad -(x_i - x_m)\left(2L_iL_m + pL_mL_j + pL_mL_k\right) \\
\frac{\partial \phi_{ix}}{\partial L_j} &= -\left(x_i - x_j\right)(L_i^2 + pL_iL_k + pL_iL_m)
\end{aligned} \tag{3.12}$$

$$-(x_i - x_k)(pL_iL_k) - (x_i - x_m)(pL_iL_m)$$

$$\frac{\partial \phi_{ix}}{\partial L_k} = -\left(x_i - x_j\right)\left(pL_iL_j\right) - (x_i - x_k)\left(L_i^2 + pL_iL_m + pL_iL_j\right)$$

$$-(x_i - x_m)(pL_iL_m)$$

$$\frac{\partial \phi_{ix}}{\partial L_m} = -\left(x_i - x_j\right)\left(pL_iL_j\right) - (x_i - x_k)(pL_iL_k)$$

$$-(x_i - x_m)\left(L_i^2 + pL_iL_j + pL_iL_k\right)$$

$$\frac{\partial \phi_{iy}}{\partial L_i} = -\left(y_i - y_j\right)\left(2L_iL_j + pL_jL_k + pL_jL_m\right)$$

$$-(y_i - y_k)\left(2L_iL_k + pL_kL_m + pL_kL_j\right)$$

$$-(y_i - y_m)\left(2L_iL_m + pL_mL_j + pL_mL_k\right)$$

$$\frac{\partial \phi_{iy}}{\partial L_j} = -\left(y_i - y_j\right)(L_i^2 + pL_iL_k + pL_iL_m)$$

$$-(y_i - y_k)(pL_iL_k) - (y_i - y_m)(pL_iL_m)$$

$$\frac{\partial \phi_{iy}}{\partial L_k} = -\left(y_i - y_j\right)\left(pL_iL_j\right) - (y_i - y_k)\left(L_i^2 + pL_iL_m + pL_iL_j\right)$$

$$-(y_i - y_m)(pL_iL_m)$$

$$\frac{\partial \phi_{iy}}{\partial L_m} = -\left(y_i - y_j\right)\left(pL_iL_j\right) - (y_i - y_k)(pL_iL_k)$$

$$-(y_i - y_m)\left(L_i^2 + pL_iL_j + pL_iL_k\right)$$

When $l \equiv i$, then $\xi = -1; \eta = -1$ and $L_i = 1;\ L_j = 0;\ L_k = 0;\ L_m = 0$, substituting these known values into aforementioned equations, $\phi_i(x_i) = 1$ can be obtained. In the same manner, when $l \equiv j;\ l \equiv k;\ l \equiv m$, the function $\phi_i(x_l)$ can be described as $\phi_i\left(x_j\right) = 0$; $\phi_i(x_k) = 0$; $\phi_i(x_m) = 0$, respectively.

When $l \equiv i$, then $\xi = -1; \eta = -1$ and $L_i = 1;\ L_j = 0;\ L_k = 0;\ L_m = 0$, the following equations can be obtained as well.

$$\begin{Bmatrix} \frac{\partial}{\partial \xi} \\ \frac{\partial}{\partial \eta} \end{Bmatrix} \begin{bmatrix} L_i & L_j & L_k & L_m \end{bmatrix} = \frac{1}{4}\begin{bmatrix} -2 & 2 & 0 & 0 \\ -2 & 0 & 0 & 2 \end{bmatrix} \tag{3.13}$$

$$\mathbf{J}^{-1} = \frac{1}{4\det(\mathbf{J})}\begin{bmatrix} -2y_i + 2y_m & 2y_i - 2y_j \\ 2x_i - 2x_m & -2x_i + 2x_j \end{bmatrix}$$

For the further manipulation

$$\begin{Bmatrix} \frac{\partial}{\partial x} \\ \frac{\partial}{\partial y} \end{Bmatrix} \begin{bmatrix} L_i & L_j & L_k & L_m \end{bmatrix} = \mathbf{J}^{-1} \begin{Bmatrix} \frac{\partial}{\partial \xi} \\ \frac{\partial}{\partial \eta} \end{Bmatrix} \begin{bmatrix} L_i & L_j & L_k & L_m \end{bmatrix}$$

$$= \frac{1}{4\det(\mathbf{J})}\begin{bmatrix} -2y_i + 2y_m & 2y_i - 2y_j \\ 2x_i - 2x_m & -2x_i + 2x_j \end{bmatrix} \frac{1}{4}\begin{bmatrix} -2 & 2 & 0 & 0 \\ -2 & 0 & 0 & 2 \end{bmatrix} \tag{3.14}$$

$$= \frac{1}{4\det(\mathbf{J})}\begin{bmatrix} y_j - y_m & y_m - y_i & 0 & y_i - y_j \\ x_m - x_j & x_i - x_m & 0 & x_j - x_i \end{bmatrix}$$

Based on the following relationship:

$$\frac{\partial \phi}{\partial L_i} = 1; \ \frac{\partial \phi}{\partial L_j} = 1; \ \frac{\partial \phi}{\partial L_k} = 1; \ \frac{\partial \phi}{\partial L_m} = 1; \tag{3.15}$$

The following equations can be obtained:

$$\phi_{i,x}(x_i) = \frac{\partial \phi_i}{\partial x} = \begin{bmatrix} \frac{\partial \phi_i}{\partial L_i} & \frac{\partial \phi_i}{\partial L_j} & \frac{\partial \phi_i}{\partial L_k} & \frac{\partial \phi_i}{\partial L_m} \end{bmatrix} \begin{bmatrix} \frac{\partial L_i}{\partial x} \\ \frac{\partial L_j}{\partial x} \\ \frac{\partial L_k}{\partial x} \\ \frac{\partial L_m}{\partial x} \end{bmatrix} \tag{3.16}$$

$$= \begin{bmatrix} 1 & 1 & 1 & 1 \end{bmatrix} \frac{1}{4\det(\mathbf{J})} \begin{bmatrix} y_j - y_m \\ y_m - y_i \\ 0 \\ y_i - y_j \end{bmatrix}$$

$$= \frac{1}{4\det(\mathbf{J})}\left[y_j - y_m + y_m - y_i + y_i - y_j\right] = 0$$

$$\phi_{i,y}(x_i) = \frac{\partial \phi_i}{\partial y} = \begin{bmatrix} \frac{\partial \phi_i}{\partial L_i} & \frac{\partial \phi_i}{\partial L_j} & \frac{\partial \phi_i}{\partial L_k} & \frac{\partial \phi_i}{\partial L_m} \end{bmatrix} \begin{bmatrix} \frac{\partial L_i}{\partial y} \\ \frac{\partial L_j}{\partial y} \\ \frac{\partial L_k}{\partial y} \\ \frac{\partial L_m}{\partial y} \end{bmatrix} \tag{3.17}$$

$$= [1 \quad 1 \quad 1 \quad 1] \frac{1}{4\det(\mathbf{J})} \begin{bmatrix} x_m - x_j \\ x_i - x_m \\ 0 \\ x_j - x_i \end{bmatrix}$$

$$= \frac{1}{4\det(\mathbf{J})} \left[x_m - x_j + x_i - x_m + x_j - x_i \right] = 0$$

Similarly, it is straightforward to prove the same for $l \equiv j,$ $l \equiv k,$ or $l \equiv m,$ as well as other conditions.

Therefore, the condition can be summarized as:

$$\begin{aligned} &\phi_i(\mathbf{x}_l) = \delta_{il}, \quad \phi_{i,x}(\mathbf{x}_l) = 0, \quad \phi_{i,y}(\mathbf{x}_l) = 0, \\ &\phi_{ix}(\mathbf{x}_l) = 0, \quad \phi_{ix,x}(\mathbf{x}_l) = \delta_{il}, \quad \phi_{ix,y}(\mathbf{x}_l) = 0, \\ &\phi_{iy}(\mathbf{x}_l) = 0, \quad \phi_{iy,x}(\mathbf{x}_l) = 0, \quad \phi_{iy,y}(\mathbf{x}_l) = \delta_{il}, \end{aligned} \tag{3.18}$$

where l is any one of the indices $i, j, k, m,$ and

$$\delta_{il} = \begin{cases} 1 & \text{if} \quad i = l \\ 0 & \text{if} \quad i \neq l \end{cases} \tag{3.19}$$

Note that the above conditions have to be applied in a similar manner to other functions, i.e., $\phi_j, \phi_{jx}, \phi_{jy}$, $\phi_k, \phi_{kx}, \phi_{ky}$ and $\phi_m, \phi_{mx}, \phi_{my}$. These polynomial basis functions $\phi_i, \phi_{ix}, \phi_{iy}$ for the CQ4 element are given by

$$\begin{aligned} \phi_i &= L_i + L_i^2 L_j + L_i^2 L_k + L_i^2 L_m - L_i L_j^2 - L_i L_k^2 - L_i L_m^2, \\ \phi_{ix} &= -(x_i - x_j)(L_i^2 L_j + pL_i L_j L_k + pL_i L_j L_m) \\ &\quad - (x_i - x_k)(L_i^2 L_k + pL_i L_k L_m + pL_i L_k L_j) \\ &\quad - (x_i - x_m)(L_i^2 L_m + pL_i L_m L_j + pL_i L_m L_k), \end{aligned} \tag{3.20}$$

$$\begin{aligned}\phi_{iy} = &-(y_i - y_j)(L_i^2 L_j + pL_i L_j L_k + pL_i L_j L_m) \\ &-(y_i - y_k)(L_i^2 L_k + pL_i L_k L_m + pL_i L_k L_j) \\ &-(y_i - y_m)(L_i^2 L_m + pL_i L_m L_j + pL_i L_m L_k).\end{aligned}$$

In Eq. (3.20) $p = 1/2$, and the functions $\phi_j, \phi_{jx}, \phi_{jy}$, $\phi_k, \phi_{kx}, \phi_{ky}$ and $\phi_m, \phi_{mx}, \phi_{my}$ can be also calculated in the same manner by a circulatory permutation of indices i, j, k, m. In addition, L_i, L_j, L_k, L_m are the area coordinates of the point of interest $\mathbf{x}$ in the quadrilateral element i, j, k, m.

3.3.2 Illustration of CQ4 shape function

Fig. 3.3 typically depicts the shape functions of the classical Q4 and CQ4 elements in one-dimension. As expected the CQ4 shape functions behave smoother than that of the common Q4, and interestingly it is found the same in 2D case, e.g., see Figs. 3.4(a) and (b). The first-order derivatives of the CQ4 shape functions are also sketched in Figs. 3.4(c) and (d), respectively, for better observations. The smoother behavior of the CQ4 shape functions is one of its important features as compared with the traditional cases.

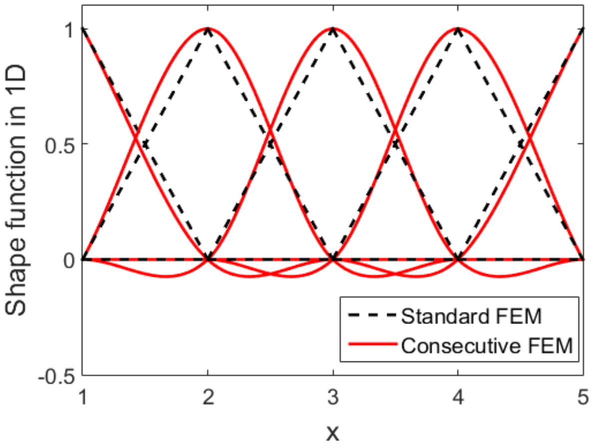

Fig. 3.3 Comparison of the standard and consecutive FEM shape functions in 1D space.

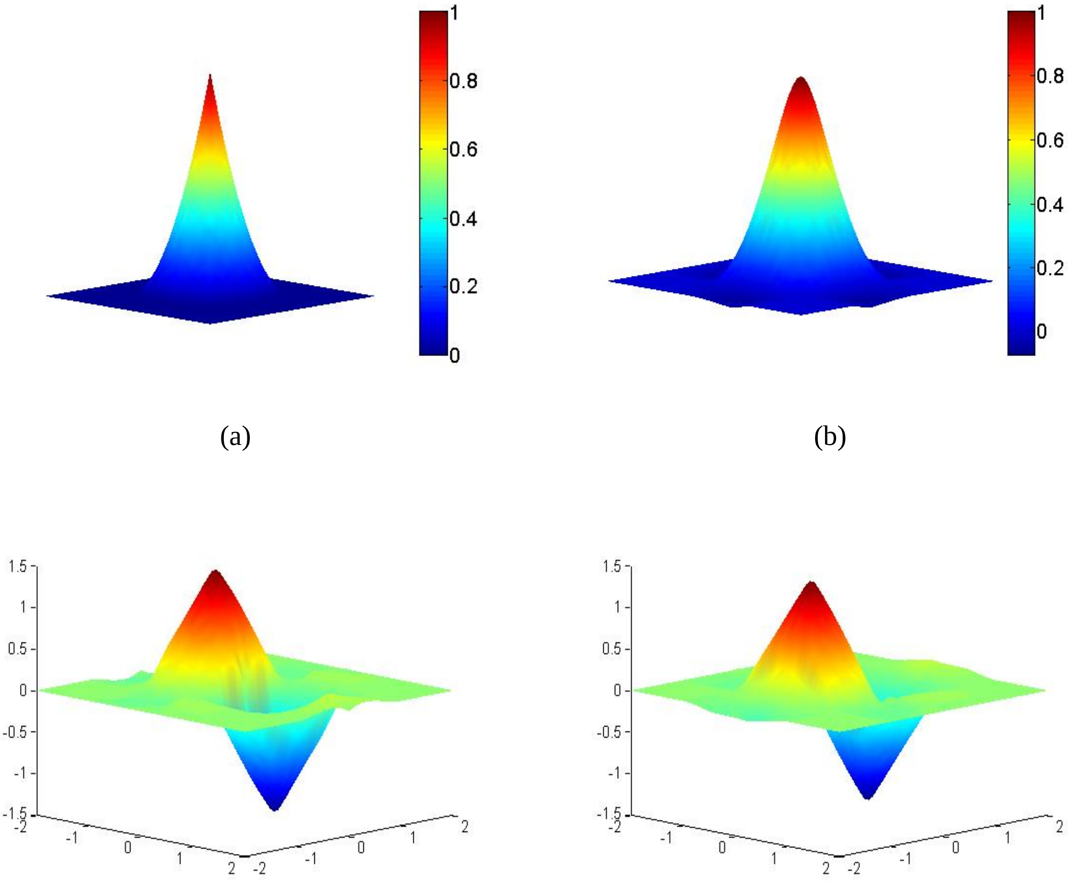

(a) (b)

(c) (d)

Fig. 3.4 Schematic interpretation of the standard FEM shape function (a) and the consecutive-interpolation shape function (b) in 2D space. The first derivative of the consecutive shape function with respect to x variable (c) and y variable (d) is shown.

It is very important to see that the CQ4 shape functions are complete polynomials, satisfy properties of the partition of unity, and possess Kronecker's delta function property. It is obvious that they are not rational polynomials, and the stiffness can be as accurately computed as those for regular Q4 elements. The shape functions are C^{∞} in the element interior, C^{1} at nodes and C^{0} on element edges. However, there are some nodes, for instance the nodes located on the essential boundary or on the interface of bi-materials, are required for the CQ4 to recover to a C^{0} continuity. A slight modification hence may be performed on those nodes. It is also interesting to highlight that the CQ4 will be degenerated into the standard Q4 element if all the nodes in the problem domain are supposed to be C^0.

3.4 XCQ4 Problem Formulation

Consider a domain Ω with a crack as shown in Fig. 3.5. The domain is subjected to a uniform body forces $\mathbf{b}$ and includes crack faces Γ_c, displacement boundary Γ_u and traction boundary Γ_t. Both traction force and displacement boundary conditions are considered, while the crack faces are set to be traction free.

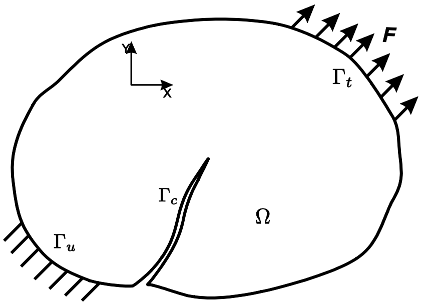

Fig. 3.5 Body containing a crack.

The strong form of equilibrium equation is as follows:

$$\nabla \cdot \boldsymbol{\sigma} + \mathbf{b} = 0 \quad \text{in } \Omega \tag{3.21}$$

The boundary conditions are:

$$\begin{aligned} \boldsymbol{\sigma} \cdot \mathbf{n} &= \boldsymbol{F} \quad \text{on } \Gamma_t \\ \boldsymbol{\sigma} \cdot \mathbf{n} &= 0 \quad \text{on } \Gamma_c \\ \mathbf{u} &= \bar{\mathrm{u}} \quad \text{on } \Gamma_u \end{aligned} \tag{3.22}$$

where $\mathbf{n}$ is the unit normal vector, $\boldsymbol{\sigma}$ is the Cauchy stress.

Considering the assumption of small strains and displacements, the elastic strains $\boldsymbol{\epsilon}$ are defined in terms of kinematic equations as follows:

$$\boldsymbol{\epsilon} = \frac{1}{2}(\boldsymbol{\nabla u} + (\boldsymbol{\nabla u})^T) = \nabla_s \mathbf{u} \tag{3.23}$$

where the $\nabla_s \mathbf{u}$ is the symmetric part of the displacement gradient.

Based on the linear elastic and isotropic constitutive law, the equation with respect to the Hook's law is expressed as:

$$\boldsymbol{\sigma} = \boldsymbol{C} : \boldsymbol{\epsilon} \tag{3.24}$$

where $\boldsymbol{C}$ is the elastic material stiffness tensor.

The space of kinematically admissible displacement fields is given as

$$\boldsymbol{u} \in U = \{\boldsymbol{v} \in V : \boldsymbol{v} = 0 \text{ on } \Gamma_u\} \tag{3.25}$$

The space V allows for discontinuous displacements across Γ_c, respectively.

The weak form of the equilibrium equation ignoring the body force is defined as

$$\int_\Omega \boldsymbol{\sigma} : \boldsymbol{\epsilon}(\boldsymbol{v})\, dx = \int_{\Gamma_t} \boldsymbol{F} \cdot \boldsymbol{v}\, ds \quad \forall \boldsymbol{v} \in U \tag{3.26}$$

Furthermore, the discretized weak form turns into

$$\int_\Omega \boldsymbol{C}\boldsymbol{\epsilon}(\boldsymbol{u}^h) : \boldsymbol{\epsilon}(\boldsymbol{v}^h)\, dx = \int_{\Gamma_t} \boldsymbol{F} \cdot \boldsymbol{v}^h\, ds \quad \forall \boldsymbol{v}^h \in U^h \tag{3.27}$$

3.5 Discrete Pattern of Equilibrium Equation

The crucial idea behind the XFEM is to employ a displacement approximation that is capable of capturing arbitrary discontinuity and singularity near crack tip using the concept of partition of unity [Melenk and Babusk, 1996]. It is accomplished by handling appropriate enrichment functions with which the local displacement approximation around the crack is enhanced by adding discontinuous Heaviside function across the crack faces and the asymptotic branch functions around the crack tip. The enriched displacements approximation using the new XCQ4 element is carried out in a similar XFEM setting except the CQ4 shape functions based on the CIP scheme are taken instead. When the problem domain is discretized by finite elements with I^s being the nodal set, as a result the extended CQ4 approximation of the displacements for cracks can be written as

$$\begin{aligned}\mathbf{u}^h(\mathbf{x}) = \sum_{i \in I^{\mathrm{s}}} \tilde{N}_i(\mathbf{x})\mathbf{u}_i + \sum_{j \in J^{\mathrm{cut}}} \tilde{N}_j(\mathbf{x})\big[H(\mathbf{x}) - H(\mathbf{x}_j)\big]\mathbf{a}_j \\ + \sum_{k \in K^{\mathrm{tip}}} \tilde{N}_k(\mathbf{x}) \sum_{\alpha=1}^{4} \big[F^\alpha(\mathbf{x}) - F^\alpha(\mathbf{x}_k)\big]\mathbf{b}_k^\alpha\end{aligned} \tag{3.28}$$

where $\tilde{N}_i(\mathbf{x})$ are the CQ4 shape functions associated with the node i that construct the partition of unity. J^{cut} is the set of enriched nodes associated with crack faces whose support domain is cut by the crack, while K^{tip} is the set of enriched nodes associated with crack tips whose support domain contains crack tips. $\mathbf{u}_i$ is the vector of the nodal degrees of freedom (DOFs) of node i, containing the nodal displacements. In addition, $H(\mathbf{x})$ is the modified Heaviside step function, which takes on the value of +1 above the crack and -1 below the crack, enabling the modeling of a crack that fully cuts a finite element. $\mathbf{a}_i$ is the vectors of the nodal enriched DOFs in the elements containing the crack associated with the discontinuous Heaviside function. The last term of Eq. (3.28) $F^{\alpha}(\mathbf{x})$ $(\alpha = 1,2,3,4)$ are the asymptotic branch crack tip enrichment functions and $\mathbf{b}_k^{\alpha}$ is the vectors of the additionally nodal enriched DOFs in the elements containing the crack tip associated with branch functions $F^{\alpha}(\mathbf{x})$.

For 2D linear isotropic elasticity problems, the asymptotic crack-tip enrichment functions $F^{\alpha}(\mathbf{x})$ are given by [Belytschko et al., 1999]

$$\left[F^{\alpha}(\mathbf{x}), \alpha = 1,\cdots,4\right] = \begin{bmatrix} \sqrt{r}\sin\left(\dfrac{\theta}{2}\right) \\ \sqrt{r}\cos\left(\dfrac{\theta}{2}\right) \\ \sqrt{r}\sin\left(\dfrac{\theta}{2}\right)\sin(\theta) \\ \sqrt{r}\cos\left(\dfrac{\theta}{2}\right)\sin(\theta) \end{bmatrix} \tag{3.29}$$

where (r, θ) is a polar coordinate system with its origin at the crack tip. Note that the first function in Eq. (3.29), $\sqrt{r}\sin(\theta/2)$ is discontinuous across the crack faces while the other three functions are continuous [Belytschko et al., 1999]. For a better representation and for the sake of completeness, Fig. 3.6 visualizes such four functions.

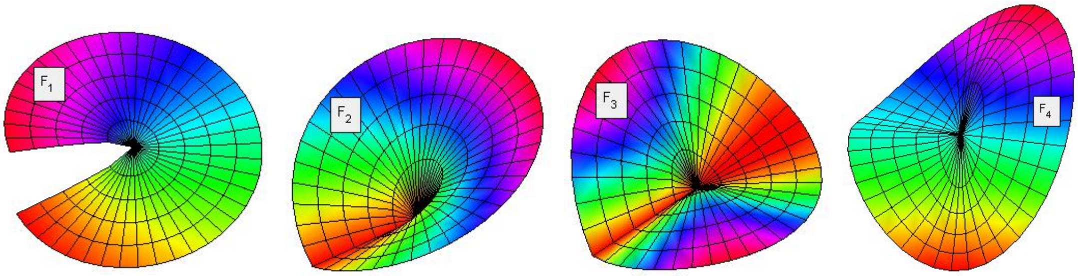

Fig. 3.6 Schematic representation of the fourfold enrichment functions of isotropic materials in Eq. (3.29)

Fig. 3.7(a) schematically illustrates 1D example of the Heaviside enrichment function for the elements cut by the crack. The element containing a discontinuity induced by crack at position $x = 2.5$ is supported by several shape functions, and the Heaviside function is then multiplied with those shape functions to model the discontinuity as sketched in Fig. 3.7(b). For 2D cases, the Heaviside enriched standard shape functions and the Heaviside enriched CIP shape functions are additionally plotted in Figs. 3.7(c) and (d), respectively. One important feature can be observed in the figures is that the shape functions with the CIP scheme are always smoother than that without the CIP.

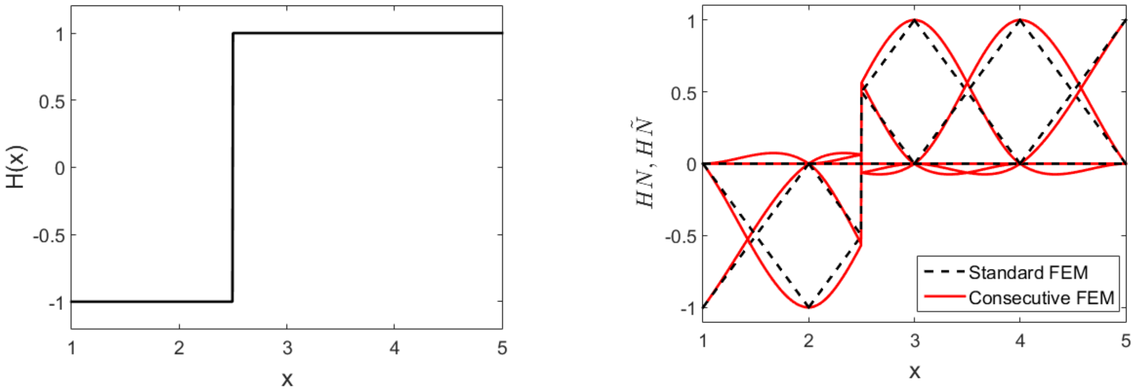

(a)

(b)

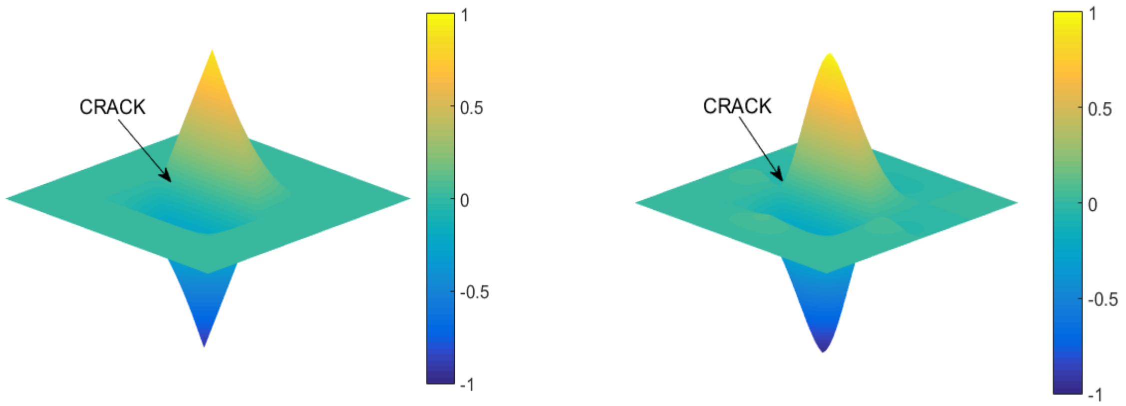

(c) (d)

Fig. 3.7 Illustration of 1D example of enrichment function for elements cut by the crack using the conventional and CIP FEM: (a) the Heaviside function in 1D; (b) a comparison of the multiplication of the Heaviside enrichment function and the standard (HN) and consecutive (HN) shape function in 1D space for the element at the discontinuous position $x = 2.5$. Similarly, (c) the multiplication of the Heaviside enriched function and the standard shape function (HN) in 2D space; and (d) for (HN).

3.5.1 Ramp function

In the linear elastic fracture mechanics the stress and displacement field in the vicinity of crack tip is always singular, which generates a difficulty in capturing the discontinuity. In XFEM the branch functions derived from linear elasticity containing the function $\sqrt{r}\sin(\theta/2)$ (See Eq. (3.29)) have the effect on seizing the discontinuity via the approximate interpolation in crack tip element. In other words the branch functions reflect the foundation of asymptotic field around the crack tip. Accordingly the problem of additional degrees of freedom at each asymptotic enriched node occurred and relatively more computational time is required because of four components of branch functions. For this reason the ramp function [Xia et al., 2012; Kumar et al., 2016] along Heaviside function is proposed to replace the fourfold functions for enriching the field near the crack tip, which is also available for solving the issues without knowing the analytical solution and the order of singularity in the circumstance of inelastic material behavior. It should be noted that the number of crack tip enriched function decreases from four to one. In such conditions the new displacement approximation can be written as:

$$\begin{aligned}\mathbf{u}^h(\mathbf{x}) = &\sum_{i\in I^{\mathrm{s}}} \tilde{N}_i(\mathbf{x})\mathbf{u}_i + \sum_{j\in J^{\mathrm{cut}}} \tilde{N}_j(\mathbf{x})\left[H(\mathbf{x}) - H(\mathbf{x}_j)\right]\mathbf{a}_j \\ &+ \sum_{k\in K^{\mathrm{tip}}} \tilde{N}_k(\mathbf{x})\left[H(\mathbf{x}) - H(\mathbf{x}_k)\right]R\left(\mathbf{x}\right)\mathbf{b}_k\end{aligned} \tag{3.30}$$

where the ramp function $R(\mathbf{x})$ along with the Heaviside function is identical with the branch functions of reflecting the asymptotic filed around the crack tip. Two kinds of ramp function are provided to play the vital role in enriching the crack tip element. A linear and cubic (high order) ramp functions are defined as Eqs. (3.31) and (3.32) respectively.

$$R\left(\xi\right) = \begin{cases} -\dfrac{\xi}{l_c} & \text{if} \quad \xi \le 0 \\ 0 & \text{if} \quad \xi > 0 \end{cases} \tag{3.31}$$

$$R\left(\xi\right) = \begin{cases} 3\left(\dfrac{\xi}{l_c}\right)^2 + 2\left(\dfrac{\xi}{l_c}\right)^3 & \text{if} \quad \xi \le 0 \\ 0 & \text{if} \quad \xi > 0 \end{cases} \tag{3.32}$$

The relevant coordinate system is depicted in Fig. 3.8. It can be observed that $(\tilde{\xi},\tilde{\eta})$ is the local natural coordinate system of crack tip while (ξ,η) is natural coordinate system. Thus $\tilde{\xi}$ in Eqs. (3.31) and (3.32) denotes the projection with respect to $\tilde{\xi}$ axis of each query node in crack tip element. l_c is the segmental crack length which is calculated only in crack tip element. The graphic characteristic of linear and cubic ramp function is shown in Fig. 3.9.

At the same time, when the linear function and the higher order polynomial function are used, their derivatives must be considered. Thus, the derivative for the linear function is:

$$\begin{aligned}\frac{\partial R(\boldsymbol{\xi})}{\partial \xi} &= -\frac{1}{l_c}\frac{\partial \tilde{\xi}}{\partial \xi} = -\frac{1}{l_c} cos\beta \\ \frac{\partial R(\boldsymbol{\eta})}{\partial \eta} &= -\frac{1}{l_c}\frac{\partial \tilde{\eta}}{\partial \eta} = -\frac{1}{l_c} sin\beta\end{aligned} \tag{3.33}$$

and for the polynomial function is:

$$\begin{aligned}\frac{\partial R(\boldsymbol{\xi})}{\partial \xi} &= \frac{6}{l_c}\frac{\partial \tilde{\xi}}{\partial \xi}\left(\frac{\tilde{\xi}}{l_c}\right) + \frac{6}{l_c}\frac{\partial \tilde{\xi}}{\partial \xi}\left(\frac{\tilde{\xi}}{l_c}\right)^2 \\ &= \frac{6}{l_c} cos\beta\left(\frac{\tilde{\xi}}{l_c}\right) + \frac{6}{l_c} cos\beta\left(\frac{\tilde{\xi}}{l_c}\right)^2 \\ \frac{\partial R(\boldsymbol{\xi})}{\partial \eta} &= \frac{6}{l_c}\frac{\partial \tilde{\xi}}{\partial \eta}\left(\frac{\tilde{\xi}}{l_c}\right) + \frac{6}{l_c}\frac{\partial \tilde{\xi}}{\partial \eta}\left(\frac{\tilde{\xi}}{l_c}\right)^2 \\ &= \frac{6}{l_c} sin\beta\left(\frac{\tilde{\xi}}{l_c}\right) + \frac{6}{l_c} sin\beta\left(\frac{\tilde{\xi}}{l_c}\right)^2 \end{aligned} \tag{3.34}$$

where β is the angle between local and global coordinate system.

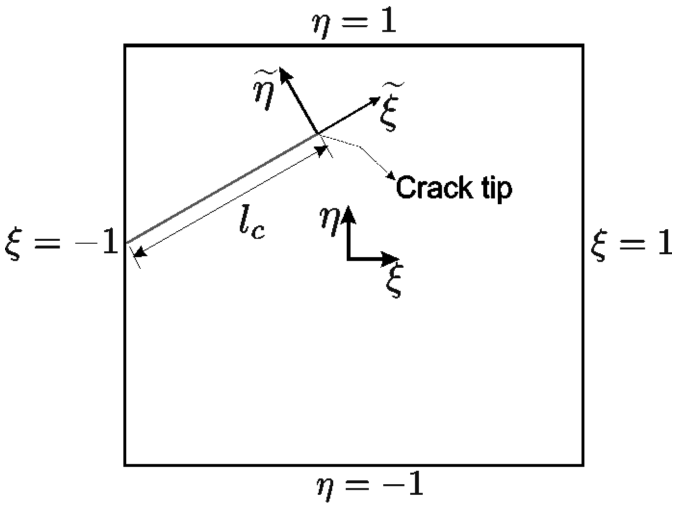

Fig. 3.8 Natural coordinates for a 4-node quadrilateral element.

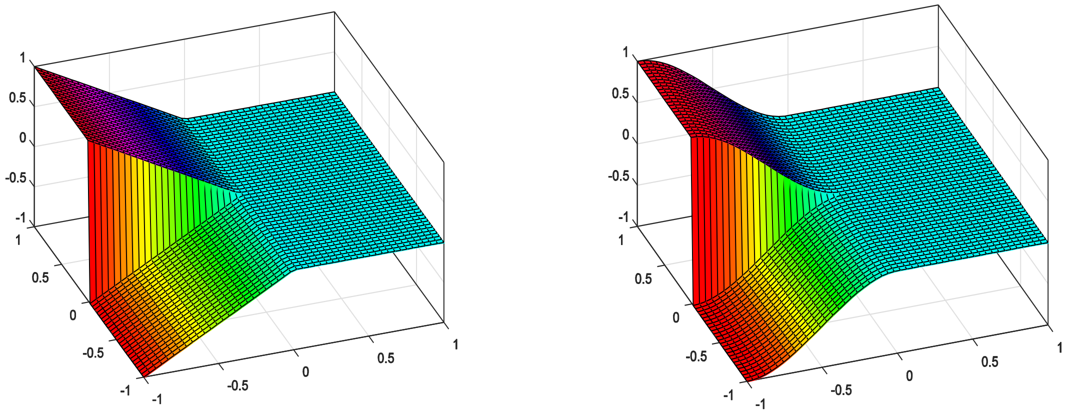

(a)

(b)

Fig. 3.9 Linear (a) and cubic (b) ramp function along with Heaviside function.

3.5.2 Modified Function for Enriched Nodes

The support domains of Heaviside enriched node for a continuous element e and a crack tip enriched node i are schematically shown in Fig. 3.10. It can be recognized that the support domain with respect to enriched node would result in the continuity of the corresponding site relaxing to C^0 as the nodal derivatives computed by the CIP are not continuous owing to the discontinuity [Zheng et al., 2010; Wu et al., 2012]. Still some nodes along the material interfaces or boundaries also need to be modified to meet the requirement about continuity. It thus is indispensable to take some measures to settle the circumstance caused by the enriched nodes. One alternative option is to improve the computation of the average nodal gradient for enriched nodes as

$$\bar{N}^{[i]}_{f,x} = N^{[i][e]}_{f,x} \tag{3.35}$$

where the relevant definition of parameters can be found in Eq. (3.9).

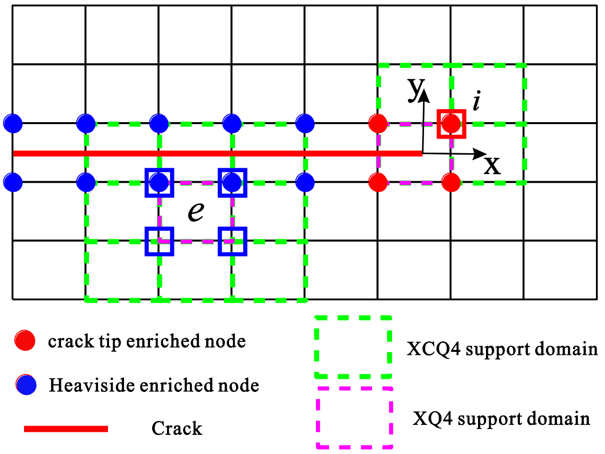

Fig. 3.10 Schematic representation of the support domains for XCQ4 and its enriched nodes.

3.5.3 Spatial Discretization of XCQ4

The discrete system of linear equilibrium equation under small displacement elasto-statics condition can be expressed as

$$\mathbf{K}\mathbf{d} = \mathbf{F} \tag{3.36}$$

where $\mathbf{K}$ is the global stiffness matrix, $\mathbf{d}$ is the global nodal displacement vector of the system including normal and enriched total DOFs. For enriched elements, the elementary stiffness matrix are obtained

$$\mathbf{k}_{ij}^{e} = \begin{bmatrix} \mathbf{k}_{ij}^{\mathbf{uu}} & \mathbf{k}_{ij}^{\mathbf{ua}} & \mathbf{k}_{ij}^{\mathbf{ub}} \\ \mathbf{k}_{ij}^{\mathbf{au}} & \mathbf{k}_{ij}^{\mathbf{aa}} & \mathbf{k}_{ij}^{\mathbf{ab}} \\ \mathbf{k}_{ij}^{\mathbf{bu}} & \mathbf{k}_{ij}^{\mathbf{ba}} & \mathbf{k}_{ij}^{\mathbf{bb}} \end{bmatrix} \tag{3.37}$$

whereas for the non-enriched elements

$$\mathbf{k}_{ij}^{e} = \mathbf{k}_{ij}^{\mathbf{uu}} \tag{3.38}$$

with

$$\mathbf{k}_{ij}^{rs} = \int_{\Omega^e} (\mathbf{B}_i^r)^{\mathrm{T}} \mathbf{C} (\mathbf{B}_j^s) d\Omega \;\; ; \qquad r,\, s \cong \mathbf{u},\, \mathbf{a}, \mathbf{b} \tag{3.39}$$

where $\mathbf{B}$ is the derivative of shape function and can be divided into classical strain-displacement matrix $\mathbf{B}_i^u$, Heaviside enriched strain-displacement matrix $\mathbf{B}_j^a$ and near crack tip enriched strain-displacement matrix $\mathbf{B}_k^{b\alpha}$. Due to the CIP shape functions, the new classical, Heaviside enriched and asymptotic enriched strain-displacement matrix are given by

$$\mathbf{B}_i^{\mathbf{u}} = \begin{bmatrix} \tilde{N}_{i,x} & 0 \\ 0 & \tilde{N}_{i,\mathrm{y}} \\ \tilde{N}_{i,\mathrm{y}} & \tilde{N}_{i,x} \end{bmatrix}; \;\; \mathbf{B}_j^{\mathbf{a}} = \begin{bmatrix} \left(\tilde{N}_j H\right)_{,x} & 0 \\ 0 & \left(\tilde{N}_j H\right)_{,\mathrm{y}} \\ \left(\tilde{N}_j H\right)_{,\mathrm{y}} & \left(\tilde{N}_j H\right)_{,x} \end{bmatrix};$$

$$\mathbf{B}_k^{\mathbf{b}\alpha}\big|_{\alpha=1,2,3,4} = \begin{bmatrix} \left(\tilde{N}_k F_\alpha\right)_{,x} & 0 \\ 0 & \left(\tilde{N}_k F_\alpha\right)_{,\mathrm{y}} \\ \left(\tilde{N}_k F_\alpha\right)_{,\mathrm{y}} & \left(\tilde{N}_k F_\alpha\right)_{,x} \end{bmatrix} \tag{3.40}$$

In Eq. (3.36), $\mathbf{F}$ is the vector of external nodal force and the element contribution to the global element force vector is given by

$$\mathbf{f}_i^{e} = \{\mathbf{f}_i^{\mathbf{u}}\; \mathbf{f}_i^{\mathbf{a}}\; \mathbf{f}_i^{\mathbf{b}1}\; \mathbf{f}_i^{\mathbf{b}2}\; \mathbf{f}_i^{\mathbf{b}3}\; \mathbf{f}_i^{\mathbf{b}4}\}^{\mathrm{T}} \tag{3.41}$$

for enriched elements, whereas

$$\mathbf{f}_i^e = \mathbf{f}_i^{\mathbf{u}} \tag{3.42}$$

for non-enriched elements, and their detailed components as

$$\mathbf{f}_i^{\mathbf{u}} = \int_{\partial\Omega^e} \tilde{N}_i \bar{\mathbf{t}} d\Gamma + \int_{\Omega^e} \tilde{N}_i \bar{\mathbf{b}} d\Omega \tag{3.43}$$

$$\mathbf{f}_i^{\mathbf{a}} = \int_{\partial\Omega^e} \tilde{N}_i \left[H(\mathbf{x}) - H(\mathbf{x}_i)\right] \bar{\mathbf{t}} d\Gamma + \int_{\Omega^e} \tilde{N}_i \left[H(\mathbf{x}) - H(\mathbf{x}_i)\right] \bar{\mathbf{b}} d\Omega \tag{3.44}$$

$$\mathbf{f}_i^{\mathbf{b}\alpha}\Big|_{\alpha=1,2,3,4} = \int_{\partial\Omega^e} \tilde{N}_i \left[F^\alpha(\mathbf{x}) - F^\alpha(\mathbf{x}_i)\right] \bar{\mathbf{t}} d\Gamma + \int_{\Omega^e} \tilde{N}_i \left[F^\alpha(\mathbf{x}) - F^\alpha(\mathbf{x}_i)\right] \bar{\mathbf{b}} d\Omega \tag{3.45}$$

where $\bar{\mathbf{b}}$ and $\bar{\mathbf{t}}$ represent the body force per unit volume and the prescribed tractions, respectively.

3.5.4 Interaction Integral and SIFs Calculation

To obtain the SIFs, the domain form of interaction integrals [Moës et al., 1999] is employed in this paper. Two states of a cracked body are considered. state #1 ($\sigma_{ij}^{(1)}$, $\varepsilon_{ij}^{(1)}$, $u_{ij}^{(1)}$) corresponds to the actual state while state #2 ($\sigma_{ij}^{(2)}$, $\varepsilon_{ij}^{(2)}$, $u_{ij}^{(2)}$) is an auxiliary state which is chosen as the asymptotic fields for modes I and II. In terms of aforementioned definition, the interaction integral with the mixed-mode SIFs can be written as

$$M^{(1,2)} = \int_\Gamma \left[W^{(1,2)} \delta_{1j} - \sigma_{ij}^{(1)} \frac{\partial u_i^2}{\partial x_1} - \sigma_{ij}^{(2)} \frac{\partial u_i^1}{\partial x_1} \right] n_j d\Gamma. \tag{3.46}$$

Since the interaction integral $M^{(1,2)}$ in Eq. (3.46) is not suited for the FEM implementation, it is hence transformed into an area integral by multiplying the integrand with a bounded weighting function $q(\mathbf{x})$, which is schematically represented in Fig. 3.11, the value of which is 1 on the open set containing the crack tip and 0 on the outer prescribed contour. Finally, the interaction integral in domain form is determined by

$$M^{(1,2)} = \int_A \left[\sigma_{ij}^{(1)} \frac{\partial u_i^2}{\partial x_1} + \sigma_{ij}^{(2)} \frac{\partial u_i^1}{\partial x_1} - W^{(1,2)} \delta_{1j} \right] \frac{\partial q}{\partial x_j} dA. \tag{3.47}$$

It must be noticed that by incorporating the CIP into the approximation, the support domain for the element belonging to J-domain in terms of the XCQ4 is larger than that of the standard XQ4. For instance, the J-domain is schematically depicted in Fig. 3.12(a) for the XQ4 and in Fig. 3.12(b) for the XCQ4, in which the function $q(\mathbf{x})$ varies from 0 to 1 in the marked yellow region. It is observed that the support domain determined by the XQ4 is smaller than that by the XCQ4 when calculating the SIFs. It is because the neighboring elements are also involved into the implementation of the interaction integral using the XCQ4 method, and thus gaining a higher accuracy of SIFs based on the XCQ4 is desirable. All the features of the XCQ4 element will be illustrated in the numerical results.

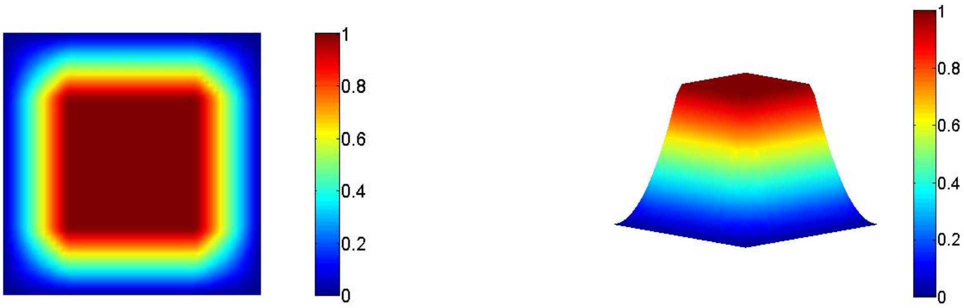

(a) (b)

Fig. 3.11 Schematic representation of the weighting function $q(\mathbf{x})$ used for implementing the interaction integral: (a) top-view and (b) front-view.

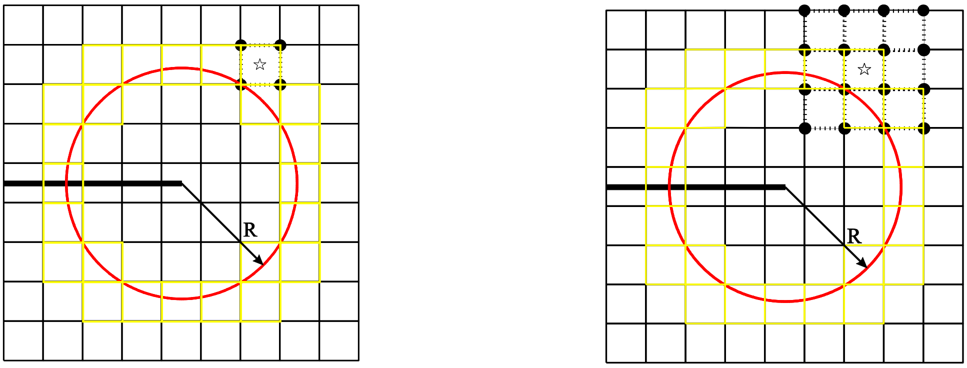

(a) (b)

Fig. 3.12 Illustration of the difference on the implementation of the J-domain between the XQ4 (a) and the XCQ4 (b). The support domain with an arbitrary element in J-domain tackled by the XCQ4 is larger than that by the common XQ4 because of the consecutive-interpolation procedure.

3.6 Desirable Properties of XCQ4 and Integration Order

Major desirable features of the proposed approach can be pointed out: (a) the crack can be modelled arbitrarily without considering the conformation between the fracture configuration and finite element mesh; (b) no remeshing is required in modeling the evolution of crack; (c) the post-processing of stress recovery in FEM is no longer required; (d) high accuracy of the output results of the crack path.

The effect of the number of Gaussian quadrature points on the static results is insignificant. It implies that higher numbers of quadrature points are not able to produce higher accuracy on the solutions. In this fracture modeling work, the standard Gauss quadrature rule is taken and it is applied to elements that do not contain any enriched nodes. High-order quadrature rule is applied to elements that contain enriched nodes, but are not cut by the crack, to enhance the accuracy of the solutions. On the other hand, the sub-division triangular method is adopted and apply it to elements that are cut by the crack or contain crack tips [Moës et al., 1999]. In the sub-triangles, high-order Gauss quadrature rules are used to ensure the accuracy.

Basically, for the elements cut by the crack the normal Gauss quadrature rule is incapable of integrating over the element as the precondition of employing divergence theorem is that the selected domain is regular enough and contain no discontinuity. If a discontinuity is present the field should be partitioned in some non-overlapped sub-domains to make the field continuous. Therefore, in this study the enriched elements are segmented into several sub triangles, which transform the role of discontinuity inside the domain into the boundary of the regenerated small domain such that the Gauss quadrature can progress smoothly. The value of quadrature points and weights could be acquired by looping over each regenerated sub-triangles, then the integration of week-form for prescribed element containing the discontinuity proceeds by cycling over per element belong to the XCQ4 support domain in regard to every integration point in triangular domain. It is noteworthy that the purpose of partitioning the element cut by the crack merely for the integration purpose, and so no additional degrees of freedom are augmented in whole domain.

3.7 Summary

This chapter introduce the extended 4-node quadrilateral finite element (XCQ4) based on consecutive-interpolation procedure (CIP) with continuous nodal stress for accurately modeling singular stress fields near crack tips of two-dimensional (2D) cracks in solids is presented. In contrast to classical methods, the approximation functions constructed based on the CIP involve both nodal values and averaged nodal gradients as interpolation conditions. The objective is to exhibit a pioneering extension of a recently developed CQ4 element enhanced by enrichment to precisely model 2D elastic crack problems, taking advantages of the strengths and making use all the desirable features of both techniques, the CIP and enrichment method.

For accurately modeling cracks XCQ4 approach adopted enrichments that include a discontinuous Heaviside function and the asymptotic near tip crack field to take advantage of characteristic of mesh independence. The enriched Heaviside function is used away from the crack tip as it is to capture the discontinuities across the crack faces while the asymptotic near tip field embedded in the approximation function to represent the singularities at the crack tip.

CHAPTER 4

CRACK ANALYSIS IN ELASTIC SOLIDS

4.1 Introduction

This chapter presents the application of the XCQ4 based on consecutive-interpolation procedure (CIP) with continuous nodal stress for accurately modeling singular stress fields near crack tips of two-dimensional (2D) cracks in solids. In contrast to classical methods, the approximation functions constructed based on the CIP involve both nodal values and averaged nodal gradients as interpolation conditions. The objective is to exhibit a pioneering extension of a recently developed CQ4 element enhanced by enrichment to precisely model 2D elastic crack problems, taking advantages of the strengths and making use all the desirable features of both techniques, the CIP and enrichment method. The stress intensity factors (SIFs) are estimated using the interaction integral. The accuracy and performance of the proposed XCQ4 and its numerical properties are illustrated through numerical examples, considering both single and mixed-mode problems with complicated configurations. The appropriate number of nodes at the initial step for each example is determined to avoid the neighboring elements including the crack tip element. The relevant results present here are taken from the paper published by [Kang et al., 2015]. Compared with reference solutions available in the literature and the conventional XQ4 results, it is found that the accuracy of the XCQ4 is high. Studies on the convergence rate of the SIFs in relative errors also reveal a better performance of the XCQ4 over the classical XQ4. The fracture parameters are found to be stable for different areas of integration paths around the crack tip. Further applications of the developed XCQ4 to other complex problems are potential.

4.2 A Three-point Bending Beam Containing An Edge Crack

4.2.1 Initial Conditions

By considering a three-point bending beam (TPB) containing an edge crack of length a as depicted in Fig. 4.1, the geometric parameters of the TPB are set to be $W = 6$ and $L = 12$. The beam is subjected to a concentrated force specified by $F = 1$, while the edge crack is assumed to locate at the mid-span of the TPB beam, as a result of only developing mode I crack. The analytical solutions for different crack lengths are given by [Srawley et al., 1976]. The beam is also analyzed previously by [Wu and Cai, 2014] using a partition of unity and numerical manifold method (PUM). All those available results are employed for the validation purpose.

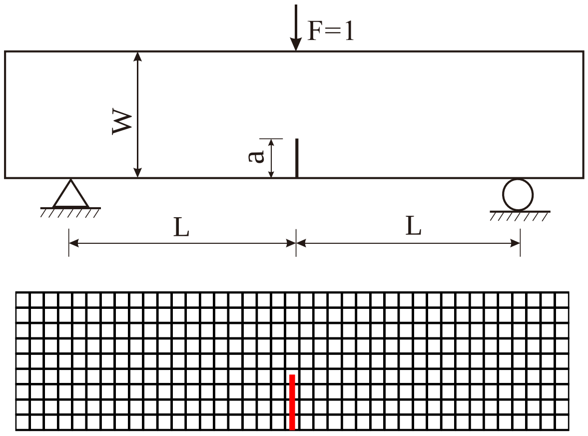

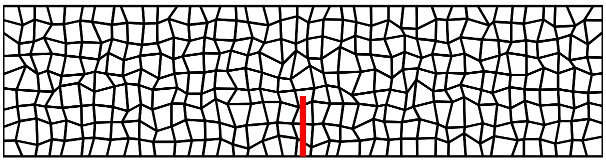

Fig. 4.1 Geometrical notation of a three point bending test specimen involving an edge crack showing its boundary and loading conditions. Typical regular and irregular (distorted) meshes of 9x39 elements of the TPB beam are shown.

4.2.2 Analysis of accuracy of Mode-I SIF

Firstly, the accuracy of the present formulation is analyzed and Table 4.1 hence presents a comparison of the calculated mode I SIF of the TPB beam among the XCQ4, XQ4, PUM and the analytical method. In Table 4.1, a convergence study of the SIF for different regular meshes and different crack lengths via the crack-length-to-width ratio a/W is also presented. More precisely, various ratios of a/W such as a/W = 0.3; 0.4 and 0.5 and several uniform meshes such as 10x40; 20x80; 30x120 and 40x160 nodes are considered. It is noted that the same numerical integration is applied to both the XQ4 and the XCQ4. It can be observed from the computed results of the mode I SIF that the variation of the SIF versus the ratio a/W is significant.

Table 4.1 Convergence of the SIFs with respect to mesh density of a three-point bending beam computed by the XCQ4, XQ4, PUM and the analytical methods.

a/W	Method	Mesh				PUM	Exact
		10×40	20×80	30×120	40×160		
0.3	XQ4	2.3503	2.4226	2.4427	2.4518	2.514	2.484
	XCQ4	2.3913	2.4508	2.4677	2.4751		
0.4	XQ4	3.0287	3.1456	3.1775	3.1918	3.25	3.236
	XCQ4	3.0673	3.1694	3.1988	3.2116		
0.5	XQ4	3.9956	4.1933	4.2471	4.2711	4.417	4.348
	XCQ4	4.0282	4.2162	4.2693	4.2935		

The larger the crack length increases the higher the mode I SIF is obtained, which can be seen clearly in Fig. 4.2. For a better observation, the comparison of the mode I SIF calculated by different approaches is also sketched in Fig. 4.3. From Table 4.1 and Figs. 4.2-4.3, one can easily be seen that the SIFs for three cases of a/W obtained by the present XCQ4 converge well to the exact solutions once the mesh density decreases. The common XQ4 interestingly behaves the same situation as the XCQ4 does, but its accuracy on the SIF is lower than that achieved by the XCQ4 using the same meshes. Additionally, higher values of the SIFs computed based on the PUM [Wu and Cai, 2014] for three cases of the ratio a/W over the analytical results can be observed in the figures. Loosely speaking, the PUM results could be thought as the upper bound solution whiles the present XCQ4 and XQ4 for the lower one.

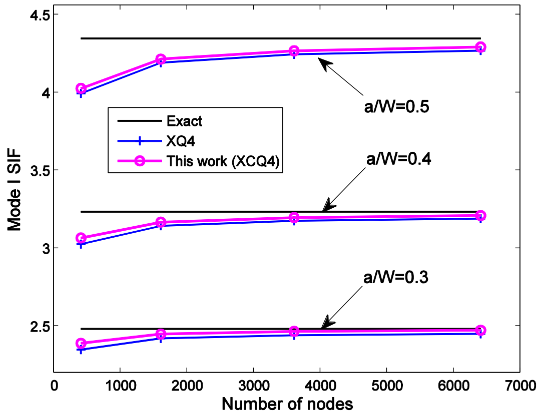

Fig. 4.2 Variation of the mode I SIF of a three-point bending beam for different crack-length-to-width ratios a/W.

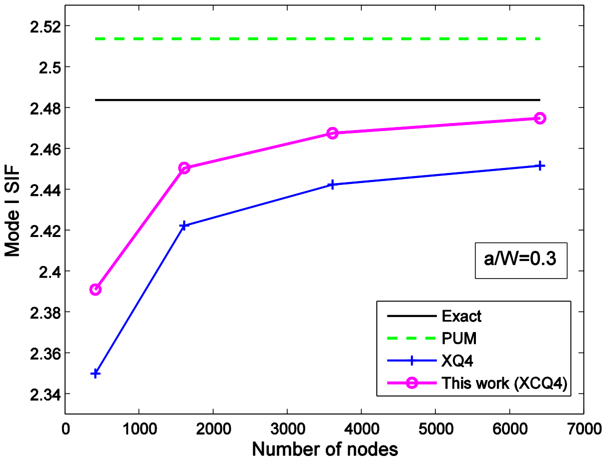

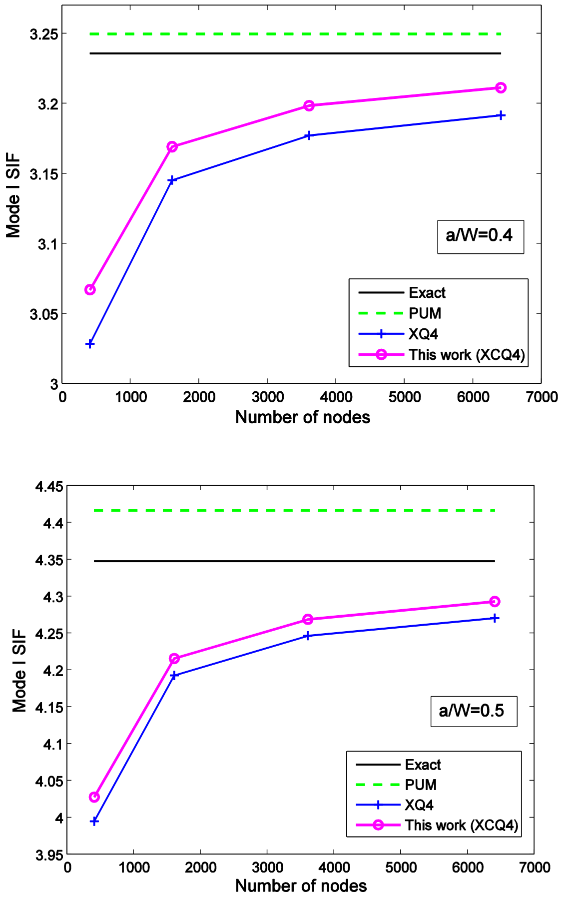

Fig. 4.3 Comparison of the computed mode I SIF of a three-point bending beam for different crack-length-to-width ratios a/W.

The irregular or distorted mesh affecting the mode I SIF is also studied. A typical distorted mesh is shown in Fig. 4.1. Table 4.2 presents the numerical results dealing with the effect of the distorted mesh on the mode I SIF of the TPB beam using a fine mesh of 40x160. The percentage errors (in parenthesis) estimated over the exact solutions for three cases of the ratios a/W are provided. Not surprisingly, the accuracy gained by the regular mesh is higher than that by the distorted one. In overall the numerical results indicate that the distorted mesh has a little effect on the accuracy.

Table 4.2 Effect of distorted mesh on the mode I SIF of a TPB beam.

a/W	This work		Exact
	Regular (39×159)	Irregular (39×159)	
0.3	2.4752 *(0.35)*	2.4816 *(0.09)*	2.484
0.4	3.2116 *(0.75)*	3.2001 *(1.11)*	3.236
0.5	4.2935 *(1.25)*	4.5209 *(3.97)*	4.348

4.2.3 Evaluation of Convergence Rate about Mode-I SIF

Next, the convergence rate of the mode I SIF by the present method using regular meshes is demonstrated through the log-log plots. The relative error of the SIF computed by Eq. (4.1) is hence plotted in Fig. 4.4, considering three cases of the ratio a/W =0.3, 0.4 and 0.5, respectively. As expected, the superior convergence rate for the XCQ4 can be obtained, and in comparison with the results computed by the common XQ4 element, the XCQ4 yields higher accuracy for all cases of the ratio a/W.

$$\mathrm{Re}=\frac{\left|K^{\mathrm{Numerical}}-K^{\mathrm{Exact}}\right|}{K^{\mathrm{Exact}}} \tag{4.1}$$

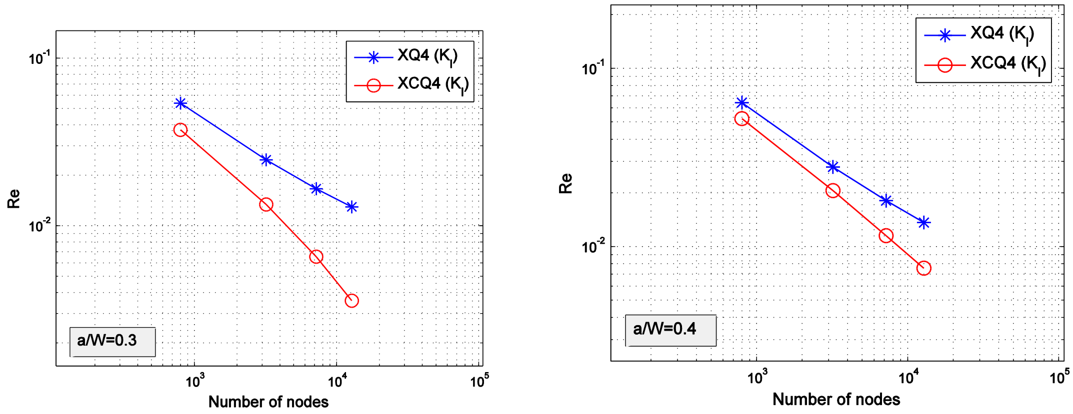

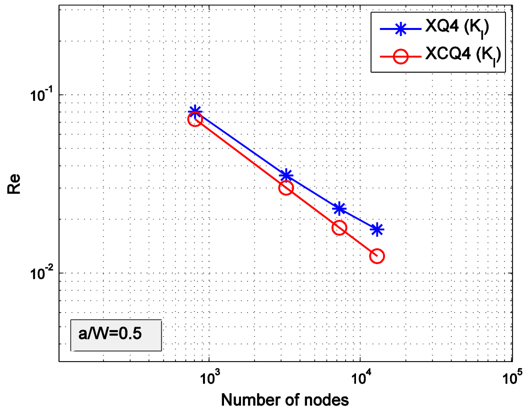

Fig. 4.4 Comparison of the convergence rate of the mode I SIF of a TPB beam for different ratios a/W between the XCQ4 and XQ4.

4.3 An Edge Crack under Shear and Tensile Load

Next example considers a finite rectangular plate with an edge crack either subjected to a uniform shear load or tensile load on the top of the plate. The geometry of these test specimens is schematically depicted in Fig. 4.5. The bottom edge of the specimens is fully clamped. The dimensionless geometric parameters for these specimens are set up as follows: the length of specimen $L = 16$, the width $W = 7$, and a crack length $a = 3.5$.

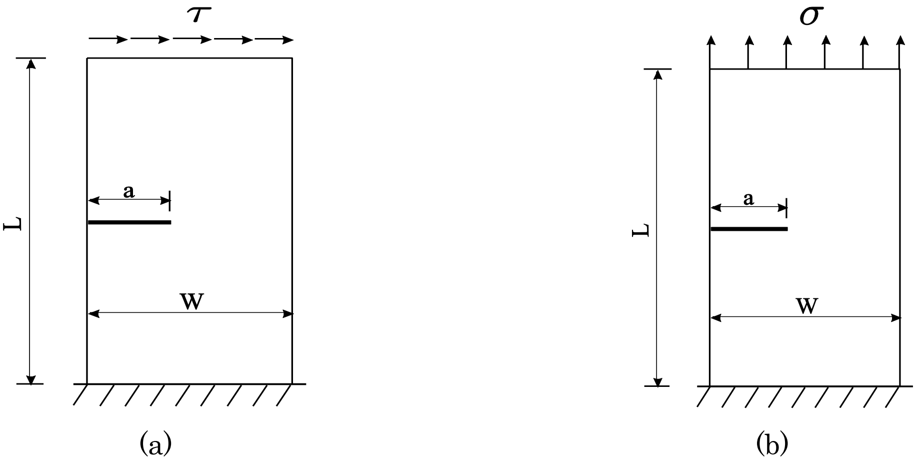

Fig. 4.5 Geometric notation of an edge crack under shear load (a) and tensile load (b) and its boundary condition.

4.3.1 Shear Loading

A shear load $\tau = 1$ subjected to the top of the plate is considered. This is a mixed-mode problem. The exact solutions of the mixed-mode SIFs for this case of shear loading condition [Moës et al., 1999], $K_I = 34.0$ and $K_{II} = 4.55$, are used for the comparison purpose.

The influence of the J-integral domain radius R, as depicted in Fig. 3.12 above, on the SIFs in terms of the developed XCQ4 and the common XQ4 is numerically investigated. Three different values of the J-domain radius such as R = 2, 2.5 and 3 are taken while four regular meshes of 10x20; 20x40; 30x60 and 40x80 nodes are used. The corresponding results of the SIFs for each radius are computed and presented in Table 4.3. The calculated numerical results are very interesting. It is obvious that the accuracy of the SIFs increases and approaches to the exact solutions with increasing the number of elements. Once again, it can be seen in the table that the developed XCQ4 offers higher accuracy on the SIFs than the common XQ4. The variation and the effect of the selected domain radii on the mixed-mode SIFs are insignificant. However, a not too large and not too small domain radius is often selected for the analysis to ensure not to lose the accuracy of the method. Previously, the influence of this parameter on the dynamic SIFs is also analyzed in a similar setting, but for a singular element, e.g., see [Liu et al., 2012]. In general R = 2, 2.5 or 3 can be used.

The relative error in mode-I and mode-II SIFs accounted for different domain radii are sketched in Fig. 4.6 in which both solutions derived from the XCQ4 and the common XQ4 are shown. The convergences for both modes behave in a similar situation, implying that the convergence rate of the XCQ4 for different R is better than that of the XQ4 for both modes. Consequently, the XCQ4 performs better in tensile and shear/sliding failure modes than the traditional XQ4 element.

Table 4.3 Convergence of the SIFs against mesh density for an edge crack under shear loading. The analytical solutions is $K_I = 34.0$ and $K_{II} = 4.55$.

R		Method	Mesh			
			10×20	20×40	30×60	40×80
2	K_I	XQ4	31.3742	33.0055	33.4473	33.6480
		XCQ4	31.7094	33.1934	33.6175	33.8123
	K_{II}	XQ4	4.4075	4.4632	4.4775	4.4839
		XCQ4	4.4987	4.5301	4.5635	4.5553
2.5	K_I	XQ4	31.1810	32.8235	33.2693	33.4731
		XCQ4	31.5365	33.0080	33.4352	33.6361
	K_{II}	XQ4	4.3953	4.4522	4.4698	4.4774
		XCQ4	4.4467	4.4764	4.4838	4.4911
3	K_I	XQ4	31.2015	32.8516	33.3274	33.5318
		XCQ4	31.3362	33.0001	33.4795	33.6808
	K_{II}	XQ4	4.3912	4.4477	4.4664	4.4737
		XCQ4	4.4265	4.4563	4.4709	4.4989

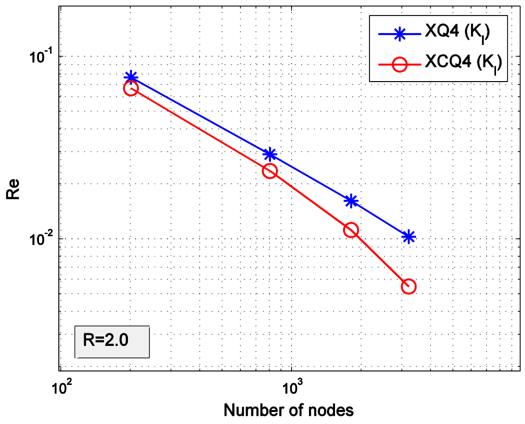

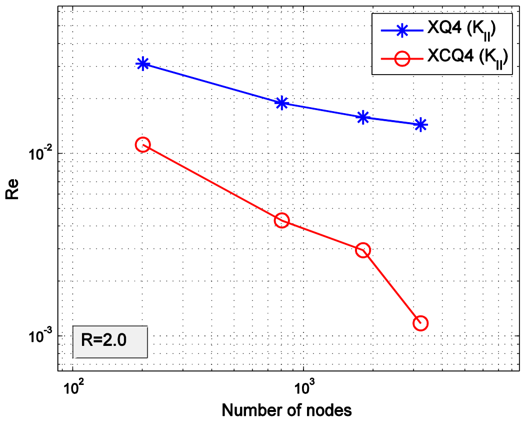

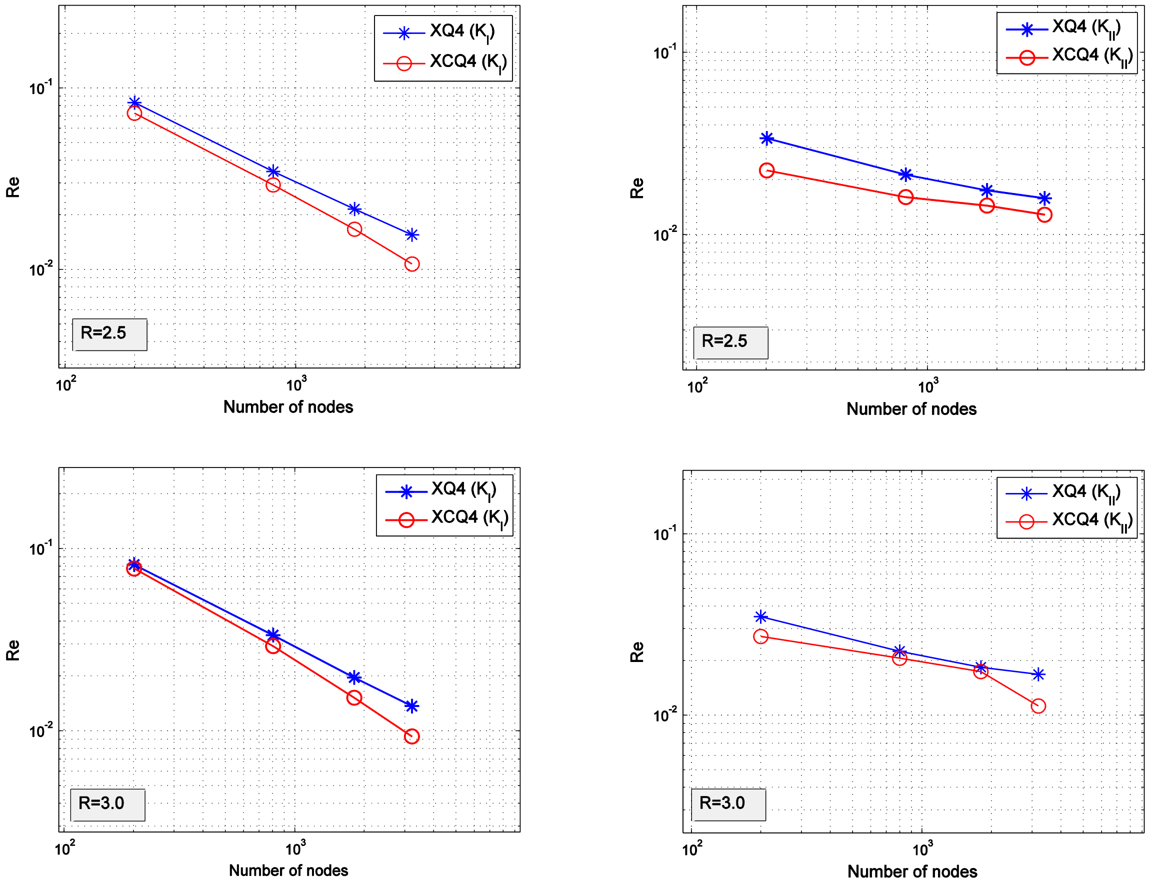

Fig. 4.6 Convergence results of mode I and II of an edge crack under shear loading obtained by the XCQ4 and XQ4 for different R.

4.3.2 Tensile Loading

A tensile loading as shown in Fig. 4.5(b) is studied. The specimen is subjected to $\sigma = 1$ on the top of the plate, and under such condition only mode I can develop. Similar to the shear loading case, the influence of the domain radius on the SIF is investigated, but only $R = 2$ and 2.5 are examined in this tensile loading case. The convergence of the SIF versus meshes is also explored. The numerical mode I SIF is validated against the analytical solutions given by [Ewalds and Wanhill, 1989]

$$K_I = C\sigma\sqrt{\pi a} \tag{4.2}$$

where the correction coefficient is determined by

$$C = 1.12 - 0.231\left(\frac{a}{W}\right) + 10.55\left(\frac{a}{W^2}\right) - 21.72\left(\frac{a}{W}\right)^3 + 30.39\left(\frac{a}{W}\right)^4 \tag{4.3}$$

The computed results and the exact values of mode I SIF is thus presented in Table 4.4, which shows higher accuracy of the mode I SIF gained by the XCQ4 than the conventional XQ4. Approaching to the exact solutions once the number of elements increasing can be found for the XCQ4. Basically, the same conclusion conducted in the previous example for the influence of the J-domain radius can also be found in this tension loading specimen. Furthermore, the relative error in mode I SIFs for the diverse discretization and J-integral domain radius R are illustrated in Fig. 4.7. The XCQ4 again performs better than the XQ4.

Table 4.4 Convergence of the mode I against mesh density for an edge crack under tension loading.

R	Method	Mesh				Ref.
		10×20	20×40	30×60	40×80	
2	XQ4	8.7292	9.1050	9.2137	9.2649	9.3721
	XCQ4	8.7808	9.1499	9.2591	9.3105	
2.5	XQ4	8.6869	9.0602	9.1681	9.2192	
	XCQ4	8.7362	9.1012	9.2108	9.2632	

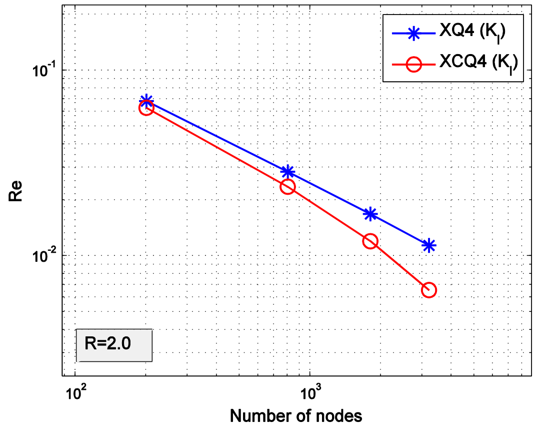

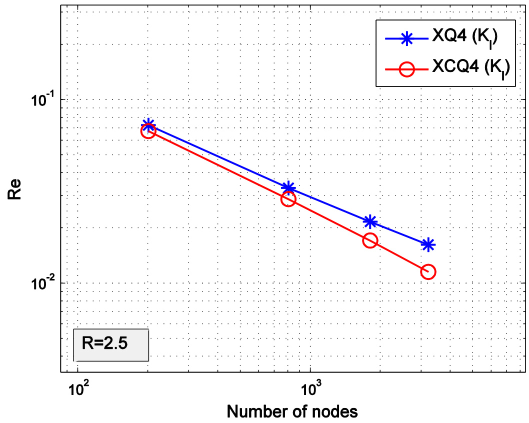

Fig. 4.7 Convergence results of mode I SIF of an edge crack under tension loading obtained by the XCQ4 and XQ4 for different R.

In order to further interpret and exhibit the performance of XCQ4 in stress distribution, the σ_x stress contour and von Mises stress contour of this tension problem with a regular mesh size of 40x80 elements are shown in Figs. 4.8 and 4.9, respectively. It is very interesting to see that the proposed XCQ4 using the CIP can achieve stresses at the crack tip smoother than the one yielded by normal XQ4.

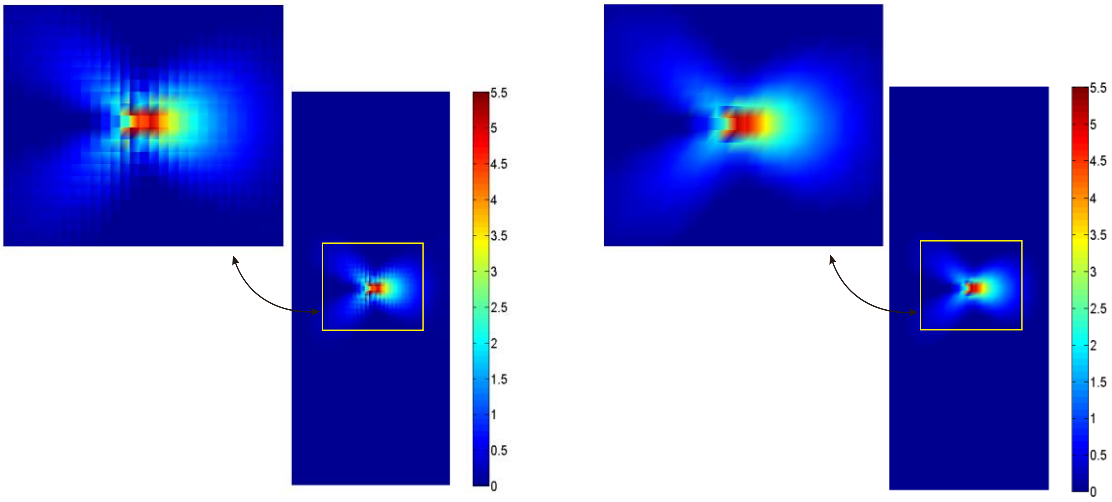

(a) (b)

Fig. 4.8 Comparison of stress distribution on σ_x between (a) XQ4 and (b) XCQ4 using a fine mesh. The normal stress at the crack tip derived from the XCQ4 is smoother than that gained by the XQ4.

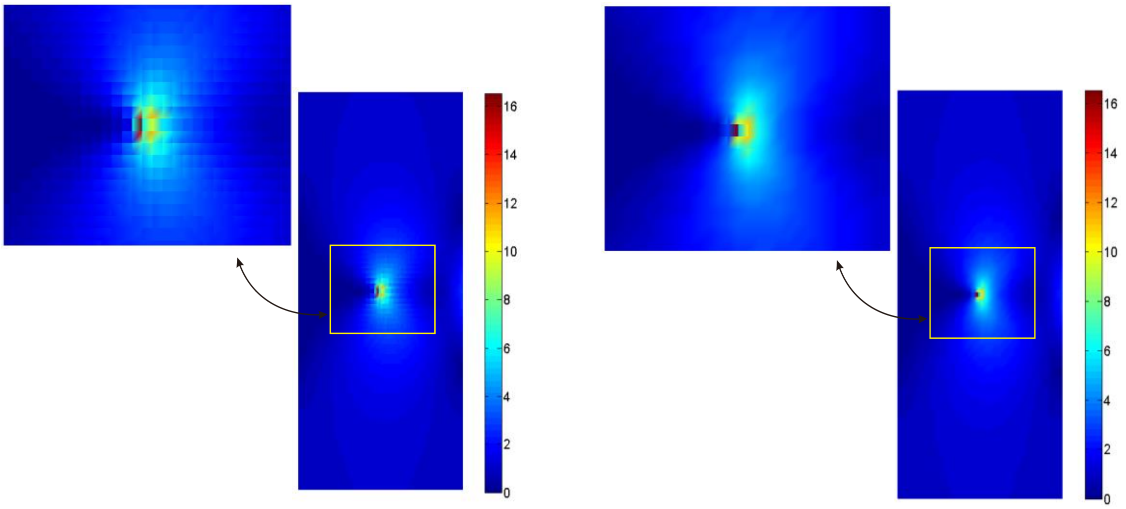

(a) (b)

Fig. 4.9 Comparison of the von Mises stress between (a) XQ4 and (b) XCQ4 using a fine mesh. The von Mises stress at the crack tip derived from the XCQ4 is smoother than that gained by the XQ4.

4.4 An Inclined Central Crack under Tension

The third numerical example deals with mixed-mode problem by considering an inclined crack in a rectangular plate under a pure tension $\sigma = 3MPa$ on both sides of plate, as shown in Fig. 4.10. The parameter θ is to define the angle with respect to the horizontal axis. The dimensionless geometric parameters are set to be $L = 2$ and $W = 1$.

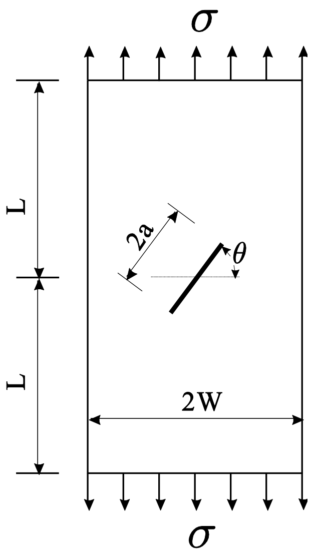

Fig. 4.10 Geometry notation of an inclined central cracked plate under tensions.

When $\theta = 0^o$, the analytical solution for mode-I SIF can be obtained by [Wu and Cai, 2014] as follows:

$$K_I = \sigma\sqrt{\pi a}\sqrt{\sec\frac{\pi a}{2W}}\left[1-0.025\left(\frac{a}{W}\right)^2+0.06\left(\frac{a}{W}\right)^4\right] \quad (4.4)$$

and the convergence in relative errors of the mode I SIF against the element size (h) is then shown in Fig. 4.11. In the results, two different crack-length-to-width ratios, $a/W = 0.2$ and $a/W = 0.6$ for instance, are considered, and the corresponding mode I SIF calculated by the XCQ4 and XQ4 for four different regular meshes of 19x39; 24x49; 29x59 and 34x69 elements are obtained. The results are very interesting, and similar to the previous examples the XCQ4 performs outstanding over the conventional XQ4.

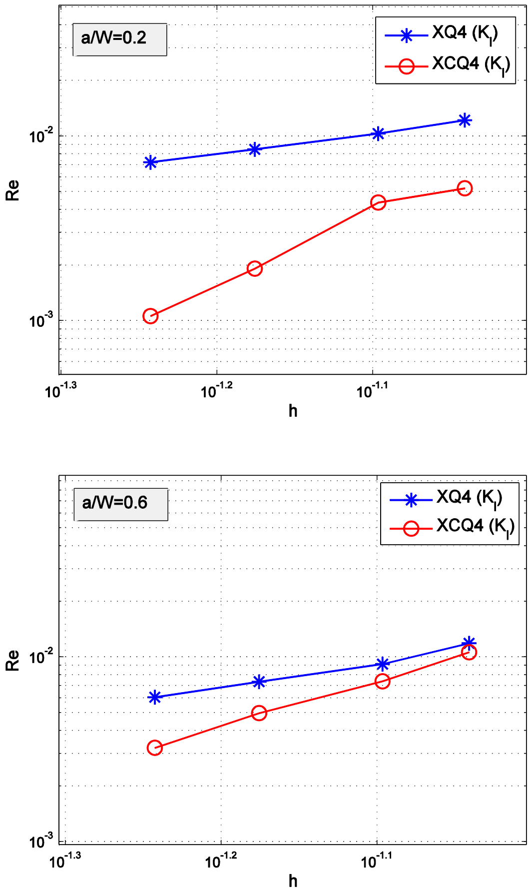

Fig. 4.11 Convergence rate of mode I of an inclined central crack plate for different crack lengths.

When the crack angle θ is set to be arbitrary within $[0^o, 90^o]$, the mixed-mode can hence be developed. A crack-length-to-width ratio of $a/W = 0.2$ and a regular mesh of 29x59 elements are taken. As previously stated in [Moës et al., 1999] that the plate dimensions are large in comparison to the crack length, the numerical solution can be compared to the solution for an infinite plate. Under such loading condition, the exact SIFs for this problem are given by

$$\begin{aligned} K_I &= \sigma\sqrt{\pi a}\cos^2(\theta) \\ K_{II} &= \sigma\sqrt{\pi a}\sin(\theta)\cos(\theta) \end{aligned} \tag{4.5}$$

The present numerical results of K_I and K_{II} computed by the XCQ4 in Fig. 4.12 reveal a good agreement with the exact solutions for the entire range of the crack angle θ.

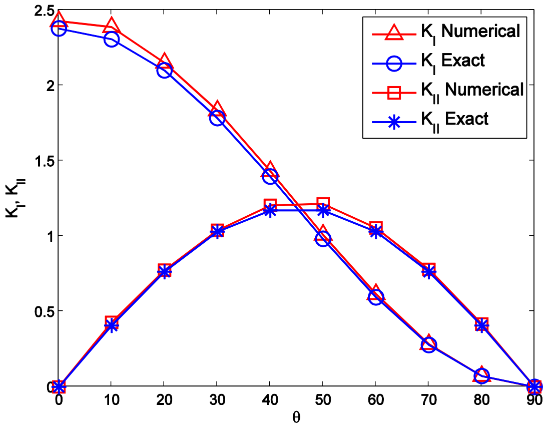

Fig. 4.12 Variation of K_I, K_{II} versus angle θ for a plate with an angled center crack $a = 0.2$ obtained by the developed XCQ4 element.

4.5 A Cruciform Specimen Containing An Inclined Center Crack

4.5.1 Basic Fracture Analysis of Mode I

To show the applicability of the developed XCQ4 method in cracks modeling of complicated configurations, the last numerical example to a cruciform specimen with an interior inclined center crack is considered as sketched in Fig. 4.13(a). The geometric parameters of the specimen are $2L = 330mm$, $2S = 200mm$, $2H = 150mm$, $2W = 100mm$ and a crack length $2a$ varying from $60mm$, $80mm$ and $100mm$. The tension $\sigma = 1$ is imposed on both sides of specimen. In addition, the total discretization of structure contains 1372 nodes and 1299 elements as displayed in Fig. 4.13(b) and the structured discretization consisting of 22x22 nodes is utilized in the region covering the crack. The dimension of the region is 110 mm × 110 mm.

The cruciform specimen has been previously studied by [Kitagawa et al., 1979] using an experimental method and [Tanaka et al., 2015] using an extended wavelet Galerkin method with a high-order B-spline basis function. However, the normalized SIFs $K_I^* = K_I/\sqrt{\pi a}$ and $K_{II}^* = K_{II}/\sqrt{\pi a}$ are employed to assess the robustness and accuracy of the XCQ4 method and the reference solution only for mode I is given by [Kitagawa et al., 1979]

$$K_I^{*,Ref} = 1.1906 + 0.0076\frac{a}{W} + 0.2051\left(\frac{a}{W}\right)^2 - 0.0042\left(\frac{a}{W}\right)^3, \qquad 0.2 \le a/W \le 1.0 \qquad (4.6)$$

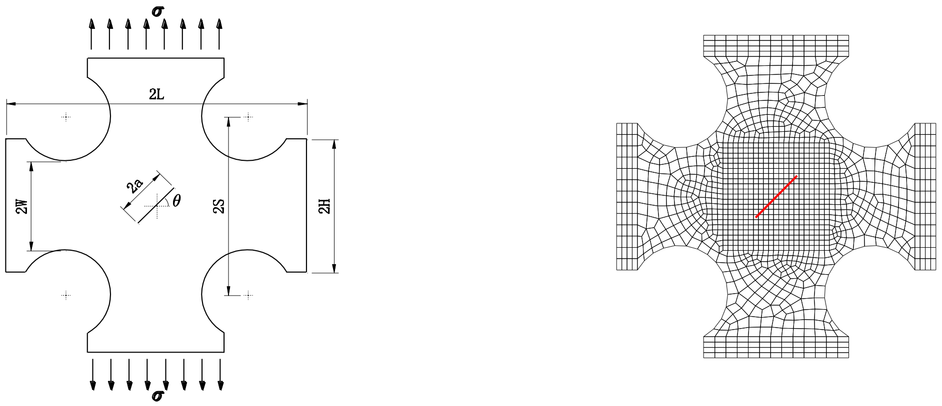

(a) (b)

Fig. 4.13 (a) Geometric notation of a cruciform specimen model and its boundary condition. (b) A typical irregular mesh for the cruciform specimen. Note that the mesh at the crack is uniform.

Subsequently the relative error between numerical and analytical normalized mode I in regard to different values of a/W = 0.6, 0.8 and 1.0, and $\theta = 0^o$ is tabulated in Table 4.5.

From the table one can find out that the XCQ4 performs better than the XQ4 through the comparison of the relative errors for each other. Regardless of the coarse mesh discretization in the region covering crack, the XCQ4 can manage the relative error below 1% as well. Moreover, the present numerical results exhibit that the mode I SIF increases with an increase of the aspect ratio of crack-length-to-width a/W, but its variation is small.

In Fig. 4.14 and Fig. 4.15 the σ_{xx} stress coutour and von Mises stress contour of cruciform specimen is provided so as to testify XCQ4 is able to generate the remarkable stress distribution among the elements having disordered aspect ratio, which indicates the more flexible applicability of present method.

To quantitatively verify the difference of stress distribution between the XCQ4 and XQ4 method, the averaged σ_{xx}, σ_{yy} and σ_{xy} values associated with 19 elements defined in Fig. 4.16 are extracted and the comparison of stress values computed by XCQ4 and XQ4 are plotted in Figs. 4.17-4.19. According to the results, it is obvious that the smoother stress distribution can be achieved by XCQ4 in comparison with the results derived from XQ4 method.

Table 4.5 Comparison of the normalized mode I SIF K_I^* for different a/W and $\theta = 0^o$ between the XCQ4 and XQ4.

a/W	XQ4	Relative error (%)	XCQ4	Relative error (%)	$K_I^{*,Ref}$
0.6	1.2490	1.5	1.2591	0.7	1.268
0.8	1.3045	1.62	1.3157	0.78	1.326
1.0	1.3749	1.72	1.3884	0.76	1.399

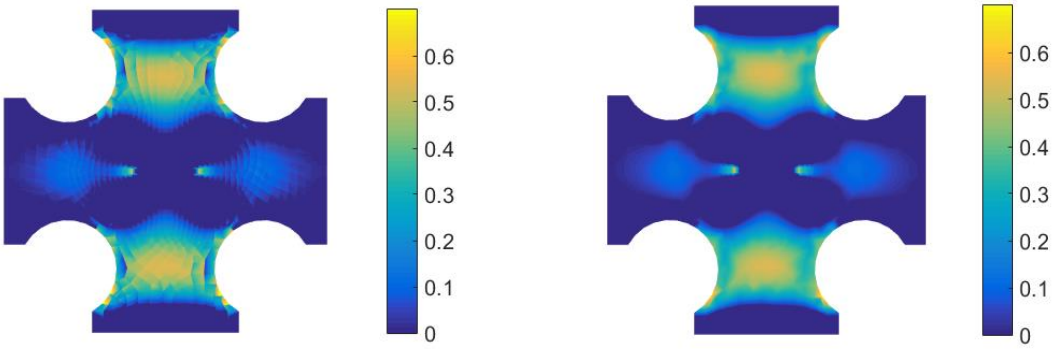

(a) (b)

Fig. 4.14 Comparison of stress distribution on σ_{xx} between (a) XQ4 and (b) XCQ4.

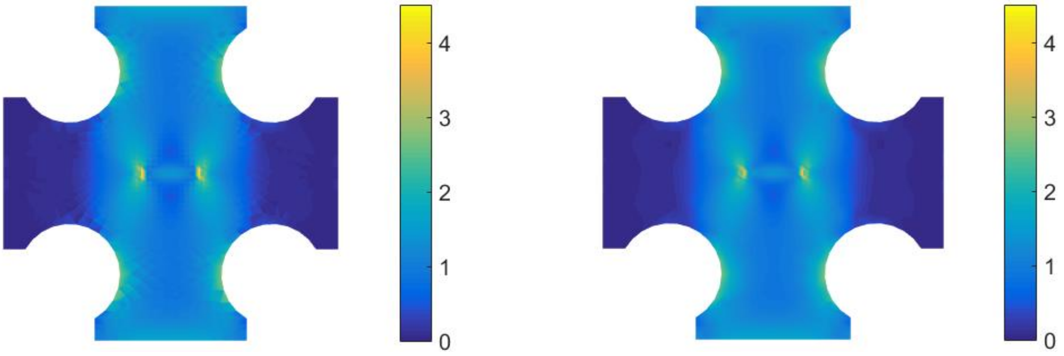

(a) (b)

Fig. 4.15 Comparison of the von Mises stress between (a) XQ4 and (b) XCQ4.

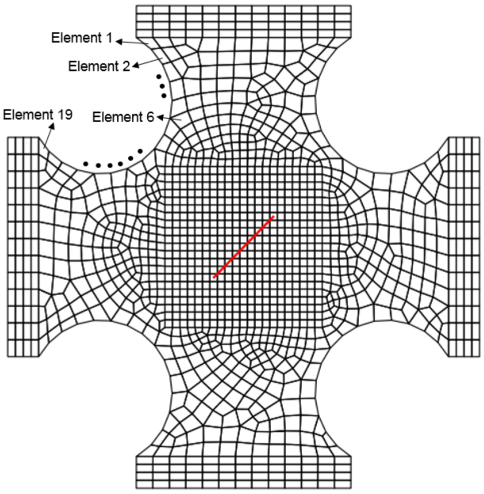

Fig. 4.16 Location of the prescribed elements for stress extraction.

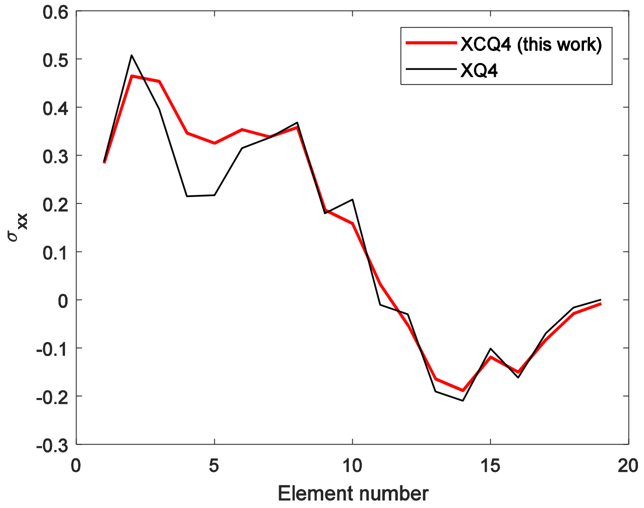

Fig. 4.17 The averaged σ_{xx} for the prescribed elements.

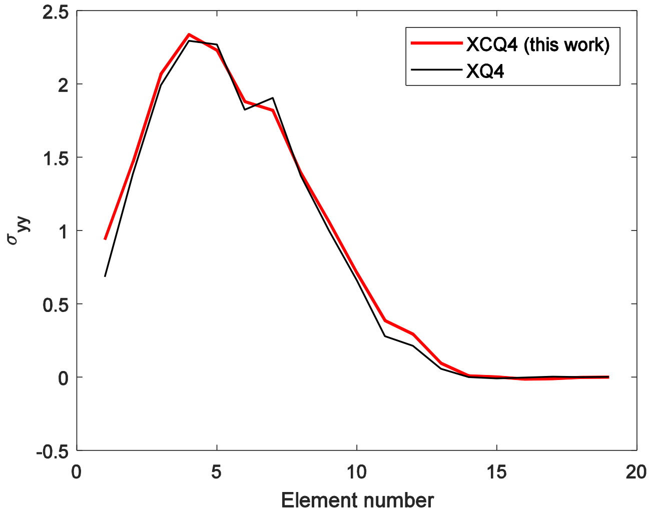

Fig. 4.18 The averaged σ_{yy} for the prescribed elements.

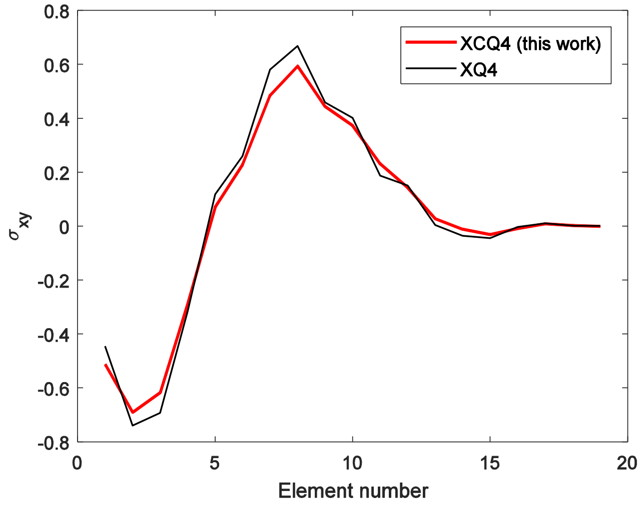

Fig. 4.19 The averaged σ_{xy} for the prescribed elements.

4.5.2 SIFs Plot for Mix-mode Fracture

Next, the mixed-mode fractures by setting the crack angle θ to be arbitrary within the range of $[0^o, 90^o]$ is estimated. A crack-length-to-width ratio of $a/W = 0.6$ is examined only. The previous results presented by [Tanaka et al., 2015] using an extended wavelet Galerkin method (XWGM) with a high-order B-spline basis function are employed for the validation purpose. Fig. 4.20 shows a very good agreement of the normalized K_I^* and K_{II}^* results calculated by the developed XCQ4, the common XQ4 and the XWGM [Tanaka et al., 2015] for the entire range of crack angle θ.

It is distinctly observed that the value of K_I^* is negative once the crack angle θ approaching to 90^o. This situation can also be seen the same in the work done by [Tanaka et al., 2015] using the XWGM, but they did not give any discussions to the arisen issue in their paper. The mode I SIF here is not like the third example levelling off to zero but breaks through the zero and reaches the negative value. Basically, there are two assumptions that may reasonably be handled to explain the insight into the physical meaningless negative SIF. One is due to the fact that no assumption of crack face contact has been made, which may require an advanced iterative solution procedure. The configuration of this example is more complicated than the third example as its boundary includes the curves, so the stress and displacement behaviors inside the specimen and especially nearby the crack tip may be different from the plate composing of straight line boundaries. As well-known that the SIFs predominantly depend on the stresses and displacements existed in the vicinity of crack as they are used for the implementation of the interaction integral.

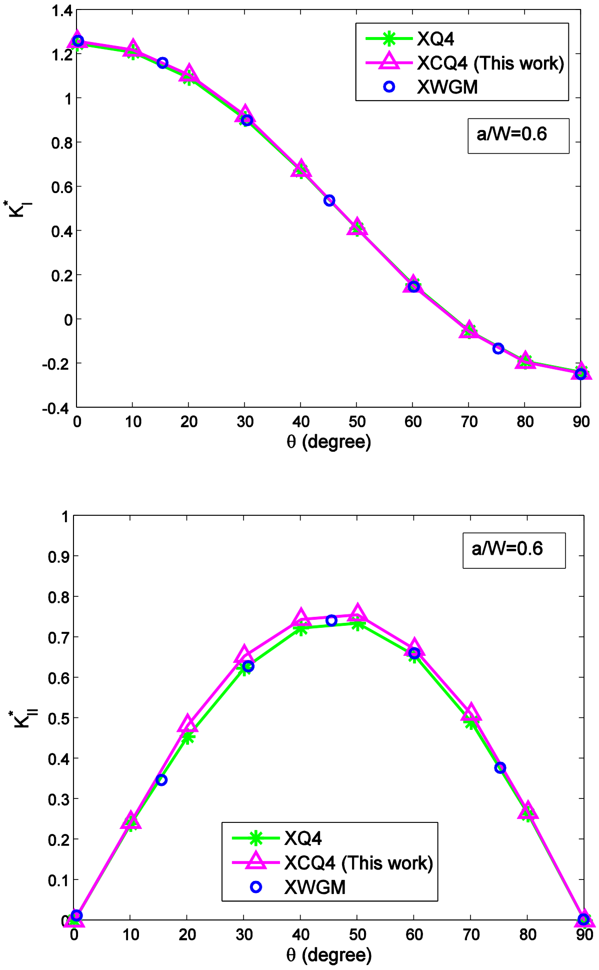

Fig. 4.20 Comparison of the normalized SIFs of the cruciform specimen containing an angled center crack among the XCQ4, XQ4 and the XWGM.

4.6 Summary

The applicability of the present element has been shown as it can yield quite good accuracy to the structures with complicated configuration. The basis function for the XCQ4 element not only provides better numerical solutions but also offers a smoother stress distribution at the crack tip, which is not trivial obtained by the standard elements. Upon the achievement during the performance of this work the implementation of the XCQ4 for crack propagation can be figured out that more accurate crack propagation path could be able to attain in terms of more precise crack propagation direction gained by stress intensity factor at crack tip. Based on the investigations it can be observed that the developed XCQ4 element performs outstanding for the SIFs involving single and mixed-mode fractures. Its extension to other engineering non-smoothed problems would be possible and potential.

CHAPTER 5

QUASI-STATIC CRACK GROWTH SIMULATION

5.1 Introduction

According to the aforementioned research achievement, the evaluation of quasi-static crack propagation in 2-dimensional solids is explored in chapter 5. For some of these problems numerical results have also been calculated with the standard extended finite element (XQ4), provided that the two approaches have the same number of degrees of freedom. In addition, two different versions of enrichment functions capturing the crack tip fields are taken into account, integrating into either the XCQ4 or XQ4. In each case, results have been computed with both settings and compared between each other. It is found that the numerical solution using the XCQ4 element has better accuracy than that found with the XQ4, and these solutions agree well with reference solutions available in literature. The underlying difference between the constitutive-interpolation basis functions and those for the traditional XQ4 is that the former approximation functions constructed by incorporating both nodal values and averaged nodal gradients obtained from linear shape function as interpolation conditions, enhancing and smoothing the stress fields and stress intensity factors.

The accuracy and performance of the developed XCQ4 in modelling crack growth are demonstrated through six representative numerical examples in 2D solids. The mesh sensitivity to the XCQ4, the crack paths, the SIFs obtained by either the new ramp enrichment functions or the standard enrichment functions, the deformed shapes, stress distribution, etc. are considered and analyzed. The computed results of all numerical examples are thus compared with reference solutions derived from experimental or other numerical methods. In what follows, six different approaches under consideration are formed as follows:

- XCQ4 (Std): Standard extended CQ4 element
- XCQ4 (Linear): Extended CQ4 element coupling linear ramp function
- XCQ4 (Cubic): Extended CQ4 element coupling cubic ramp function
- XQ4 (Std): Standard extended Q4 element
- XQ4 (Linear): Extended Q4 element coupling linear ramp function
- XQ4 (Cubic): Extended Q4 element coupling cubic ramp function

In subsection 5.2.3, the conditioning of corresponding approaches is investigated respectively. In numerical example 5.3 and 5.4, the influence of mesh density on the predicted crack path and mix-mode SIFs accuracy, and computational times of assembling global stiffness matrix using different numerical approaches is evaluated respectively. In numerical 5.5, 5.6 and 5.7, the feasibility of the XCQ4 (Std) method in complex specimen configuration containing curve boundary and unstructured discretization is evaluated. Also the smaller crack incremental sizes are taken into account in these examples. Therefore initial mesh refinement is prescribed to ensure the accuracy of the predicted crack path by XCQ4 (Std) and mesh density will not change when the crack is growing.

Similar to the preceding studies, a set of 2x2 Gaussian points for the standard elements is found to be adequate. However, higher quadrature order, 7x7 for instance, is taken for the elements surrounding the crack-tip instead. In addition Fig. 5.1 shows the numerical procedure of modelling crack growth by means of the proposed XCQ4 and XQ4 method. The numerical achievements in this chapter is cited from [Kang et al., 2017].

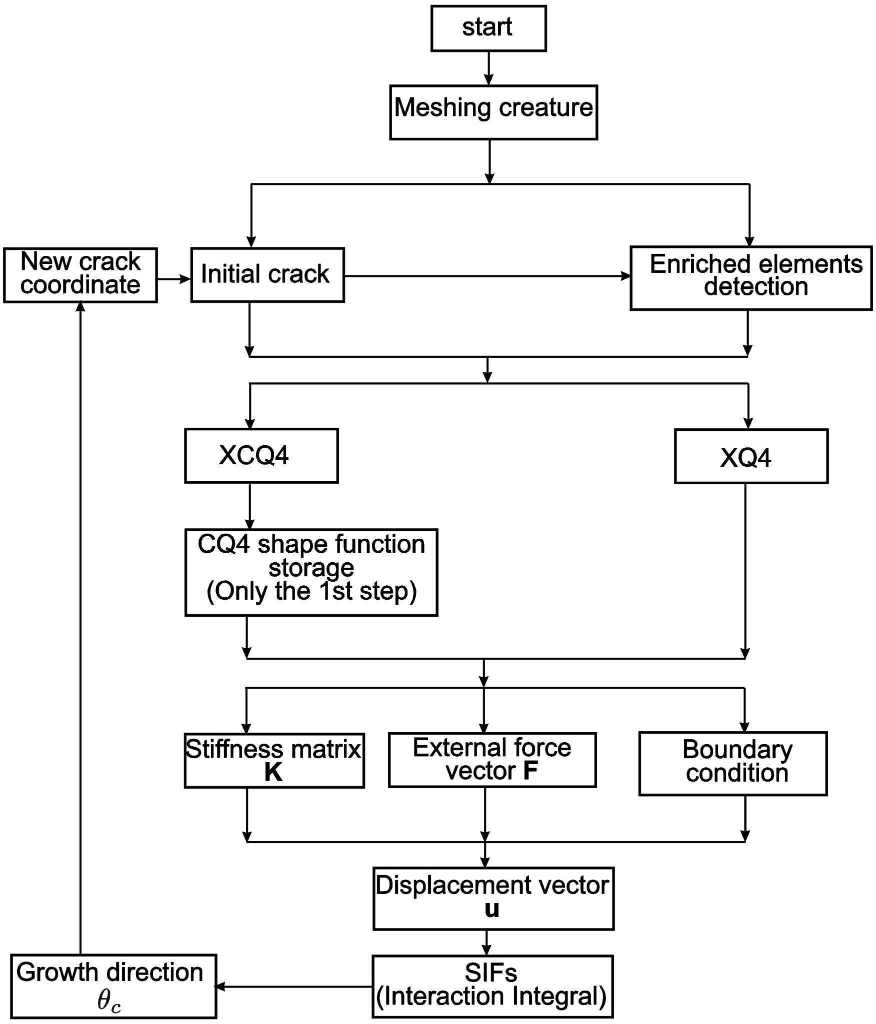

Fig. 5.1 Key steps of crack propagation modelling with proposed XCQ4 and XQ4 method.

5.2 Crack Initiation and Growth

5.2.1 Basic Formulation and Theory

In this section the detail of selected criterion used to compute the crack growth direction and the modified interaction integral procedure are introduced. Under general mixed-mode loadings, the asymptotic near-tip circumferential and shear stresses take the following expression [Belytschko et al., 1999]

$$\begin{Bmatrix}\sigma_{\theta\theta}\\ \sigma_{r\theta}\end{Bmatrix}=\frac{K_I}{\sqrt{2\pi r}}\frac{1}{4}\begin{Bmatrix}3\cos(\theta/2)+\cos(3\theta/2)\\ \sin(\theta/2)+\sin(3\theta/2)\end{Bmatrix}+\frac{K_{II}}{\sqrt{2\pi r}}\frac{1}{4}\begin{Bmatrix}-3\sin(\theta/2)-3\sin(3\theta/2)\\ \cos(\theta/2)+3\cos(3\theta/2)\end{Bmatrix} \tag{5.1}$$

In this work, the maximum circumferential stress criterion is adopted to predict the direction of crack growth θ_c by setting the shear stress $\sigma_{r\theta}$ to be zero. The expression of θ_c can be written as

$$\theta_c = 2\arctan\frac{1}{4}\left(\frac{K_I}{K_{II}}\pm\sqrt{\left(\frac{K_I}{K_{II}}\right)^2+8}\right) \tag{5.2}$$

Accordingly the stress intensity factors K_I and K_{II} in the above equation are calculated by using domain forms of interaction integral as mentioned before. In order to make the interaction integral more easily to implement a bounded weighting function $q(\mathbf{x})$ is introduced. Specifically the value of $q(\mathbf{x})$ take unity on an open set containing the crack tip and vanishes on an outer prescribed contour as sketched in Fig. 5.2(a). For a stereo observation of weighting function the three-dimensional values of $q(\mathbf{x})$ around the region containing the crack tip is portrayed in Figs. 5.2(d)-(f) in different evolving stages. Usually when the interaction integral proceeds, there are three steps for the implementation.

- The domain form of interaction integral must be determined, in other words the radius r_d of the domain embracing the crack tip should be selected in the first place.
- Based on the prescribed area where the computation of interaction integral takes place, the value of weighting function $q(\mathbf{x})$ is defined as 1 inside the domain and 0 otherwise. It can be observed that the term $\partial q/\partial x_j$ in the domain form of interaction integral implies that the interaction integral is meaningful only over the field where the value of $q(\mathbf{x})$ is not constant.

- The domain of interaction integral shall move along with the crack tip such that the interaction integral can be assessed precisely at each incremental step and the direction of crack growth can be obtained accordingly.

However when the crack tip approaches the boundary of the body, the domain of interaction integral may be failed to fully locate inside the body. In this case the evaluation of interaction integral is conducted along the contour that is not encircling the crack tip. This particular case is graphically represented in Figs. 5.2(b) and (e). Thus the summation of energy over each element pertaining to the domain of interaction integral cannot reflect the real energy field around the crack tip. Thus the crack growth direction θ_c will be determined inaccurately, which consequently leads to the less accuracy of the final output of the results. Therefore, this particular scheme is adopted to overcome this shortcoming in the implementation of interaction integral for crack propagation as illustrated in Figs. 5.2(c) and (f). Two steps for this modification are required.

- The value of weighting function $q(\mathbf{x})$ should be assigned as 1 for the nodes inside the radius r_d and 0 outside.
- Collect all the boundary nodes and let the value of weighting function $q(\mathbf{x})$ be zero for these nodes. Then the interaction integral can be computed over a contour encircling the crack tip completely.

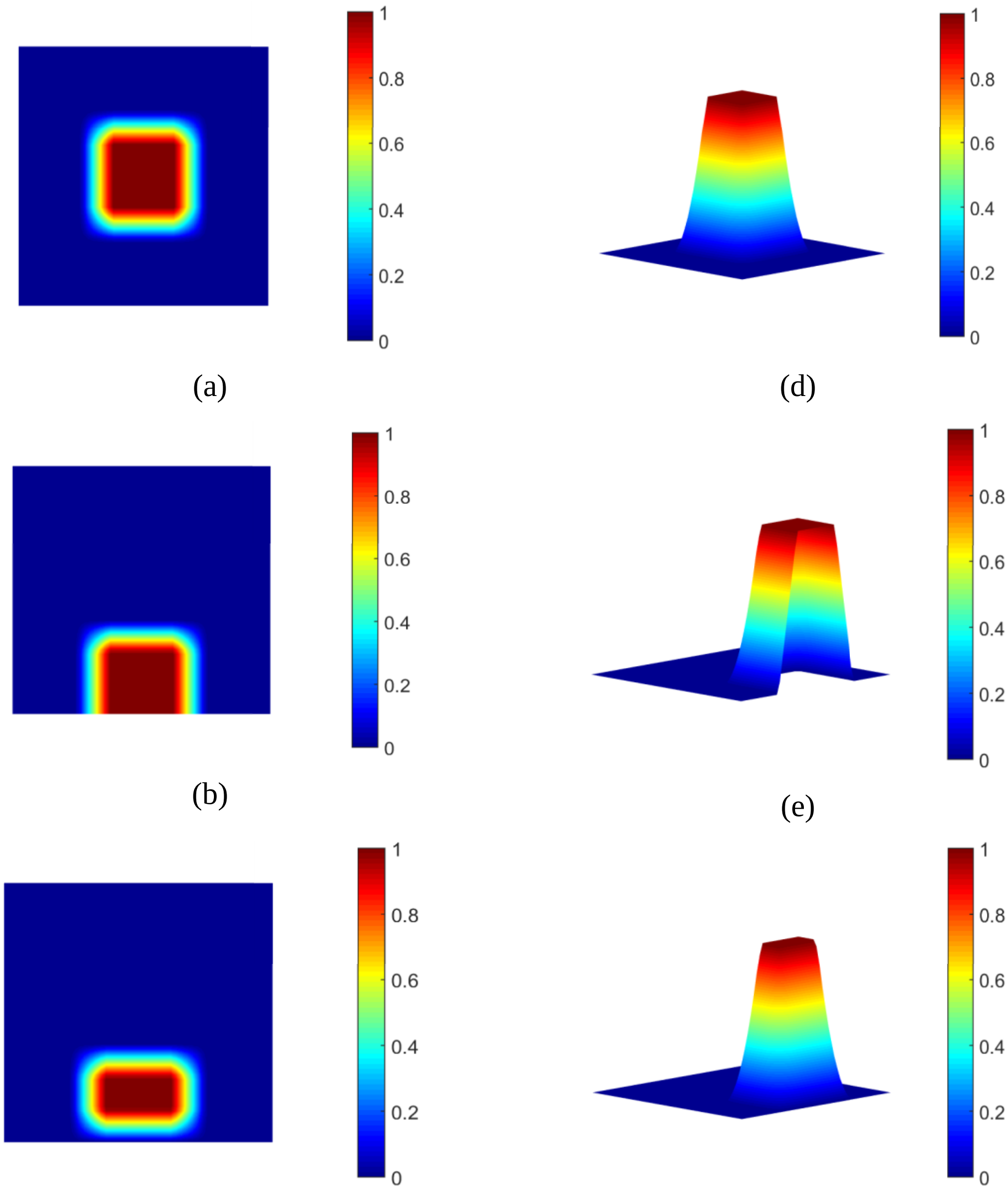

(a) (d)

(b) (e)

(c) (f)

Fig. 5.2 Values of the weighting function $q(\mathbf{x})$ regarding different crack tip position. (a) (d) Inside (initial); (b) (e) Intersection (raw); (c) (f) Intersection & Inside (modified).

It is worth to stress out that the support domain for the element considered in J-domain in terms of the XCQ4 is larger than that of the XQ4. The reason is caused by the larger span formed by neighboring elements of the CIP framework.

5.2.2 Two Pragmatic Algorithms for Crack Growth

In the crack propagation problem, several special situations should be considered in an appropriate manner. For instance, two cracks propagate and encounter with each other, finally join and growth together with a new generated junction. Also if a crack grows to a boundary, the implementation of the final step should be determined to terminate the iteration. Here, two pragmatic algorithms are introduced as boundary algorithm and coalescence detection algorithm proposed by [Budyn et al., 2004].

Boundary algorithm indicates that extend the current position of crack tip point by a prescribed incremental length in the direction normal to the nearest boundary, if the latter point is outside the body, the final place of the crack tip is at the intersection point of the free boundary with the virtual extension of the crack. Then, the segment between these two points should be regarded as final part of crack path.

Coalescence detection algorithm is similar to [Carpinteri et al., 1990], which demonstrates that if crack A approaches crack B, find the closest crack segment of crack B from the current tip of crack A, when the distance between the growing crack A tip and the middle of the closest segment of crack B is less than the incremental length, the cracks are joined. The relevant mathematical definition of junction enrichment function is elaborated in Section 5.7.

5.2.3 Conditioning Analysis

In Fig. 5.3, the condition number of proposed methods are illustrated in the case consisting of LxL square with an edge crack. The initial length of crack is set to be $a = 0.5$ and the dimension of square is $L = 1$. The material parameters are taken as $E = 100$ and $\upsilon = 0$. Through observing the slope rate in Fig. 5.3(a), it is evident that XCQ4 (Std) presents better performance than XQ4 (Std) method with the increasing of the discretization density. In the case of ramp functions replacing branch functions to enrich crack tip nodes, results of Fig. 5.3(b) and Fig. 5.3(c) indicate that the condition number influenced by ramp function is lower than the standard branch functions in proposed methods, which means the problem solved by ramp functions is relatively well-conditioned.

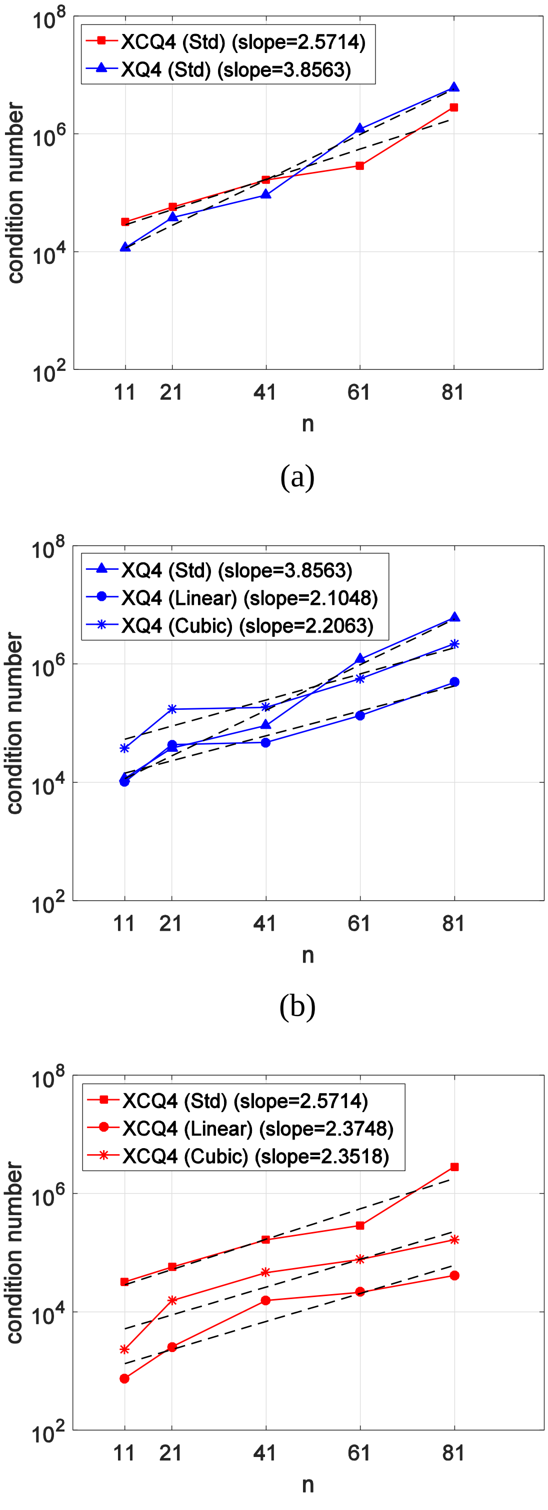

(a)

(b)

(c)

Fig. 5.3 Condition numbers of the system matrices assembled by six different approaches versus the number of elements in each direction.

5.3 A Single Edge Crack Plate Under Mixed Mode Loading

Let us begin with a single notched plate containing an initial crack $a = 3.5$ as depicted in Fig. 5.4. The plain strain condition is assumed and the plate is determined by the following geometric parameters $W = 7$ and $L = 16$. The Young's modulus $E = 30\text{x}10^6 Pa$ and the Poisson's ratio $\nu = 0.25$ are chosen. The specimen is subjected to a uniformed shear stress $\tau = 1$ along the top edge and fixed at the bottom. This case was solved in [Phongthanapanich et al., 2004] using the adaptive finite element method with Delaunay triangulation as mesh generator and the relevant numerical results are considered as the reference to demonstrate the robustness of the proposed method. The mesh has 3471 regular elements. In this case the crack increment is $\Delta a = 0.4$ and the problem is solved in 10 steps totally.

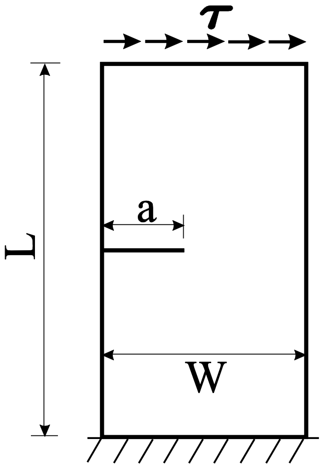

Fig. 5.4 Geometry of the edge crack plate problem.

5.3.1 The Effect of Element Size on Predicted Crack Trajectory

The influence of mesh density on the predicted crack path is investigated in this numerical example. Three regular sizes of mesh are used such as 19x49, 29x69 and 39x89. The comparison of predicted crack growth trajectories computed by the developed XCQ4 (Std) under three mesh sets is given in Fig. 5.5(a) and it can be found that the three curves generally agree with each other very well. Nonetheless through observing the latter part of the crack path in the close-up of results, the path produced by coarse mesh i.e. 19x49 has a slight deviation as compared with other two medium i.e. 29x69 and fine i.e. 39x89 mesh. This observation indicates that the mesh density has effect on the accuracy of modelling the crack evolution and an appropriate mesh density is imperative to obtain the desirable crack evolution path by XCQ4 (Std).

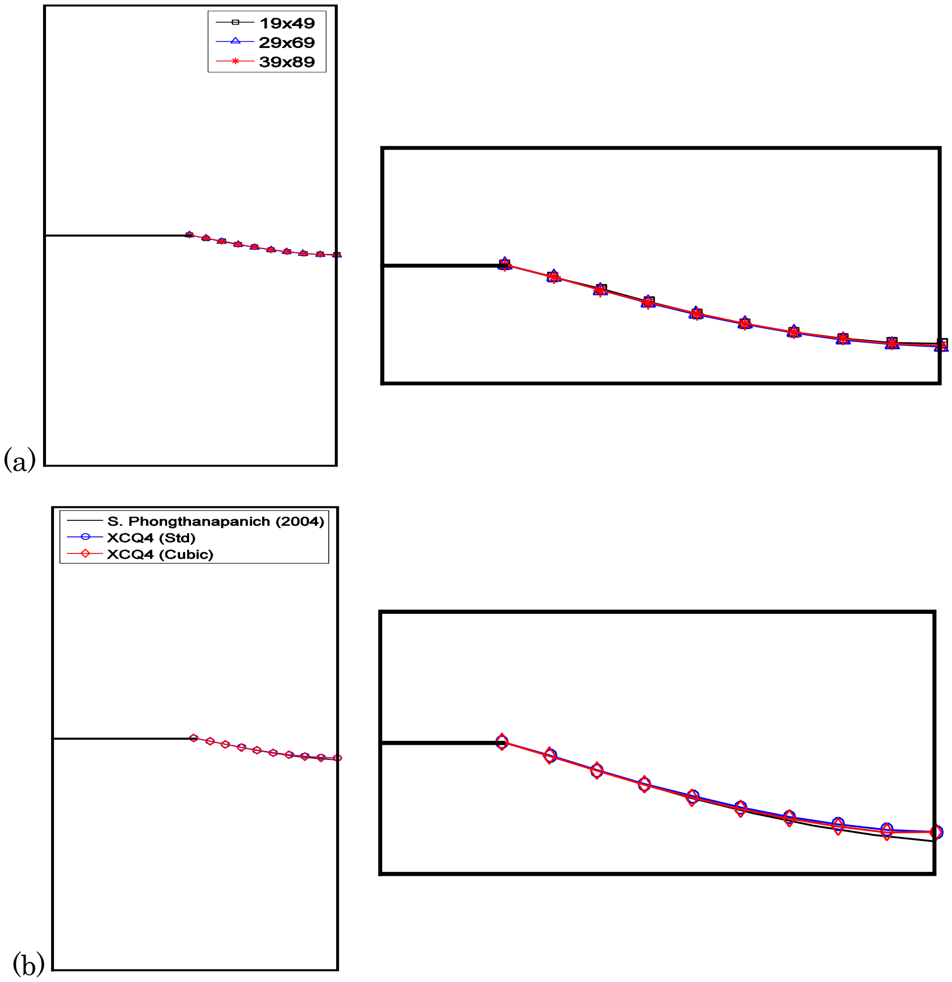

Fig. 5.5 Predicted crack paths by XCQ4 (Std) under various mesh densities (a); Comparison of XCQ4 (Std), XCQ4 (Cubic) and reference solution (b).

By considering the mesh of 39x89, Fig. 5.5(b) shows the predicted crack trajectories of the XCQ4 (Std) and XCQ4 (Cubic) method compared with solution reported by

[Phongthanapanich et al., 2004]. Based on the observation about close-up of results it is obvious that the crack growth paths obtained by XCQ4 (Std) and XCQ4 (Cubic) are close to the reference solution. Still it can be perceived that the crack path of XCQ4 (Cubic) turns above slightly as compared with that of XCQ4 (Std) when the crack approaches the plate edge. Further all specific crack tip coordinates yielded by different approaches are shown in Table 5.1. In this case, it can be recognized that the linear and cubic ramp functions are valid to take instead of the classical fourfold function to enrich the crack tip element and worthy to further develop.

Table 5.1 Comparison of the tip position for an edge-cracked plate under a shear loading obtained by the proposed numerical approaches.

Means	Tip position									
	2nd		4th		6th		8th		10th	
	x	y	x	y	X	y	x	y	x	y
XCQ4 (Std)	3.50	0.00	4.27	-0.21	5.05	-0.41	5.83	-0.57	6.62	-0.67
XCQ4 (Linear)	3.50	0.00	4.27	-0.22	5.04	-0.42	5.83	-0.58	6.62	-0.69
XCQ4 (Cubic)	3.50	0.00	4.27	-0.22	5.04	-0.43	5.83	-0.58	6.62	-0.69
XQ4 (Std)	3.50	0.00	4.27	-0.21	5.05	-0.41	5.83	-0.56	6.63	-0.66
XQ4 (Linear)	3.50	0.00	4.27	-0.21	5.05	-0.41	5.83	-0.57	6.62	-0.68
XQ4 (Cubic)	3.50	0.00	4.27	-0.22	5.04	-0.42	5.83	-0.58	6.62	-0.69

For a better digestion, the comparison of the mixed mode SIFs at the 1st step of crack growth is tabulated in Table 5.2. The same case of shear loading condition is solved by [Belytschko et al., 1999] and the exact solution is defined as $K_I = 34.0$ and $K_{II} = 4.55$ respectively. In Table 5.2 the values in the parenthesis are the normalized values of the numerical results. As stated in previous section, the XCQ4 method provides a higher accuracy over the SIFs than the traditional XQ4 method as well as the other coupled cases.

Table 5.2 Comparison of the SIFs for an edge-cracked plate under a shear loading obtained by the proposed numerical approaches.

Method	SIFs		Mesh
	K_I	K_{II}	
XCQ4 (Std)	33.8396 (0.9953)	4.5614 (1.0025)	39x89 elements
XCQ4 (Linear)	32.1892 (0.9467)	4.4841 (0.9855)	
XCQ4 (Cubic)	31.0459 (0.9131)	4.4466 (0.9773)	
XQ4 (Std)	33.6722 (0.9904)	4.4820 (0.9851)	
XQ4 (Linear)	32.3259 (0.9508)	4.4828 (0.9852)	
XQ4 (Cubic)	31.1956 (0.9175)	4.4480 (0.9776)	

5.3.2 Comparison of Stress Distribution by XCQ4 and XQ4

Here it is necessarily emphasized that the smooth nodal stress without post processing as an important feature of XCQ4 (Std) should be displayed. In Fig. 5.6 the deformed shape of the specimen at different steps is sketched respectively. In addition the normal stress σ_{xx} contour obtained by XCQ4 (Std) and XQ4 (Std) method are shown correspondingly. It can be found that the XCQ4 (Std) is endowed with an ability of providing better crack tip stress field.

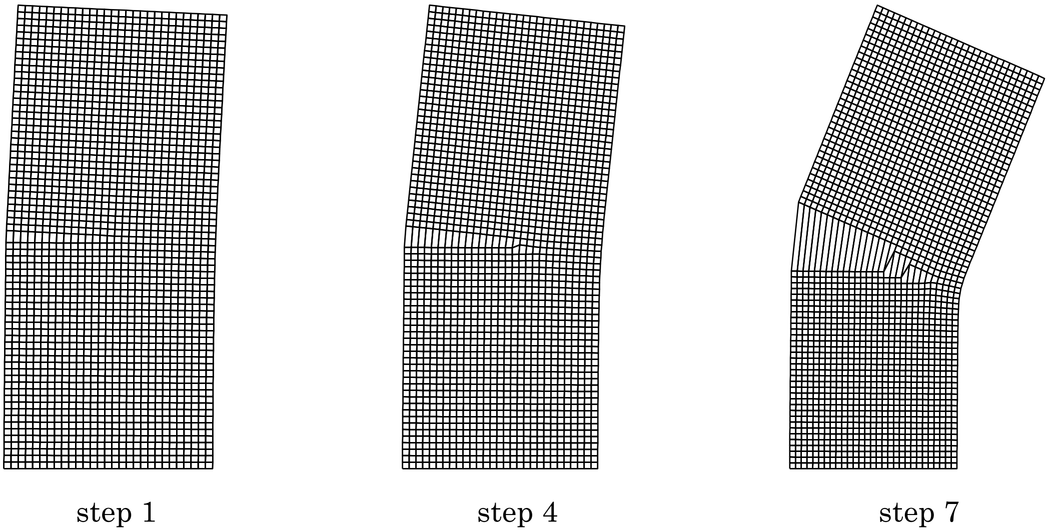

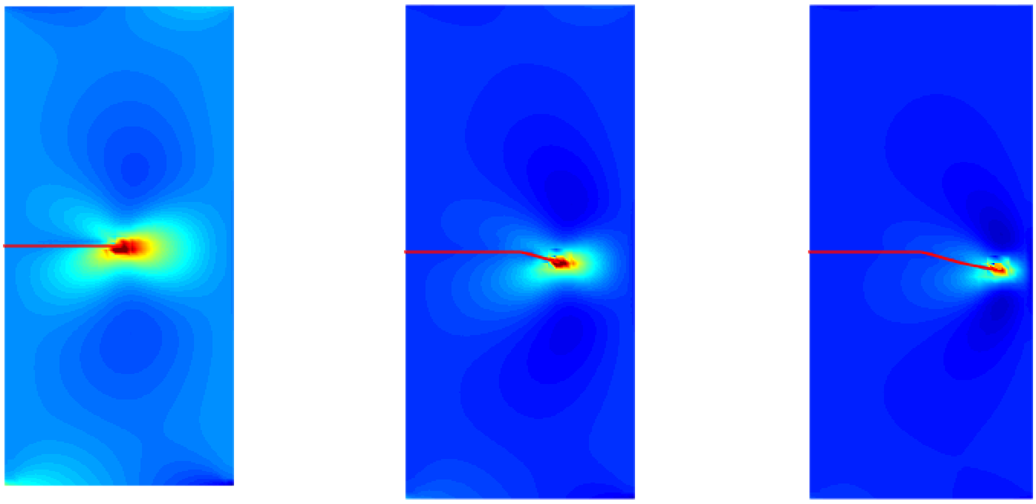

step 1_XCQ4 (Std) step 4_XCQ4 (Std) step 7_XCQ4 (Std)

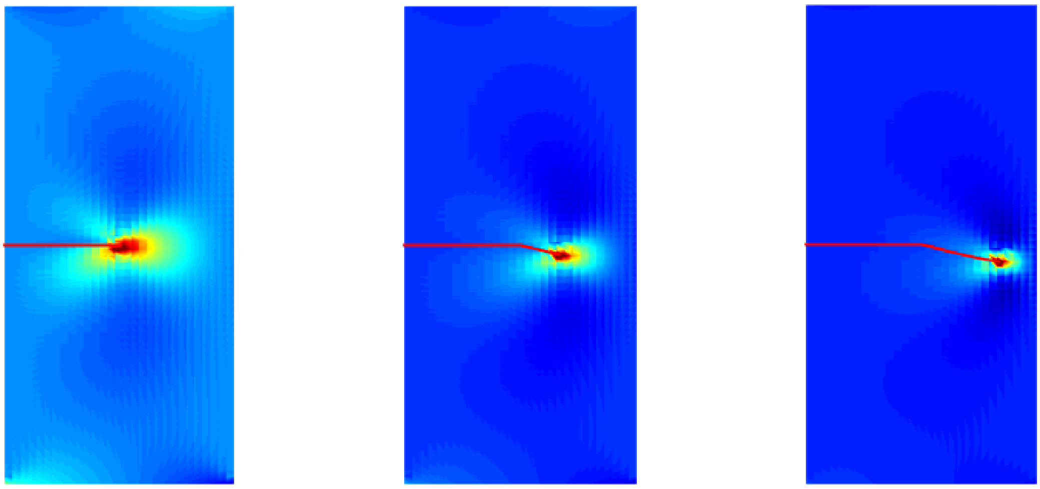

step 1_XQ4 (Std) step 4_XQ4 (Std) step 7_XQ4 (Std)

Fig. 5.6 Deformed shapes and stress σ_{xx} contours of the specimen at different growth steps.

5.4 An Edge Crack under Partial Compressive Load

A cracked rectangular plate is considered to validate the accuracy of XCQ4 and ramp function. The plane strain conditions are assumed and the geometry of specimen is schematically depicted in Fig. 5.7. A uniform compressive load $\sigma = 1$ is applied to its upper edge over a length of 4. The displacements along the y-axis are fixed at the bottom edge, meanwhile the displacements along x-axis are fixed at the right edge. The parameters of a prescribed crack are taken as $a = 5, b = 15.6$. The specimen is discretized using the regular mesh 45x68 elements. The numerical simulation is conducted by setting the incremental crack size to be $\Delta a = 0.4$ at each step. In addition the total number of 9 steps are performed.

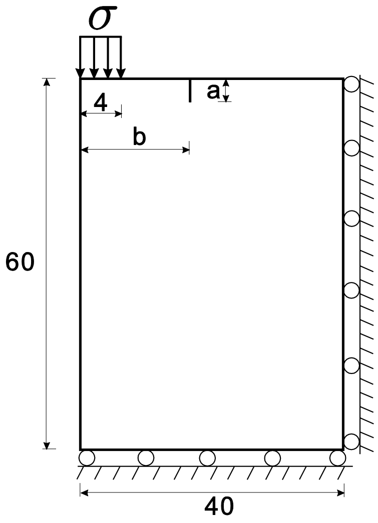

Fig. 5.7 Configuration of the plate with an edge crack.

5.4.1 Assessment of Mesh Density on Predicted Crack Path

In this example the effect of mesh density is studied and the predicted crack evolution paths yielded by XCQ4 (Std) under three sizes of mesh discretization, i.e. 21x32, 33x50 and 45x68, are plotted in Fig. 5.8(a). It is evident that the curves produced by fine (i.e. 45x68) and medium (i.e. 33x50) mesh closely resemble each other while the curve of coarse mesh (i.e. 21x32) has an apparent difference with two others. So an appropriate mesh size is desirable for crack growth simulation by XCQ4 (Std). In Fig. 5.8(b), the comparison of numerical results computed by XCQ4 (Std), XCQ4 (Cubic) with reference solution [Tabbara et al., 1998] using the element-free Galerkin method is displayed under the mesh of 45x68. The results reveal that the path predicted by XCQ4 (Std) is approaching closely to the reference solution compared with that of XCQ4 (Cubic). Furthermore the parallel stage of XCQ4 (Cubic) in the crack trajectory comes earlier than the results of XCQ4 (Std) and reference solution reported in [Tabbara et al., 1998]. In addition the computed results are summarized by means of providing the specific crack tip coordinates at each incremental step in Table 5.3.

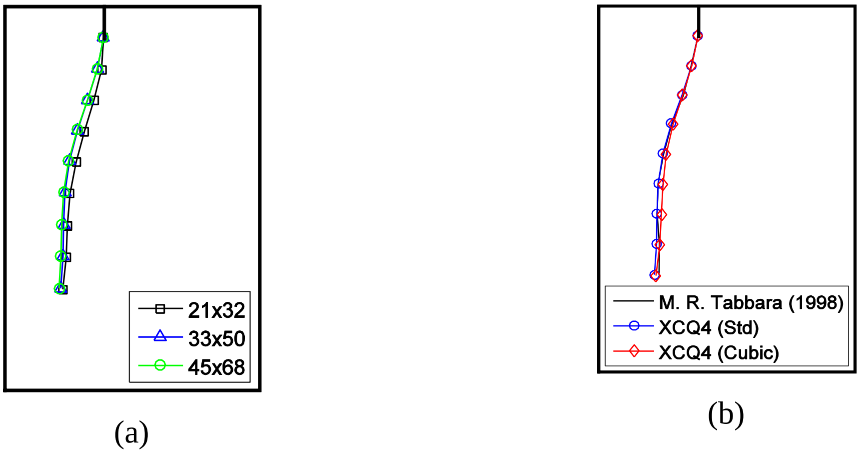

(a) (b)

Fig. 5.8 Comparison of the predicted crack paths for the plate with an edge crack in three cases.

Table 5.3 Crack tip coordinate at each step of the proposed numerical mechanisms.

Means	Tip position									
	2nd		4th		6th		8th		10th	
	x	y	x	y	x	y	x	y	x	y
XCQ4 (Std)	15.60	55.00	13.10	45.33	10.15	35.78	9.18	25.84	8.80	15.86
XCQ4 (Linear)	15.60	55.00	13.14	45.32	10.38	35.72	9.41	25.77	8.93	15.79
XCQ4 (Cubic)	15.60	55.00	13.21	45.30	10.64	35.65	9.89	25.68	9.05	15.72
XQ4 (Std)	15.60	55.00	13.13	45.32	10.23	35.76	9.21	25.82	8.79	15.83
XQ4 (Linear)	15.60	55.00	13.15	45.32	10.39	35.71	9.44	25.76	8.95	15.78
XQ4 (Cubic)	15.60	55.00	13.22	45.30	10.65	35.64	9.87	25.68	9.07	15.72
Tabbara et al., (1998)	15.60	55.00	13.32	45.27	10.27	35.76	9.23	25.84	9.53	15.85

5.4.2 Evaluation of Computational Time Cost

The computational time consumed in assembling the global stiffness matrix at the first step of crack growth is calculated and tabulated in Table 5.4. In reality, during the numerical execution of the XCQ4 the bandwidth of global stiffness matrix becomes wider than the stiffness matrix of XQ4, which causes much more time to assemble and distribute the stiffness matrix. Therefore the amount of stiffness matrix computations is almost 2.5 times as the time consumption of XQ4. It should be remarked that if the stress field around crack tip yielded by XQ4 method wishes the same smoother stress distribution, an extra post-processing computational time is indispensable. In other words, the difference of computational time between XCQ4 and XQ4 should be reduced if consider the extra post-processing computational time.

Table 5.4 Comparison of computational times for different prescribed numerical approaches.

Methods	Time (s)	Methods	Time (s)
XCQ4 (Std)	27.8510	XQ4 (Std)	11.3251
XCQ4 (Linear)	27.4788	XQ4 (Linear)	11.1722
XCQ4 (Cubic)	27.5165	XQ4 (Cubic)	11.0551

Due to the reduction in degrees of freedom at each support node in crack tip element, the computational time consumed by the scheme using ramp function as crack tip enrichment function is less than that cost by asymptotic branch functions. Despite the time consumption of different enrichment techniques are almost the same, the value of the ramp function in reducing the total computational time cannot be neglected. If the geometrical enrichment involving distance from the query node to the crack tip is chosen as crack tip enriched mechanism, there will be more than four crack tip enriched nodes, and the time consumption discrepancy should be apparent. On the other hand, in this work, computational time of assembling the global stiffness matrix is only calculated irrespective of the contribution of ramp function in post-processing and other stages.

In order to reduce the total computational time when using the XCQ4 (Std) for modeling crack evolution, a stage to store the CQ4 shape function at the 1st step of crack growth is considered. Then the CQ4 shape function will be extracted at the remaining steps when the one is required. This measure alleviates the circulatory computational time for calculating CQ4 shape function at each step.

Although the capability of capturing the discontinuity in the fracture domain is inherent in the combination of ramp function along with Heaviside function and the accuracy of SIFs is acceptable compared with analytical solution, the precision of final solution is not considered to be loosed. Then, only XCQ4 (Std) and XQ4 (Std) for modelling the crack growth path are considered in the following examples.

5.4.3 Stress Distribution at Different Time Step

As shown in Fig. 5.9 the deformed shape of the specimen at three different evolving steps is given. The predicted crack path reflects that the crack tends to propagate towards the left edge in the earlier stage and the crack trajectory is nearly parallel to the left side of surface in the medium-term stage, which is similar with the physical analysis of this case in [Tabbara et al., 1998]. The stress fields produced by the XCQ4 (Std) and XQ4 (Std) are presented in Fig. 5.9 in the same manner. The smoother stress distribution caused by XCQ4 (Std) can be found in the entire domain especially around the crack tip by contrast with the one of XQ4 (Std).

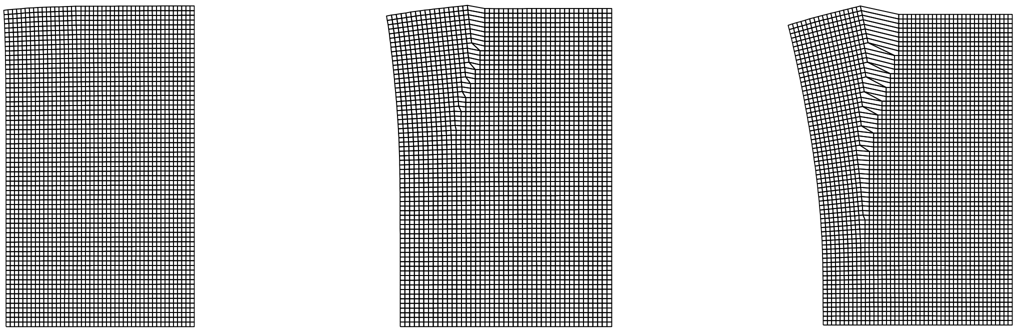

step1 step 5 step 9

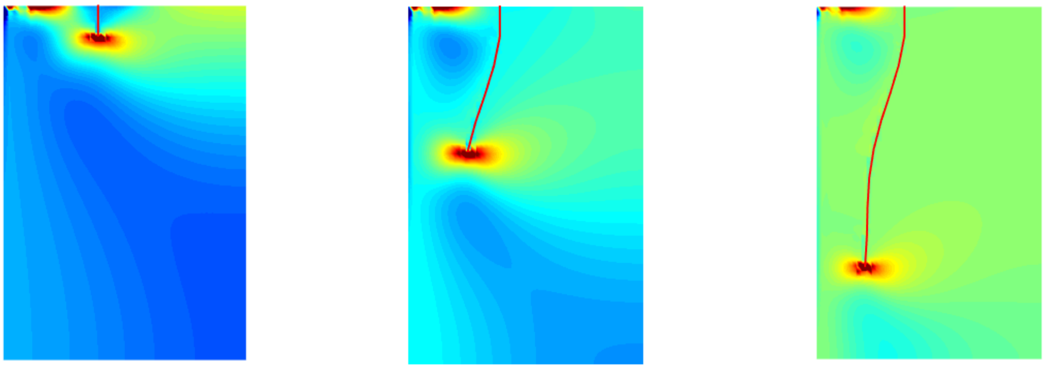

step1_XCQ4 (Std) step 5_XCQ4 (Std) step 9_XCQ4 (Std)

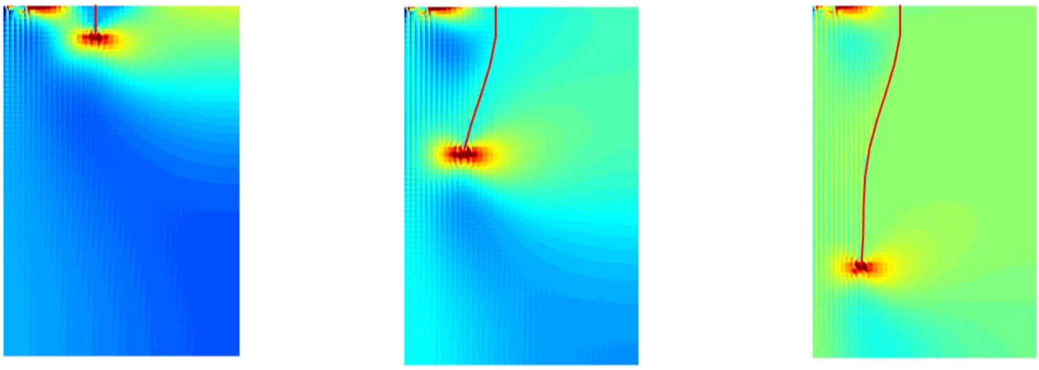

Step 1_XQ4 (Std) step 5_XQ4 (Std) step 9_XQ4 (Std)

Fig. 5.9 Deformed shapes and stress σ_{xx} contours of edge cracked plate under partial compressive loading at different steps.

5.5 Cracked Beam with Hole

5.5.1 Specimen with One hole

The following example considers a single notched beam with a hole. The geometrical parameters of the tested specimen are particularly depicted in Fig. 5.10(a). The concentrate loading $P = 100$ is imposed on the two points of the top edge and the constraint is placed on the bottom of specimen. The initial crack length is determined as $a = 2.5$ and plane strain conditions are considered. The discretization of the domain is adopted as 1977 irregular elements as shown in Fig. 5.10(b) and the incremental crack size is set to be $\Delta a = 0.8$ with total steps of 20. It is important to explain that the mesh is not necessary to be remeshed during the evolution of the crack by XCQ4 method, which is difficult to be implemented within the

FEM framework. To gain a higher accuracy of the solution, a fine mesh around the hole is adopted, while the coarse mesh far away from the hole and crack is decided. And only the XCQ4 (Std) and XQ4 (Std) are considered for modelling the crack evolution behavior. The same example has been solved numerically and experimentally by [Miranda et al., 2002, 2003]. The corresponding results are taken as the reference to validate the robustness of the proposed XCQ4 method.

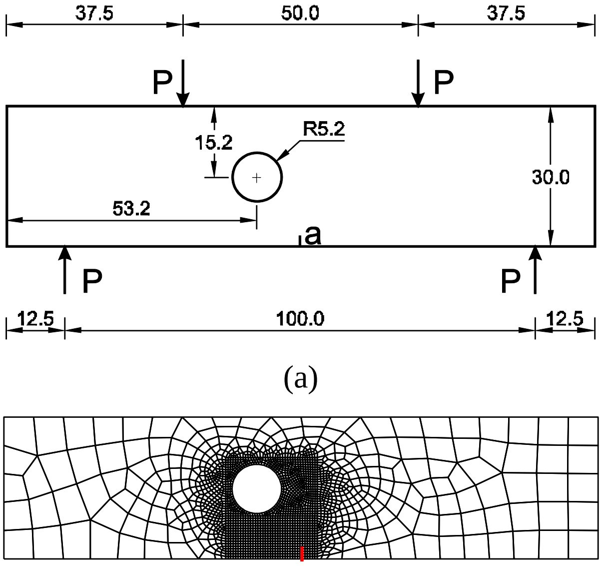

(a)

(b)

Fig. 5.10 (a) Cracked beam with a center hole; (b) Irregular discretization of the specimen.

The crack growth paths obtained by the developed XCQ4 (Std), XQ4 (Std) and the experimental solution are visualized in Fig. 5.11(a). The results point out that the predicted crack paths are consistent with the reference published in [Miranda et al., 2003] and the experimental crack path of this case reported in [Miranda et al., 2003] is exhibited in Fig. 5.11(b). The close-up of the predicted crack paths is cut out from the entire domain and shown in the Fig. 5.11(c). It can be observed that the crack propagates with a small slop in initial period when the crack tip is relatively far away from the middle hole. With the crack proceeding the orientation of the crack growth changes with a large angle and damage with the hole finally.

And the stress σ_{xx} contours of this cracked plate with an irregular mesh are shown in Fig. 5.12.

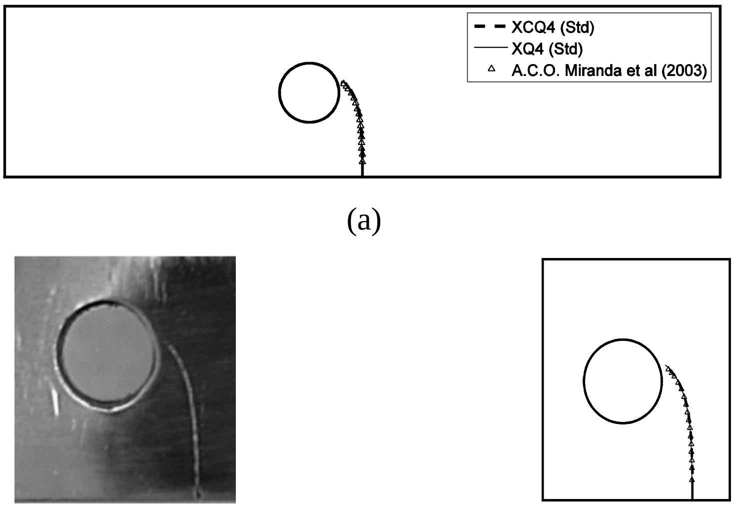

(a)

(b)

(c)

Fig. 5.11 The predicted crack path for the cracked plate with a center hole. (a) Comparison of XCQ4 (Std), XQ4 (Std) and [Miranda et al., 2003]; (b) The close-up of predicted crack path around the hole. (c) The actual crack path obtained by [Miranda et al., 2003].

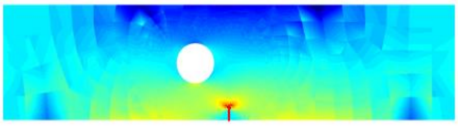

Step 2_XQ4 (Std)

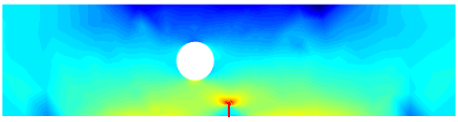

Step 2_XCQ4 (Std)

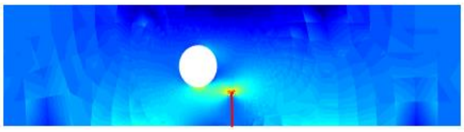

step 8_XQ4 (Std)

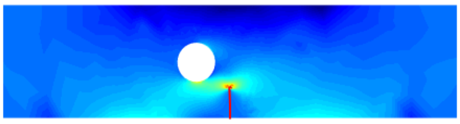

step 8_XCQ4 (Std)

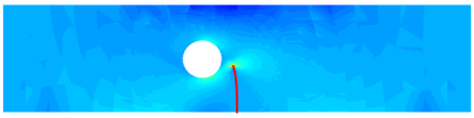

step 14_XQ4 (Std)

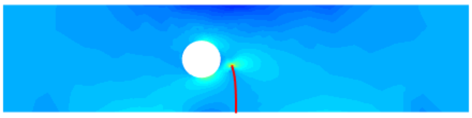

step 14_XCQ4 (Std)

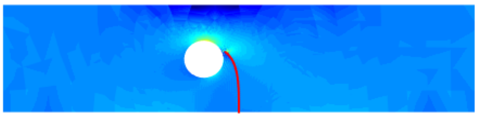

step 20_XQ4 (Std)

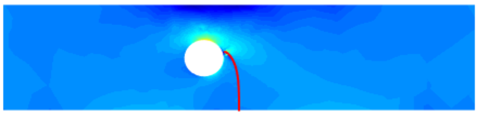

step 20_XCQ4 (Std)

Fig. 5.12 Comparison of the stress σ_{xx} contours at separate steps.

5.5.2 Specimen with Three Holes

A single edge cracked beam with three holes under mixed mode loading is selected to assess the accuracy of the proposed XCQ4 method as shown in Fig. 5.13(a). The three point bending beam is supported in two points of under edge and subjected to a concentrate loading at the mid-span of the upper edge and the plane strain conditions are assumed. This problem of simulating the crack growth trajectory is widely solved as numerical benchmark [Phongthanapanich et al., 2004; Bittencourt et al., 1996]. In this work, the same setting of initial crack a and b, which is taken as $case\ I{:}\ a = 1.5, b = 5.0$; $case\ II{:}\ a = 1.0, b = 4.0$, is given in Table 5.5. The domain discretization is set to be 3927 irregular elements as shown in Fig. 5.13(b). For the sake of acquiring more accurate crack path the density of the mesh is much finer over the region surrounding the crack and three holes than the domain far away from the crack path. Both cases are computed under the same mesh condition. It should be mentioned that the different crack incremental size has influence on the crack growth trajectory as stated in [Ventura et al., 2002]. In this work the crack incremental length is specified as described in Table 5.5.

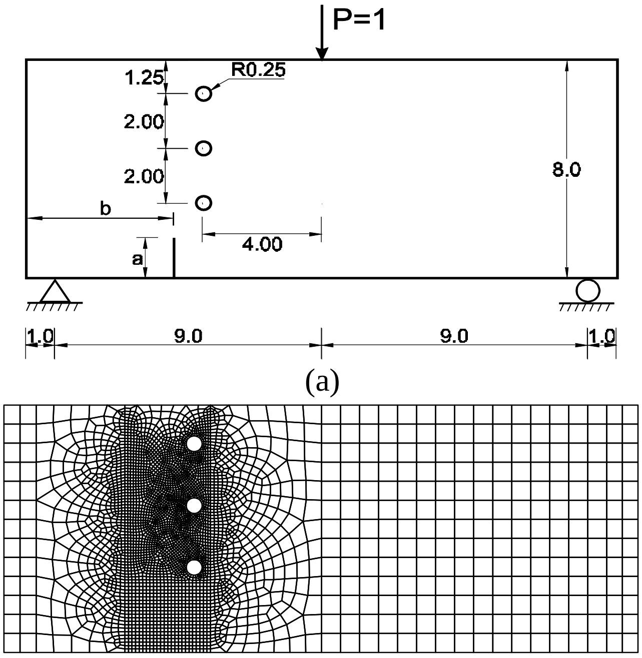

(a)

(b)

Fig. 5.13 (a) Geometry of the cracked specimen with three holes; (b) Discretization of the structure.

Table 5.5 Test cases for the cracked beam with three holes.

	a	b	Crack increment	Total steps
$case\ I$	1.5	5.0	0.12	30
$case\ II$	1.0	4.0	0.15	28

The predicted crack paths of two cases are illustrated in Fig. 5.14(a). In $case\ I$, the crack initiates towards the lower hole initially. When approaching the bottom hole the crack alters the orientation and proceeds toward the middle hole, which generates a groove in the vicinity of bottom hole as shown in Fig. 5.14(b) of close-up for $case\ I$. In $case\ II$ the crack evolution marches forward to the middle hole unhesitatingly as shown in Fig. 5.14(c) of close-up for $case\ II$. The results of both cases indicate that the predicted crack paths perform similarly with the experimental results reported by [Bittencourt et al., 1996]. Additionally four stages of the predicted crack propagation by the proposed XCQ4 (Std) for $case\ I$ are shown in Fig. 5.15 to reveal the kinematic characteristics of crack evolving procedure, which provides a visual impression on specific crack growth process.

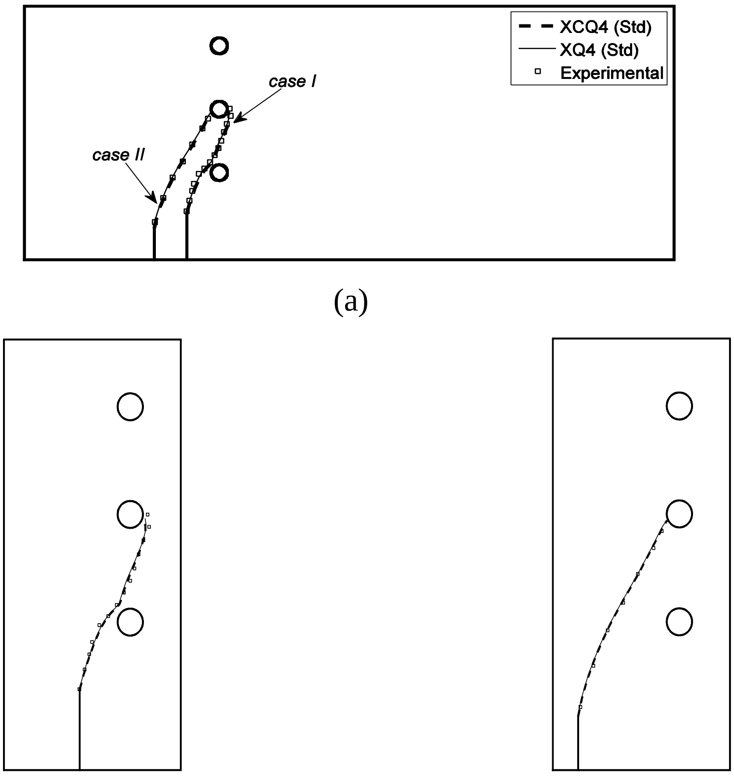

(a)

(b) (c)

Fig. 5.14 Comparison of the predicted crack growth trajectories with experimental results (a) and the close-up of the results around holes for (b) $case\ I$; (c) $case\ II$.

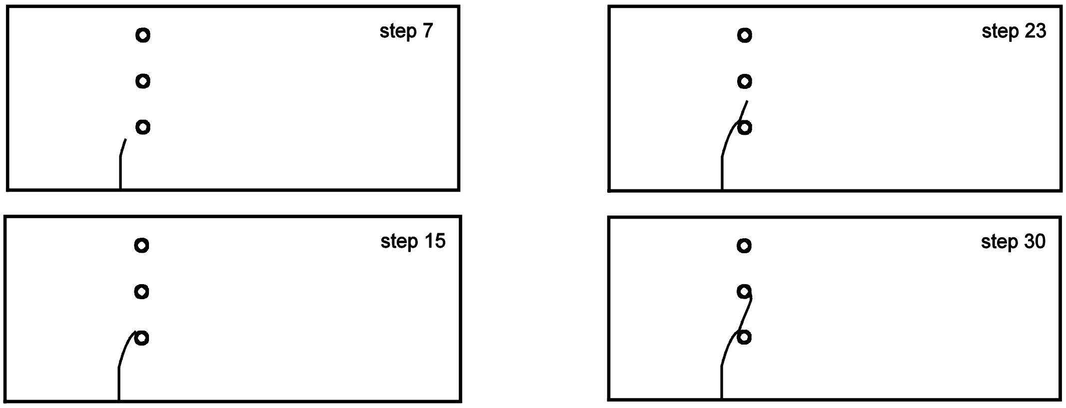

Fig. 5.15 Specific crack growth characteristics at different steps.

The SIFs plots for both two cases are depicted in Fig. 5.16. In $case\ I$ it is obvious that a larger drop of SIFs occurred when the crack trajectory approaching the lower hole. The difference of SIFs plots of XCQ4 and XQ4 can be discovered in the tail of the evolution, which accounts for the distinction of two predicted crack paths by XCQ4 (Std) and XQ4 (Std) in Fig.

5.14(b). Nonetheless the SIFs plots for both cases have a good agreement with each other overall.

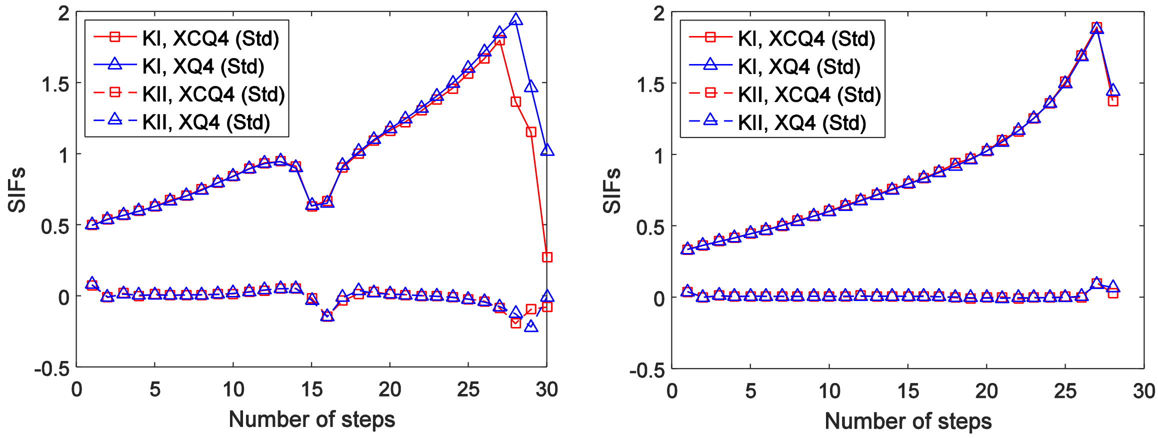

(a) (b)

Fig. 5.16 SIFs plots in total growth steps for (a) $case\ I$; (b) $case\ II$.

5.6 A Cruciform Specimen with An Edge Crack

To investigate the applicability of the proposed XCQ4 method for modelling crack evolution in complicated configuration and the effect of loading direction on the crack growth trajectory, a cruciform specimen with an edge crack under two types of loading condition is selected as illustrated in Fig. 5.17. The plain strain conditions are considered and the specimen is determined by the following geometric parameters 2L=330 mm, 2S=200 mm, 2H=150 mm, 2W=100 mm with a crack-length $a = 10\,mm$ and $\theta = 45^o$. The Young's modulus $E = 1000Pa$ and the Poisson's ratio $\nu = 0.37$ are chosen. Two directions of imposed loading are assumed to analyze the crack growth trajectory, which is defined as $type\ I$: the upper edge of specimen is subjected to the tension $\sigma = 1$ as shown in Fig. 5.17(a), while $type\ II$: the same tension force is imposed on the right edge as shown in Fig. 5.17(b). In both cases the displacements along the entire bottom edge are completely constrained and the same unstructured discretization of 3809 elements is used.

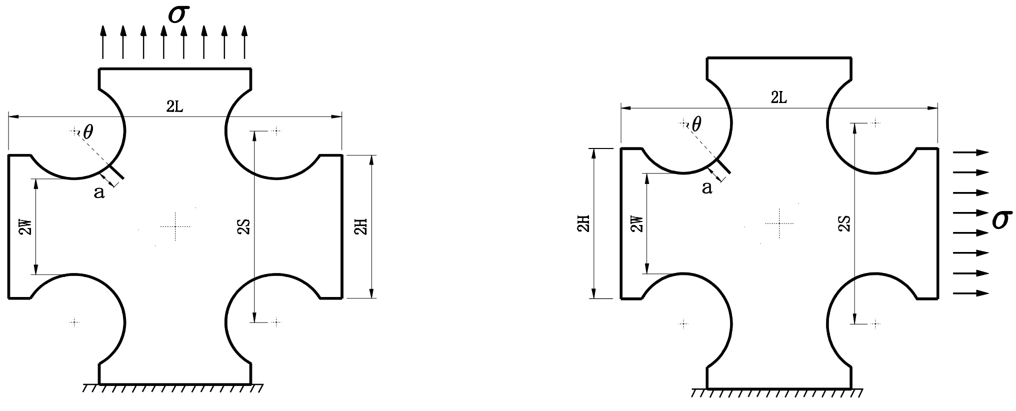

(a) (b)

Fig. 5.17 Geometry of the cruciform specimen with two boundary conditions: (a) $type\ I$; (b) $type\ II$.

The crack incremental size is taken to be $\Delta a = 5$ in this case and a total number of 20 steps are performed to simulate the crack evolution. The crack paths are computed numerically by using both the developed XCQ4 (Std) and conventional XQ4 (Std) method as shown in Fig. 5.18 for $type\ I$ and $type\ II$. As observed in results the crack path of $type\ I$ generally proceeds toward the horizontal direction until the opposite arc-shaped edge of the specimen, which tends to destroy the structure by cutting the top part of the cruciform and the deformed shape of structure at final growth step is sketched in Fig. 5.19(a). Whereas in $type\ II$ the crack initiates downward and spreads toward the lower right arc-shaped edge of the structure and it is a tendency to split the specimen completely from the middle part of the structure and the deformed configuration at final growth step is shown in Fig. 5.19(b). The amplification factor of 5 is used in this case to plot the displacement deformation to distinctly present the crack propagation path and the damage zone. Due to the novelty of the example there is no available reference solution in literature to validate the accuracy of the crack growth trajectory yielded by XCQ4 (Std) and XQ4 (Std). However it is clear that the crack paths in Fig. 5.18 agree very well with each other. Based on the verification of aforementioned four numerical examples, the numerical results of this case is prone to be convinced. In particular the normal stress contour plots of specimen at last incremental step are displayed in Fig. 5.19 to visualize the stress field of crack tip.

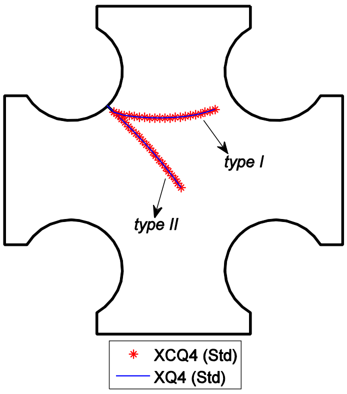

Fig. 5.18 Comparison of the predicted crack paths obtained by XCQ4 and XQ4 under different types of boundary condition: (a) $type\ I$ and (b) $type\ II$.

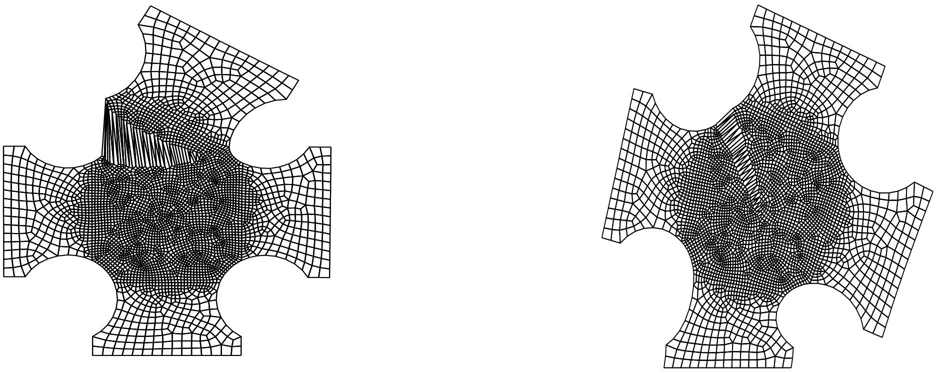

(a) (b)

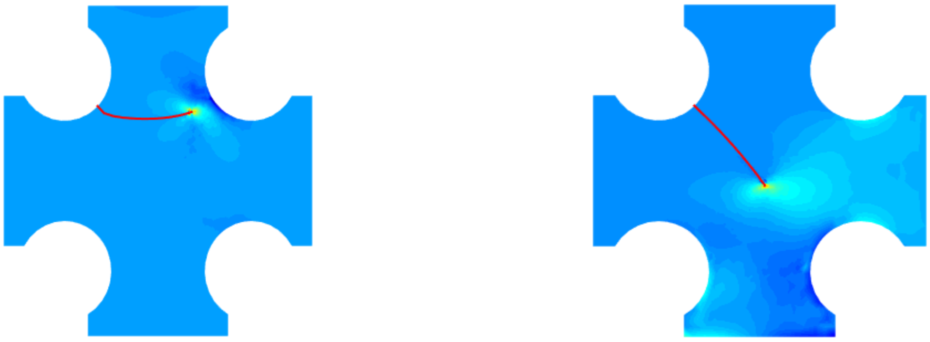

$type\ I$ XCQ4 (Std) $type\ II$ XCQ4 (Std)

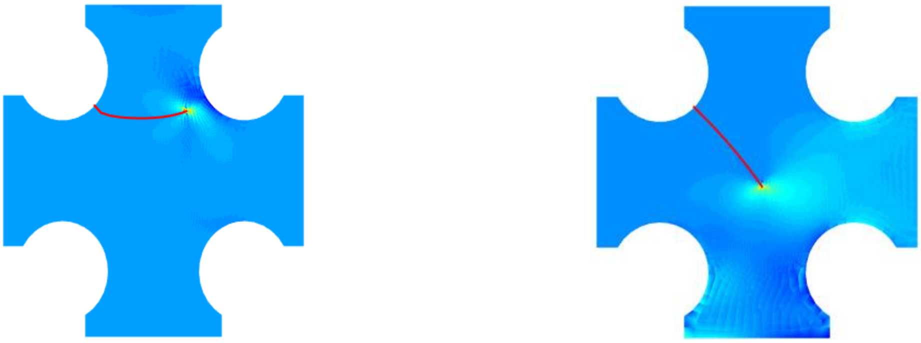

$type\ I$ XQ4 (Std) $type\ II$ XQ4 (Std)

Fig. 5.19 Deformed forms of the specimen at the last growth step for (a) $type\ I$ and (b) $type\ II$; Comparison of normal stress σ_{xx} distribution at the final step.

5.7 A Square Plate with Two Cracks

In the final numerical example the evolution of two cracks in a square plate of width 2 under the tension $\sigma = 1$ is simulated as shown in Fig. 5.20. The bottom of the specimen is fixed and the mesh is structured mesh 50x50. It should be mentioned that there is no available analytical and experimental solution for this problem. The vertical distance d of the two cracks will range from 0.15, 0.45 and 0.75. Due to the major influence of crack 1 on the structure damage, it is assumed that firstly the crack 1 of length 0.3 will propagate following the direction determined by the criterion of maximum circumferential stress, while the crack 2 of length 0.3 stays static until the junction between two cracks comes out. The location of two cracks can be given by the parameter of $a = 1$. Therefore the influence of the distance between two cracks on the predicted crack path can be evaluated in this example. The algorithm for exploring junction element and junction approximation is the same as the one of [Budyn et al., 2004]. In the element containing the junction of two cracks, a Heaviside-junction enrichment $\bar{J}(\mathbf{x})$ is used to represent the effect of junction as shown in Eq. (5.3). The signed distance function $f^n(\mathbf{x})$ of the 'Minor' crack and $f^N(\mathbf{x})$ of the 'Main' crack is defined respectively in Fig. 5.21.

$$\bar{J}_J^n(\mathbf{x}) = \begin{cases} H\left(f^n(\mathbf{x})\right) - H\left(f^n(\mathbf{x}_J)\right) & \mathit{for}\ x \in A_1 \\ H\left(f^N(\mathbf{x})\right) - H\left(f^N(\mathbf{x}_J)\right) & \mathit{for}\ x \in A_2 \end{cases} \tag{5.3}$$

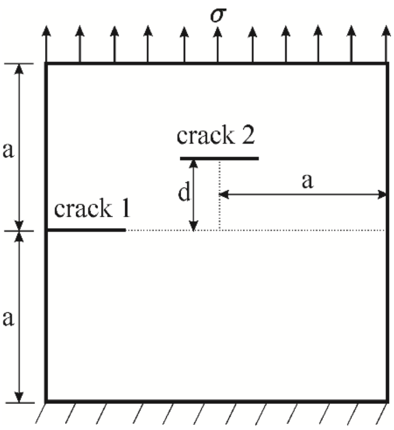

Fig. 5.20 Geometry of the plate with two horizontal cracks.

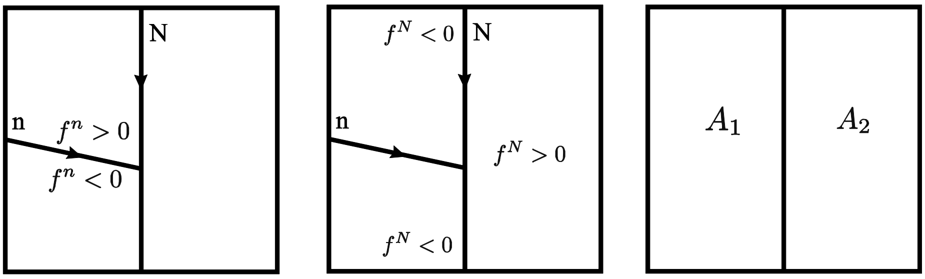

Fig. 5.21 The values of signed distance function for 'Main' crack N and 'Minor' crack n in junction element.

The crack propagates with incremental size of 0.1 which is practicable as stated in [Budyn et al., 2004]. The predicted crack paths computed by XCQ4 (Std) for four cases are summarized in Fig. 5.22(a) and the comparison of numerical results draw from XCQ4 (Std) and XQ4 (Std) in each case is plotted in Figs. 5.22(b)-(e) respectively. Through observing the predicted crack paths affected by the distance of two cracks it is found that if two crack are far from each other ($d = 0.75$ and $d = 0.45$) the crack 1 propagates with approaching crack 2 whereas there is no junction between two cracks as illustrated in Figs. 5.22(b) and (c). However if two cracks are located closely ($d = 0.15$ and $d = 0.05$) crack 1 growths toward crack 2 until the junction takes place and the connected crack propagates cooperatively as shown in Figs. 5.22(d) and (e).

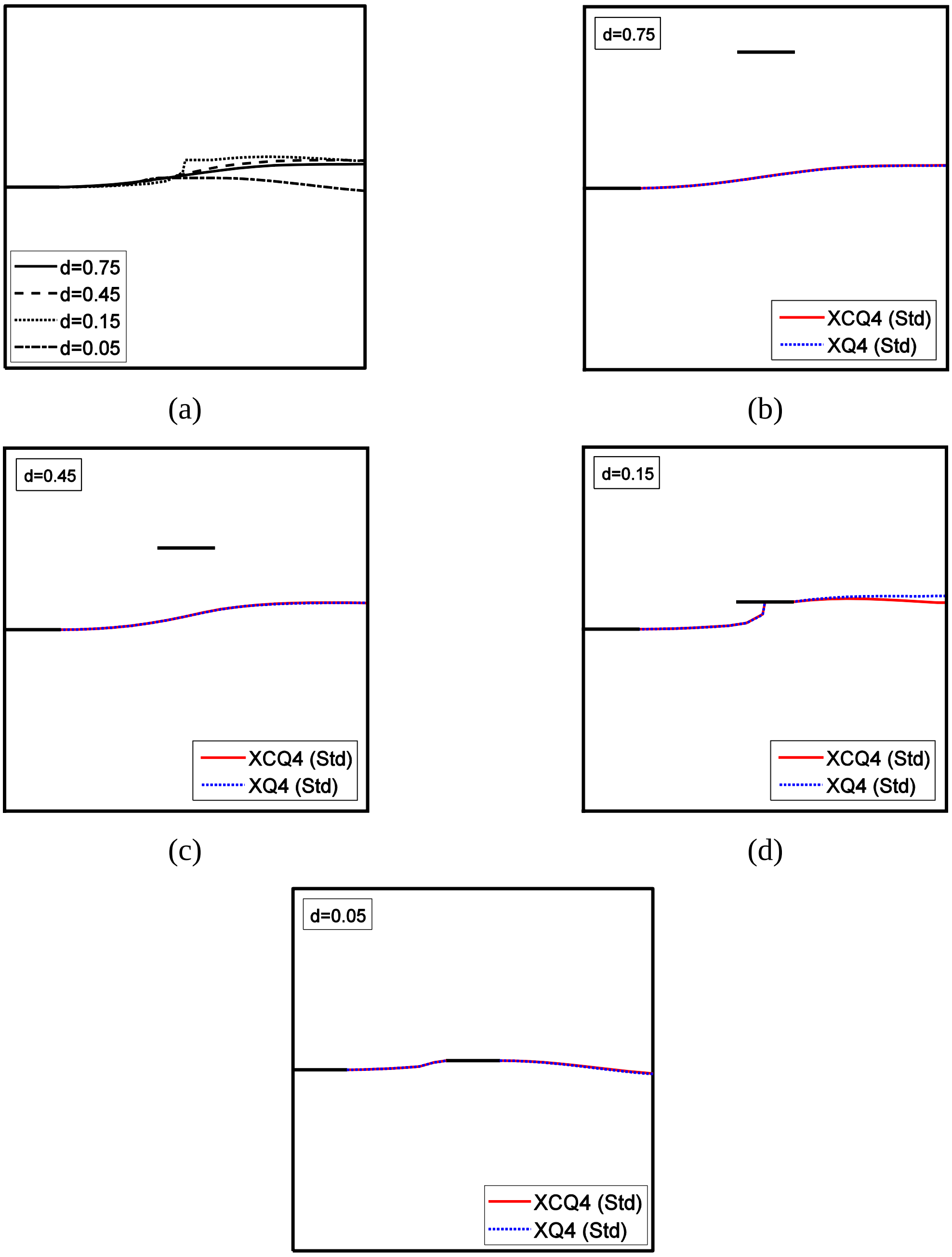

(a) (b) (c) (d) (e)

Fig. 5.22 The predicted crack paths in different distances of two cracks.

5.8 Summary

In this work the crack evolution problem is solved by using a robust finite element method based on the consecutive-interpolation procedure (CIP) containing both nodal values and averaged nodal gradients as interpolation conditions. Taking advantage of the outstanding performance of XCQ4 demonstrated in section 3 and section 4, the crack growth issues are figured out in terms of maximum circumferential stress criterion to determine the crack propagation orientation and the domain form of interaction integral to calculate the stress intensity factors. The new developed method is particularly effective for modeling crack growth in contrast with classical FEM which needs remeshing at each incremental step.

CHAPTER 6

DYNAMIC CRACK ANALYSIS OF SOLIDS & COMPOSITES

6.1 Introduction

In this chapter, the application of present approach for investigating transient dynamic stress intensity factors (DSIFs) of isotropic and orthotropic materials in 2D space is presented. The proposed numerical mechanism is an effective finite element approach composing of enrichment function and consecutive-interpolation procedure (CIP). Comparing with traditional FE methods, XCQ4 involves both nodal values and averaged nodal gradients as interpolation conditions to smooth the distribution of variables. In XCQ4, the crack interface is determined by level set function and enriched by Heaviside and crack-tip enrichment functions within the principle of partition of unity. These special functions have been developed in the literature for diverse media such as isotropic, anisotropic, piezoelectric etc. composite materials. In this work the anisotropic enriched functions for crack tip are considered. In addition, The Newmark time integration scheme is adopted to solve for the discrete equations of XCQ4 method at each time step and there is no consideration about the effects of velocity-based global damping matrix. The proposed method is verified through a series of numerical examples regarding transient fracture analysis in isotropic and anisotropic materials. Numerical DSIFs in disparate cases are presented and compared with reference solutions available in literature. The behaviors of dynamic responses are explored in specimens with complex configuration under step load and sine load.

For the loading conditions of the considered numerical examples, two types: $type\ I{:}\,Step\ loading$ and $type\ II{:}\,Sine\ loading$ are taken into account as shown in Fig. 6.1.

(a) (b)

Fig. 6.1 (a) Step loading; (b) Sine loading.

6.2 Fracture Analysis for Two-dimensional Orthotropic Material

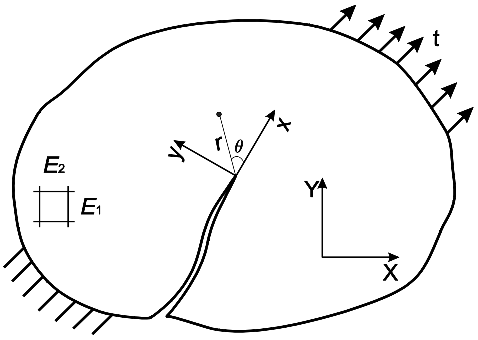

Fig. 6.2 Boundary condition for an arbitrary cracked orthotropic domain.

Assume a two-dimensional cracked anisotropic solid subjected to traction $\mathbf{t}$ as shown in Fig. 6.2. Global coordinate system (X,Y), local coordinate (x,y) and local crack tip polar coordinate system (r,θ) are defined, respectively. The relationship between stress and strain for linear elastic material can be written as:

$$\varepsilon_{ij} = s_{ijpq}\sigma_{pq} \quad (i, j, p, q = 1, 2, 3) \tag{6.1}$$

where ε_{ij}, σ_{pq} and S_{ijpq} are components of linear strain tensor, stress tensor and fourth-order compliance tensor respectively. For simple implementation, the compact form of Eq. (6.1) can be rewritten as:

$$\varepsilon_{\alpha} = a_{\alpha\beta}\sigma_{\beta} \quad (\alpha, \beta = 1, 2, 3) \tag{6.2}$$

Upon considering equilibrium and compatibility conditions [Carloni et al., 2003], a fourth-order partial differential equation can be obtained as:

$$a_{11}\mu^{4} - 2a_{16}\mu^{3} + (2a_{12} + a_{66})\mu^{2} - 2a_{26}\mu + a_{22} = 0 \tag{6.3}$$

The roots of Eq. (6.3) are always in conjugate pairs as $(\mu_1, \overline{\mu_1})$, and $(\mu_2, \overline{\mu_2})$. The displacement and stress fields in the vicinity of the crack tip has been elaborated by [Asadpoure et al., 2007]. Based on the analytical functions and complex variables$(Z_k = x + \mu_k y_k;\ k = 1,2\ )$, the corresponding expression of displacements and stresses for pure mode I are presented in Eqs. (6.4-1)-(6.4-5).

$$u_1 = K_I\sqrt{\frac{2r}{\pi}}\,\mathrm{Re}\left[\frac{1}{\mu_1 - \mu_2}\left\{\mu_1 p_2\sqrt{\cos\theta + \mu_2\sin\theta} - \mu_2 p_1\sqrt{\cos\theta + \mu_1\sin\theta}\right\}\right] \tag{6.4-1}$$

$$u_2 = K_I\sqrt{\frac{2r}{\pi}}\,\mathrm{Re}\left[\frac{1}{\mu_1 - \mu_2}\left\{\mu_1 q_2\sqrt{\cos\theta + \mu_2\sin\theta} - \mu_2 q_1\sqrt{\cos\theta + \mu_1\sin\theta}\right\}\right] \tag{6.4-2}$$

$$\sigma_{11} = \frac{K_I}{\sqrt{2\pi r}}\,\mathrm{Re}\left[\frac{\mu_1\mu_2}{\mu_1 - \mu_2}\left\{\frac{\mu_2}{\sqrt{\cos\theta + \mu_2\sin\theta}} - \frac{\mu_1}{\sqrt{\cos\theta + \mu_1\sin\theta}}\right\}\right] \tag{6.4-3}$$

$$\sigma_{22} = \frac{K_I}{\sqrt{2\pi r}}\,\mathrm{Re}\left[\frac{1}{\mu_1 - \mu_2}\left\{\frac{\mu_1}{\sqrt{\cos\theta + \mu_2\sin\theta}} - \frac{\mu_2}{\sqrt{\cos\theta + \mu_1\sin\theta}}\right\}\right] \tag{6.4-4}$$

$$\sigma_{12} = \frac{K_I}{\sqrt{2\pi r}}\,\mathrm{Re}\left[\frac{\mu_1\mu_2}{\mu_1 - \mu_2}\left\{\frac{1}{\sqrt{\cos\theta + \mu_1\sin\theta}} - \frac{1}{\sqrt{\cos\theta + \mu_2\sin\theta}}\right\}\right] \tag{6.4-5}$$

In the same manner, Eqs. (6.5-1)-(6.5-5) are displacements and stresses for pure mode II.

$$u_1 = K_{II}\sqrt{\frac{2r}{\pi}}\,\mathrm{Re}\left[\frac{1}{\mu_1-\mu_2}\left\{p_2\sqrt{\cos\theta+\mu_2\sin\theta}-p_1\sqrt{\cos\theta+\mu_1\sin\theta}\right\}\right] \tag{6.5-1}$$

$$u_2 = K_{II}\sqrt{\frac{2r}{\pi}}\,\mathrm{Re}\left[\frac{1}{\mu_1-\mu_2}\left\{q_2\sqrt{\cos\theta+\mu_2\sin\theta}-q_1\sqrt{\cos\theta+\mu_1\sin\theta}\right\}\right] \tag{6.5-2}$$

$$\sigma_{11} = \frac{K_{II}}{\sqrt{2\pi r}}\,\mathrm{Re}\left[\frac{1}{\mu_1-\mu_2}\left\{\frac{\mu_2{}^2}{\sqrt{\cos\theta+\mu_2\sin\theta}}-\frac{\mu_1{}^2}{\sqrt{\cos\theta+\mu_1\sin\theta}}\right\}\right] \tag{6.5-3}$$

$$\sigma_{22} = \frac{K_{II}}{\sqrt{2\pi r}}\,\mathrm{Re}\left[\frac{1}{\mu_1-\mu_2}\left\{\frac{1}{\sqrt{\cos\theta+\mu_2\sin\theta}}-\frac{1}{\sqrt{\cos\theta+\mu_1\sin\theta}}\right\}\right] \tag{6.5-4}$$

$$\sigma_{12} = \frac{K_{II}}{\sqrt{2\pi r}}\,\mathrm{Re}\left[\frac{1}{\mu_1-\mu_2}\left\{\frac{\mu_1}{\sqrt{\cos\theta+\mu_1\sin\theta}}-\frac{\mu_2}{\sqrt{\cos\theta+\mu_2\sin\theta}}\right\}\right] \tag{6.5-5}$$

where Re represents the real part of the value and K_I and K_{II} are stress intensity factors for mode I and mode II, respectively. p_k and q_k can be calculated by

$$p_k = a_{11}\mu_k{}^2 + a_{12} - a_{16}\mu_k \tag{6.6}$$

$$q_k = a_{12}\mu_k + a_{22}/\mu_k - a_{26} \tag{6.7}$$

6.3 Computation of DSIFs for Isotropic and Orthotropic Solids

The dynamic stress intensity factors (DSIFs) is one main parameter to evaluate the dynamic fracture response in the vicinity of the crack tip. Based on the calculation of the DSIFs, the fracture behavior of cracked bodies with different material properties become predictable. Thus it is preferred to compare with DSIFs derived from other approaches in open literature to investigate the precision of XCQ4 method. Usually interaction integral formulated by superimposing the actual field ($\sigma_{ij}^{(1)}$, $\varepsilon_{ij}^{(1)}$, $u_{ij}^{(1)}$) and auxiliary field ($\sigma_{ij}^{(2)}$, $\varepsilon_{ij}^{(2)}$, $u_{ij}^{(2)}$) on the path independent J integral is adopted for computation of SIFs. Thus the analytical form [Liu et al., 2012] of the J integral can be written as:

$$J^{d} = \int_{A}\left(\sigma_{ij}\partial u_{i,1} - (W-K)\delta_{1j}\right)q_{,j}dA + \int_{A}\left((\rho\ddot{u}_{i} - f_{i})\partial u_{i,1} - \rho\partial\dot{u}_{i,1}\dot{u}_{i}\right)qdA \tag{6.8}$$

where $W = 1/2\,\sigma_{ij}\varepsilon_{ij}$ and $K = 1/2\,\rho\dot{u}_{i}\dot{u}_{i}$ are the strain energy density and kinetic energy density, respectively. q is a function of smoothly changing from $q = 1$ adjacent crack tip to $q = 0$ over the exterior boundary. Additional explanation about the impact of the function q on calculation of interaction integral can be found in section 5.

The relationship between J integral and stress intensity factors (K_I, K_{II}) in the case of mixed mode failure can be represented as:

$$J^{d} = \frac{1}{E^{*}}\left(K_{I}^{2} + K_{II}^{2}\right) \tag{6.9}$$

where

$$E^{*} = \begin{cases} E & \text{plane stress} \\ \dfrac{E}{1-\upsilon^{2}} & \text{plane strain} \end{cases} \tag{6.10}$$

By simplifying the above equations, J integral can be rewritten as:

$$\boldsymbol{J^{d} = J^{(1)} + J^{(2)} + I^{(1,2)}} \tag{6.11}$$

where $J^{(1)}$ and $J^{(2)}$ are J integrals for actual state and auxiliary states, respectively. $I^{(1,2)}$is the interaction integral and can be calculated by:

$$I^{(1,2)} = \int_{A}\left(\sigma_{ij}^{(1)}u_{i,1}^{(2)} + \sigma_{ij}^{(2)}u_{i,1}^{(1)} - \sigma_{ik}^{(2)}\varepsilon_{ik}^{(1)}\delta_{1j}\right)q_{,j}dA + \int_{A}\rho\ddot{u}_{i}^{(1)}u_{i,1}^{(2)}qdA \tag{6.12}$$

The relationship between the SIFs (K_I, K_{II}) and the interaction integral for isotropic material is expressed as:

$$I^{(1,2)} = \frac{2\left(K_{I}^{(1)}K_{I}^{(2)} + K_{II}^{(1)}K_{II}^{(2)}\right)}{E^{*}} \tag{6.13}$$

$$K_{I}^{(1)} = \left(E^{*}/2\right)I^{(1,I)}; \quad K_{II}^{(1)} = \left(E^{*}/2\right)I^{(1,II)} \tag{6.14}$$

For orthotropic material, the relationship can be defined as:

$$I^{(1,2)}=2c_{11}K_I^{(1)}K_I^{(2)}+c_{12}\left(K_I^{(1)}K_{II}^{(2)}+K_I^{(2)}K_{II}^{(1)}\right)+2c_{22}K_{II}^{(1)}K_{II}^{(2)} \tag{6.15}$$

where

$$c_{11}=-\frac{a_{22}}{2}\operatorname{Im}\left(\frac{\mu_1+\mu_2}{\mu_1\mu_2}\right) \tag{6.16}$$

$$c_{12}=-\frac{a_{22}}{2}\operatorname{Im}\left(\frac{1}{\mu_1\mu_2}\right)+\frac{a_{11}}{2}\operatorname{Im}\left(\mu_1\mu_2\right) \tag{6.17}$$

$$c_{22}=-\frac{a_{11}}{2}\operatorname{Im}\left(\mu_1+\mu_2\right) \tag{6.18}$$

By setting the values of $(state\ 1\text{: } K_I^{(2)}=1,\ K_{II}^{(2)}=0)$ and $(state\ 2\text{: } K_I^{(2)}=0,$ $K_{II}^{(2)}=1)$, the actual mixed –mode stress intensity factors can be obtained through solving linear algebraic equations:

$$K_I^{(1)}=2c_{11}I^{(1,I)}+c_{12}I^{(1,II)} \tag{6.19}$$

$$K_{II}^{(1)}=c_{12}I^{(1,I)}+2c_{22}I^{(1,II)} \tag{6.20}$$

It is worth to stress out that the support domain for the element considered in *J*-domain in terms of the XCQ4 is larger than that used in XFEM as illustrated in Fig. 3.12. The reason is the implementation of the larger span formed by neighboring elements of the CIP framework.

6.4 Basic Formulation of Dynamic XCQ4

6.4.1 Approximations for Cracks

The XCQ4 composes of standard and enriched terms with additional functions to capture the effect of discontinuity. Assume one particular node of $\mathbf{x}_i$, the extended XCQ4 approximation of the displacement with respect to fracture can be written as:

$$\begin{aligned}\mathbf{u}^h(\mathbf{x}) &= \sum_{i\in W_s}\tilde{N}_i(\mathbf{x})\mathbf{u}_i + \sum_{j\in W_c}\tilde{N}_j(\mathbf{x})\left[H(\mathbf{x})-H(\mathbf{x}_j)\right]\mathbf{a}_j \\ &+ \sum_{k\in W_t}\tilde{N}_k(\mathbf{x})\sum_{\alpha=1}^{4}\left[F^\alpha(\mathbf{x})-F^\alpha(\mathbf{x}_k)\right]\mathbf{b}_k^\alpha\end{aligned} \tag{6.21}$$

where $\widetilde{N}_i(\mathbf{x})$ denotes CQ4 shape function for node i that contains high order polynomials. W_s, $W_c$and W_t are the sets of standard nodes, Heaviside enriched nodes and crack tip enriched nodes respectively. $\mathbf{u}_i$ is the nodal displacement vector at node i. $\mathbf{a}_j$ and $\mathbf{b}_k^\alpha$ signifies the nodal additional DOFs associated with Heaviside and asymptotic enrichment functions, respectively. $H(\mathbf{x})$ is the modified discontinuous enrichment function:

To compute the effect of discontinuity on the stress and displacement field in the vicinity of crack tip, the representation of crack-tip functions for orthotropic composites should consider all displacement fields given in Eqs. (6.4-1), (6.4-2), (6.5-1) and (6.5-2). Thus, the crack-tip functions for orthotropic solid can be obtained with similar form of those reported in [Asadpoure et al., 2006, 2007]

$$\left[F^\alpha(\mathbf{x})|_{\alpha=1}^4\right]=\left[\sqrt{r}\cos\left(\frac{\theta_1}{2}\right)\sqrt{g_1(\theta)},\sqrt{r}\cos\left(\frac{\theta_2}{2}\right)\sqrt{g_2(\theta)},\sqrt{r}\sin\left(\frac{\theta_1}{2}\right)\sqrt{g_1(\theta)},\sqrt{r}\sin\left(\frac{\theta_2}{2}\right)\sqrt{g_2(\theta)}\right] \tag{6.22}$$

where $\mathrm{g}_p(\theta)$ and θ_p $(p = 1{,}2)$ are defined as

$$g_p(\theta)=\sqrt{\left(\cos\theta+\mu_{px}\sin\theta\right)^2+\left(\mu_{py}\sin\theta\right)^2} \tag{6.23}$$

$$\theta_p = arctg\left(\frac{\mu_{py}\sin\theta}{\cos\theta+\mu_{px}\sin\theta}\right) \tag{6.24}$$

Then, standard branch functions $F_\alpha(\mathbf{x})|_{\alpha=1}^4$ derived from a linear elastic isotropic material is adopted to enrich asymptotic field near crack

$$\left[F^\alpha(\mathbf{x})|_{\alpha=1}^4\right]=\left[\sqrt{r}\sin\left(\frac{\theta}{2}\right),\sqrt{r}\cos\left(\frac{\theta}{2}\right),\sqrt{r}\sin\left(\frac{\theta}{2}\right)\sin(\theta),\sqrt{r}\cos\left(\frac{\theta}{2}\right)\sin(\theta)\right] \tag{6.25}$$

where (r,θ) is the polar coordinate system.

6.4.2 Spatial Discretization in Dynamic Domain

In the case of the elastodynamic problem, the XCQ4 method is developed in conjunction with quadrilateral elements to analyze the dynamic fracture response in several cases. The displacement $\mathbf{u}$, the velocity $\dot{\mathbf{u}}$ and the acceleration $\ddot{\mathbf{u}}$ should approximate via function expressed in Eq. (6.21). The weak form for the discrete problem can be written as:

$$\int_{\Omega} \delta\mathbf{u}^T \ddot{\mathbf{u}} \rho d\Omega + \int_{\Omega} \nabla_s \delta\mathbf{u} : \boldsymbol{\sigma} d\Omega - \int_{\Omega} \delta\mathbf{u}^T \bar{\mathbf{b}} \rho d\Omega - \int_{\Gamma_t} \delta\mathbf{u}^T \bar{\mathbf{t}} \rho d\Gamma = 0 \tag{6.26}$$

where $\delta\mathbf{u}$ is the variational trial funcions.

Upon substituting the XCQ4 approximation function of Eq. (6.21) into the weak form Eq. (6.26), the discrete form can be gained as follows:

$$\mathbf{M}\ddot{\mathbf{u}} + \mathbf{K}\mathbf{u} = \mathbf{F} \tag{6.27}$$

where $\mathbf{M}$ and $\mathbf{K}$ are the global mass and global stiffness matrices assembled by each element. $\mathbf{F}$ is the vector of global external force. These matrices can be constructed as follow:

$$\mathbf{M}_{ij} = \begin{bmatrix} \mathbf{M}_{ij}^{uu} & \mathbf{M}_{ij}^{ua} & \mathbf{M}_{ij}^{ub} \\ \mathbf{M}_{ij}^{au} & \mathbf{M}_{ij}^{aa} & \mathbf{M}_{ij}^{ab} \\ \mathbf{M}_{ij}^{bu} & \mathbf{M}_{ij}^{ba} & \mathbf{M}_{ij}^{bb} \end{bmatrix} \tag{6.28}$$

$$\mathbf{K}_{ij} = \begin{bmatrix} \mathbf{K}_{ij}^{uu} & \mathbf{K}_{ij}^{ua} & \mathbf{K}_{ij}^{ub} \\ \mathbf{K}_{ij}^{au} & \mathbf{K}_{ij}^{aa} & \mathbf{K}_{ij}^{ab} \\ \mathbf{K}_{ij}^{bu} & \mathbf{K}_{ij}^{ba} & \mathbf{K}_{ij}^{bb} \end{bmatrix} \tag{6.29}$$

$$\begin{aligned} \mathbf{u}_i &= \left\{ \mathbf{u}_i^u, \mathbf{u}_i^a, \mathbf{u}_i^b \right\} \\ \ddot{\mathbf{u}}_i &= \left\{ \ddot{\mathbf{u}}_i^u, \ddot{\mathbf{u}}_i^a, \ddot{\mathbf{u}}_i^b \right\} \\ \mathbf{F}_i &= \left\{ \mathbf{F}_i^u, \mathbf{F}_i^a, \mathbf{F}_i^b \right\} \end{aligned} \tag{6.30}$$

where

$$\begin{aligned} \mathbf{M}_{ij}^{rs} &= \int_{\Omega^e} \rho \left(\tilde{\mathbf{N}}_i^r \right)^T \tilde{\mathbf{N}}_j^s d\Omega \qquad (r,s = u,a,b) \\ \mathbf{K}_{ij}^{rs} &= \int_{\Omega^e} \left(\tilde{\mathbf{B}}_i^r \right)^T \mathbf{D} \tilde{\mathbf{B}}_j^s d\Omega \qquad (r,s = u,a,b) \end{aligned} \tag{6.31}$$

$$\begin{aligned}
\mathbf{F}_i^u &= \int_{\Omega^e} \tilde{\mathbf{N}}_i \bar{\mathbf{b}} d\Omega + \int_{\Gamma_t} \tilde{\mathbf{N}}_i \bar{\mathbf{t}} d\Gamma \\
\mathbf{F}_i^a &= \int_{\Omega^e} \tilde{\mathbf{N}}_i \left(H(\mathbf{x}) - H(\mathbf{x}_i)\right) \bar{\mathbf{b}} d\Omega + \int_{\Gamma_t} \tilde{\mathbf{N}}_i \left(H(\mathbf{x}) - H(\mathbf{x}_i)\right) \bar{\mathbf{t}} d\Gamma \\
\mathbf{F}_i^b &= \int_{\Omega^e} \tilde{\mathbf{N}}_i \left(F_\alpha(\mathbf{x}) - F_\alpha(\mathbf{x}_i)\right) \bar{\mathbf{b}} d\Omega + \int_{\Gamma_t} \tilde{\mathbf{N}}_i \left(F_\alpha(\mathbf{x}) - F_\alpha(\mathbf{x}_i)\right) \bar{\mathbf{t}} d\Gamma \quad (\alpha = 1,2,3,4)
\end{aligned} \tag{6.32}$$

In these equations, $\tilde{\mathbf{N}}_i$ and $\tilde{\mathbf{B}}_i^u$ are the shape function and displacement gradient matrices of the XCQ4 algorithm for standard nodes, and the terms $\tilde{\mathbf{B}}_i^a$ and $\tilde{\mathbf{B}}_i^b$ are gradient matrices for enriched nodes given by

$$\begin{aligned}
\tilde{\mathbf{B}}_i^u &= \begin{bmatrix} \tilde{N}_{i,x} & 0 \\ 0 & \tilde{N}_{i,y} \\ \tilde{N}_{i,y} & \tilde{N}_{i,x} \end{bmatrix} \\
\tilde{\mathbf{B}}_i^a &= \begin{bmatrix} \left(\tilde{N}_i\left(H(\mathbf{x}) - H(\mathbf{x}_i)\right)\right)_{,x} & 0 \\ 0 & \left(\tilde{N}_i\left(H(\mathbf{x}) - H(\mathbf{x}_i)\right)\right)_{,y} \\ \left(\tilde{N}_i\left(H(\mathbf{x}) - H(\mathbf{x}_i)\right)\right)_{,y} & \left(\tilde{N}_i\left(H(\mathbf{x}) - H(\mathbf{x}_i)\right)\right)_{,x} \end{bmatrix} \\
\tilde{\mathbf{B}}_i^b &= \begin{bmatrix} \left(\tilde{N}_i\left(F_\alpha(\mathbf{x}) - F_\alpha(\mathbf{x}_i)\right)\right)_{,x} & 0 \\ 0 & \left(\tilde{N}_i\left(F_\alpha(\mathbf{x}) - F_\alpha(\mathbf{x}_i)\right)\right)_{,y} \\ \left(\tilde{N}_i\left(F_\alpha(\mathbf{x}) - F_\alpha(\mathbf{x}_i)\right)\right)_{,y} & \left(\tilde{N}_i\left(F_\alpha(\mathbf{x}) - F_\alpha(\mathbf{x}_i)\right)\right)_{,x} \end{bmatrix} \quad (\alpha = 1,2,3,4)
\end{aligned} \tag{6.33}$$

6.4.3 Alternative Time Integration Criterion

In this work, the general Newmark integration is adopted for iterating in the time domain, which has been widely employed for transient dynamic crack analyses. In the case of linear acceleration in each time step and zero viscous damping, the acceleration form can be gained as follow:

$$\left(\mathbf{M} + \beta\Delta t^2\mathbf{K}\right)\ddot{\mathbf{u}}_n = \mathbf{F}_n^{ext} - \mathbf{K}(\mathbf{u}_{n-1} + \Delta t\dot{\mathbf{u}}_{n-1} + \frac{\Delta t^2}{2}(1-2\beta)\ddot{\mathbf{u}}_{n-1}) \tag{6.34}$$

where $\mathbf{F}_n^{ext}$ is the vector of global external force, $n-1$ and n signifies the last step and the present step, respectively and Δt is the time step. If the value of $\ddot{\mathbf{u}}_n$ is known, $\mathbf{u}_n$ and $\dot{\mathbf{u}}_n$

can be evaluated by following equations:

$$\mathbf{u}_n = \mathbf{u}_{n-1} + \Delta t\dot{\mathbf{u}}_{n-1} + \Delta t^2(0.5-\beta)\ddot{\mathbf{u}}_{n-1} + \beta\Delta t^2\ddot{\mathbf{u}}_n \tag{6.35}$$

$$\dot{\mathbf{u}}_n = \dot{\mathbf{u}}_{n-1} + \left(1-\gamma\right)\Delta t\ddot{\mathbf{u}}_{n-1} + \gamma\Delta t\ddot{\mathbf{u}}_n \tag{6.36}$$

where γ and β are equal to 0.5 and 0.25 to make the method implicit and unconditionally stable with the second order accuracy [Song et al., 2006].

The following procedure describes the implementation of the Newmark integration method without considering damping effects.

a) Assemble the global stiffness matrix $\mathbf{K}$ and mass matrix $\mathbf{M}$.

b) Assume the initial displacement and velocity condition, then compute the first acceleration variable by the equilibrium equation:

$$\mathbf{M}\ddot{u}_{\boldsymbol{int}} + \mathbf{K}\mathbf{u}_{\boldsymbol{int}} = \mathbf{f}_{\boldsymbol{int}} \tag{6.37}$$

c) Evaluate the integration constants:

$$\begin{gathered} a_0 = 1/(\beta\Delta t^2)\,, a_1 = \alpha/(\beta\Delta t),\ a_2 = 1/(\beta\Delta t); \\ a_3 = 1/(2\beta) - 1\,, a_4 = \alpha/\beta - 1,\ a_5 = (\Delta t/2)/\big((\alpha/\beta) - 2\big); \\ a_6 = \Delta t(1-\alpha),\ a_7 = \alpha\Delta t. \end{gathered} \tag{6.38}$$

d) Calculate the effective stiffness matrix

$$\bar{\mathbf{K}} = \mathbf{K} + a_0\mathbf{M} \tag{6.39}$$

e) Iteration for each time step

  i. Obtain the effective loads at time $t + \Delta t$

$$\bar{\mathbf{f}}_{\boldsymbol{t+\Delta t}} = \mathbf{f}_{\boldsymbol{t+\Delta t}} + \mathbf{M}(a_0\mathbf{u}_t + a_2\dot{\mathbf{u}}_t + a_3\ddot{\mathbf{u}}_t) \tag{6.40}$$

  ii. Determine the displacements by solving

$$\bar{\mathbf{K}}\mathbf{u}_{t+\Delta t} = \bar{\mathbf{f}}_{t+\Delta t} \tag{6.41}$$

  iii. Compute the accelerations and the velocities

$$\begin{gathered} \ddot{\mathbf{u}}_{t+\Delta t} = a_0(\mathbf{u}_{t+\Delta t} - \mathbf{u}_t) - a_2\dot{\mathbf{u}}_t - a_3\ddot{\mathbf{u}}_t \\ \dot{\mathbf{u}}_{t+\Delta t} = \dot{\mathbf{u}}_t + a_6\ddot{\mathbf{u}}_t + a_7\ddot{\mathbf{u}}_{t+\Delta t} \end{gathered} \tag{6.42}$$

6.5 Edge Cracked Isotropic Semi-infinite Plate

6.5.1 Initial Parameters

In the context of homogenous property, the accuracy of DSIFs calculation by this method is confirmed for the edge cracked plate with geometric parameters as $H = 300mm$, $W = 200mm$, $d = 150mm$ and $a = 50mm$. Because the far filed of wave motions will not influence the dynamic response of crack tip in this case, the finite dimension of specimen is considered. The imposed velocity v is set to be $6.5m/s$ and arise on the upper half of left edge as shown in Fig. 6.3. For other boundary, traction is free in this numerical example. The steel material is chosen with properties of Young's modulus $E = 200GPa$, density $\rho = 7850kg/m^3$ and Poisson's ratio $\upsilon = 0.25$. Also, a plain strain condition is prescribed. The same problem was solved by [Song et al., 2006] using the displacement correlation technique (DCT) and [Lee et al., 1990] using linear superposition of stress wave solutions. Both relevant numerical solutions are taken as the reference solutions to verify the robustness of the proposed method. The total mesh is 2417 elements including regular and irregular elements as shown in Fig. 6.3. The time step $\Delta t = 0.4\text{x}10^{-6}s$ is taken into account in the average acceleration method. The longitudinal wave speed C_d can be obtained based on the basis material properties as follows:

$$C_d = \sqrt{\frac{E(1-\upsilon)}{\rho(1+\upsilon)(1-2\upsilon)}} = 5529.3m/s \tag{6.43}$$

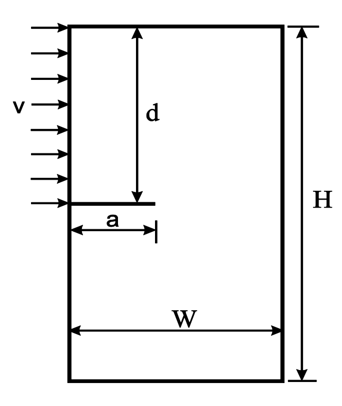

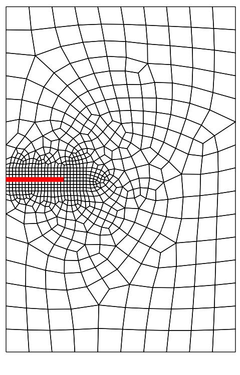

Fig. 6.3 Geometry of the edge cracked plate problem.

6.5.2 Effect of Discretization Size

The obtained numerical results are compared with the analytical solutions reported by [Lee et al., 1990] and reference solution given by [Song et al., 2006] in terms of DCT method as shown in Fig. 6.4. The horizontal axis denotes the value of normalized time $C_d t/a$. The ordinate axis signifies the normalized DSIFs by $E\upsilon\sqrt{a/\pi}/(2C_d(1-\upsilon^2))$. The time history of DSIFs is shown for the time from the initial loading to the first arrival of the scattered wave at the crack tip. The negative and positive values of K_I and K_{II} are induced, respectively when the stress waves generated by the imposed load reach the crack tip. It is clearly observed that the present numerical solution has satisfactory agreement with other solutions.

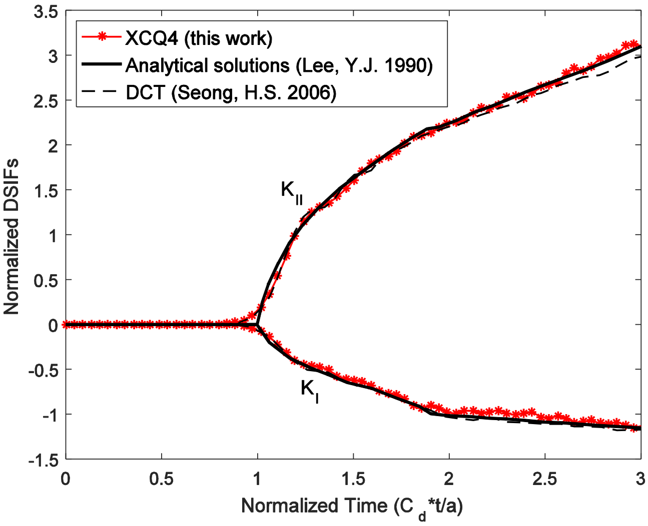

Fig. 6.4 Comparison of normalized DSIFs history with reference solutions.

The effect of mesh density on the accuracy of obtained numerical DSIFs is investigated for the same numerical example. Three discretization sizes are used as 25x7, 43x13 and 61x19. The comparison among the normalized DSIFs for three mesh arrangements as well as the analytical solution is given in Fig. 6.5. The results indicate that the coarse mesh will induce the deviation from the analytical solution at earlier initial time and relatively apparent oscillations occur throughout the whole duration. Whereas better coincidence is obtained between the analytical solution and numerical results obtained by finer mesh. It is concluded that the mesh size has influence on the accuracy of DSIFs and an appropriate mesh arrangement is necessary.

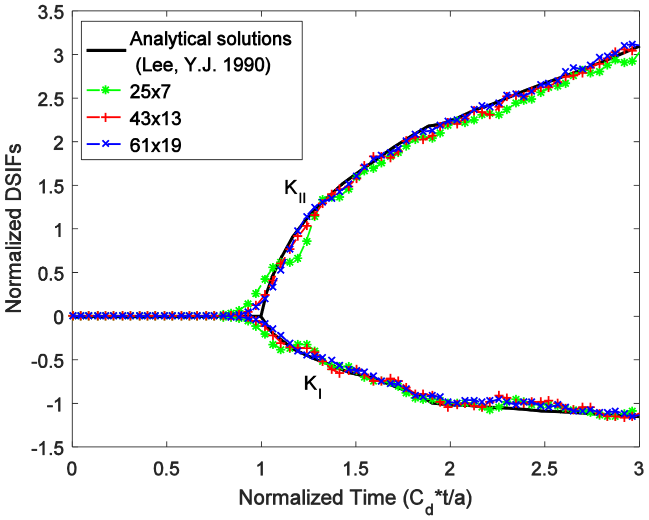

Fig. 6.5 Effect evaluation of mesh density on normalized DSIFs history.

6.5.3 Investigation of Different Crack Position

For the edge cracked semi-infinite plate, it is obvious that the DSIFs should not be affected by the vertical distance d defined from top edge to crack face as shown in Fig. 6.3, which means if the distance d switches the value and other conditions are fixed, the time histories of DSIFs under different d values are identical with each other. Upon the basis, three examinations of $d = 3H/6$, $d = 4H/6$ and $d = 5H/6$ are performed to investigate the stability of the developed method and the comparison is shown in Fig. 6.6. Since the wave reflection from the outer boundary needs much more time to reach the crack front, results obtained from different crack locations are close to each other, which has proven the reliable application of the XCQ4 for capturing the transient dynamic response in isotropic solid. Fig. 6.7 shows the comparison of numerical results derived from the XCQ4 and standard XQ4 method, it is obvious that curve obtained by the XCQ4 is closer to the analytical solution than that of the XQ4.

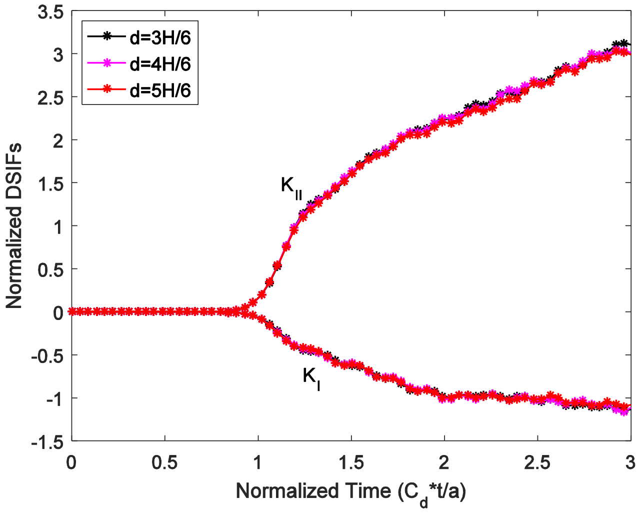

Fig. 6.6 Predicted time history of normalized DSIFs by XCQ4 under different d.

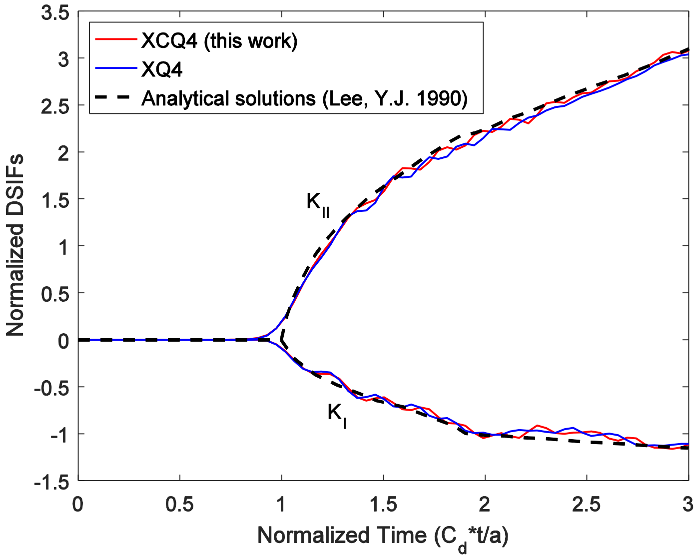

Fig. 6.7 Comparison of normalized DSIFs histories between XCQ4 and XQ4 method.

6.6 Center Crack Tension (CCT) Specimen

Assume a center cracked rectangular plate with dimension of $H = 40mm$, $W = 20mm$ and the total 50x100 structured elements distribution is used as shown in Fig. 6.8. The crack length is set to be $a = 4.8mm$ and a plain strain condition is assumed. The instantaneous tension load σ_o is applied to both top and bottom edges as displayed in Fig. 6.1(a). No additional boundary restrictions are imposed on the specimen. The isotropic material parameters for this analysis are: Young's modulus $E = 199.992GPa$, density $\rho = 5000kg/m^3$ and Poisson's ratio $\upsilon = 0.3$, and the corresponding longitudinal wave speed can be calculated as $C_d = 7340m/s$ by Eq. (6.43). The numerical simulation is conducted by setting the time step $\Delta t = 0.05\text{x}10^{-6}s$.

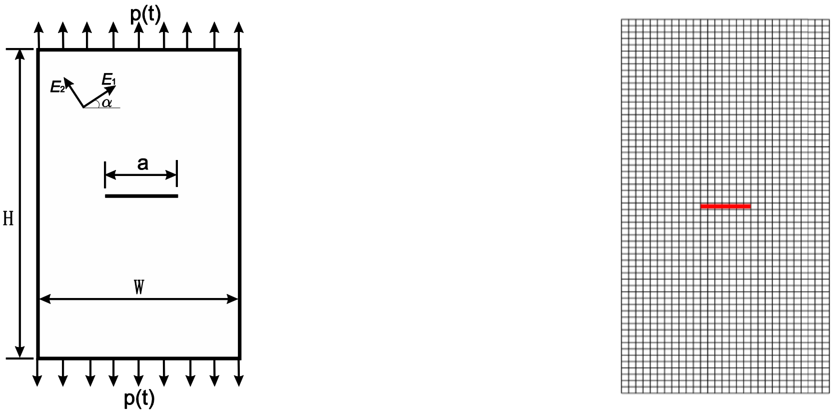

Fig. 6.8 Configuration of the plate with a central crack.

6.6.1 Isotropic Case

In Fig. 6.9, the obtained DSIF K_I is compared with the reference solution of FEM [Song et al., 2006]. The horizontal axis is the normalized time with respect to longitudinal wave speed C_d and the vertical axis is normalized by$\sigma_o(\sqrt{\pi a/2})$. Fig. 6.9 indicates that time variations of the normalized DSIFs calculated by XCQ4 are consistent with the reference solution. It should be noted that the mesh refinement in the vicinity of crack tip is necessary in FEM as implemented by [Song et al., 2006] whereas XCQ4 can work accurately ignoring this implementation.

To explore the sensitivity of the developed method to a time interval, DSIF K_I is calculated for various time increments $2C_d\Delta t = H/10$ to $2C_d\Delta t = H/60$ as shown in Fig. 6.10. The numerical results show that for the larger time step, the earlier initial rise time is observed and the fluctuations in response become larger. Overall the DSIFs time histories in all cases resemble reference solution well. It then concludes that the XCQ4 method is applicable for evaluating dynamic fracture response in a CCT isotropic specimen.

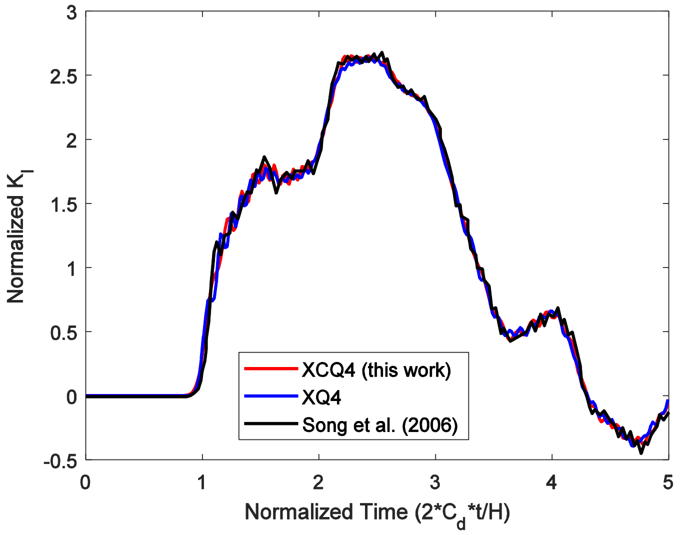

Fig. 6.9 Comparison between predicted time history of normalized mode I DSIF by XCQ4 and reference solution in isotropic solid.

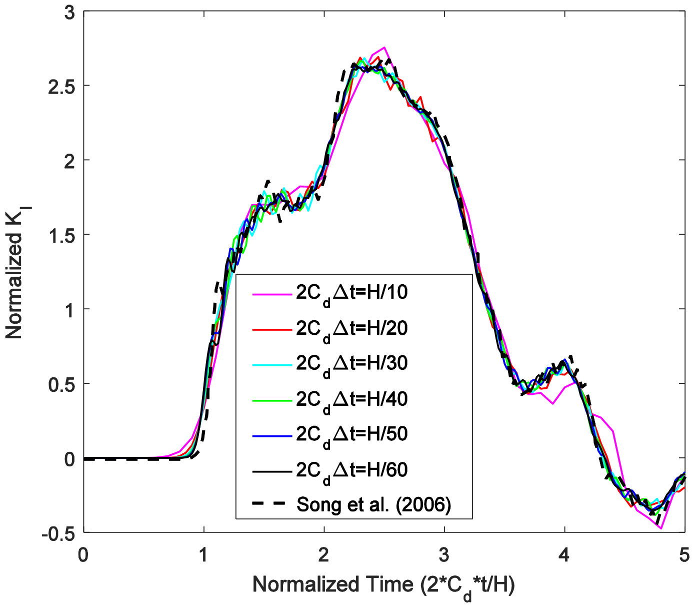

Fig. 6.10 Comparison of predicted mode I normalized DSIF history in different time steps in isotropic solid.

6.6.2 Orthotropic Case

Next, the performance of XCQ4 for solving transient dynamic fracture problem in orthotropic material is investigated using the same CCT specimen. For this case a plane stress condition is considered and the composite material properties are prescribed as: $E_1 = 118.30GPa$, $E_2 = 54.80GPa$, $G_{12} = 8.79GPa$, $\upsilon_{12} = 0.083$, and $\rho = 1900kg/m^3$. The time step $\Delta t = H/(80C_L)$ is taken into account and the same normalized coordinate axis as in the isotropic case is adopted. The wave speed along the E_2 material axis is defined as $C_L = \sqrt{C_{22}/\rho}$. Two reference solutions given by [Felipe et al., 2008] using a boundary element method and [Nguyen et al., 2016] employing an extended meshfree method are selected as references to validate the robustness of the XCQ4 method. As seen in Fig. 6.11, very similar behavior can be obtained for these numerical methods, which certifies the feasibility of XCQ4 method for investigating dynamic fracture behaviors in an orthotropic solid.

For the center crack model in the orthotropic plate, the effect of mesh density on the time variation of DSIFs is investigated. Four patterns of mesh discretization, i.e. 20x40, 30x60, 40x80 and 50x100 are considered. In Fig. 6.12, shows that the results approach to the reference solution with the increasing of mesh density. The initial time and peak value of the dynamic response has slight discrepancy when the coarse mesh is considered.

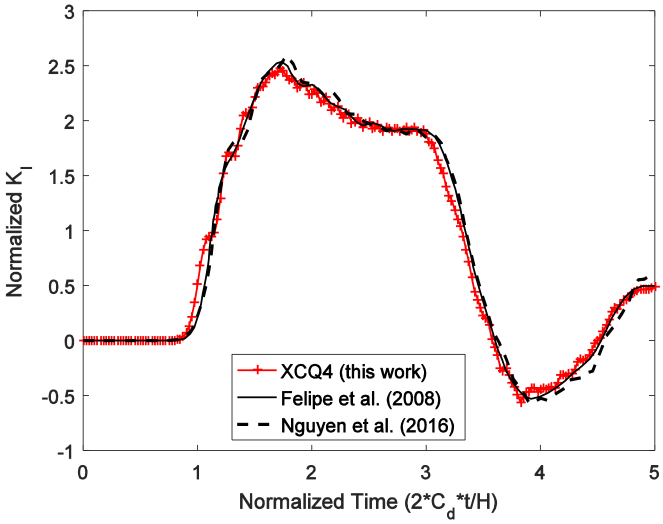

Fig. 6.11 Comparison between predicted mode I normalized DSIF history calculated by XCQ4 and reference solution in orthotropic solid.

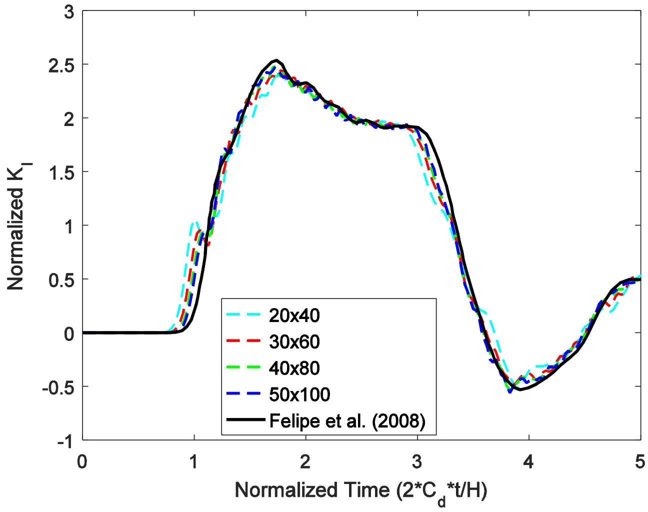

Fig. 6.12 Effect evaluation of mesh density on mode I normalized DSIF history calculated by XCQ4 in orthotropic solid.

On account of the significance of DSIFs response in orthotropic composites depending on the orientations of the orthotropy, the completely anisotropic material characteristics in a plane stress condition are estimated by determining the degree of the material anisotropy through the matrix transformation of the elastic constants. In this work, the inclination angle of material α between the principle axis of material 1 and crack orientation is equal to 0^o, 15^o, 30^o, $45^o$and 60^o respectively. In Fig. 6.13 and Fig. 6.14, the normalized results of DSIFs K_I and

K_{II} obtained by XCQ4 are plotted, respectively. The available reference solutions in [Felipe et al., 2008] and [Nguyen et al., 2016] are taken for comparison. Consequently, similar dynamic responses for both failure modes can be observed, which distinctly points out that the developed XCQ4 method can precisely forecast the instantaneous dynamic fracture responses in anisotropic material.

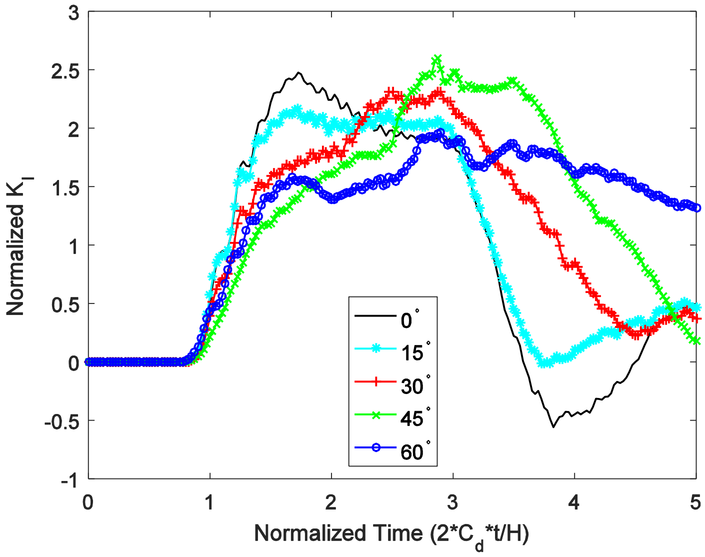

Fig. 6.13 Normalized mode I DSIF history for anisotropic case.

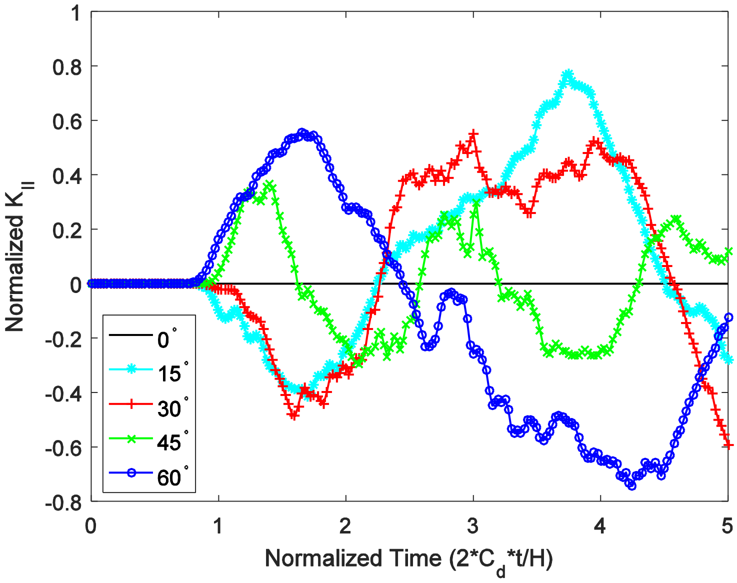

Fig. 6.14 Normalized mode II DSIF history for anisotropic case.

6.7 Edge Cracked Plate with Complex Configuration

This example is to demonstrate the applicability of XCQ4 by reporting DSIFs fracture behaviors in anisotropic material with special configuration. The geometrical shape of the model and discretization are schematically depicted in Fig. 6.15. The related parameters are prescribed as: $H = 60mm$, $L = 70mm$, $S = 20mm$, $D = 35mm$, $d = 30mm$ and $w = 20mm$. As shown in Fig. 6.1, either of two types of dynamic loadings is partially imposed on the right hand of the top edge; $type\ I: \sigma(t) = \sigma_o H(t)$ and $type\ II: \sigma(t) = \sigma_o sin(\omega t)$ with $\omega = 2\pi/(50\text{x}10^{-6})$, $\sigma_o = 7.5\text{x}10^{6}$Pa. The boundary constraints in x direction are set for all nodes on the left edge. Similarly, the nodes of bottom edge are restricted in y direction. The initial crack length is given as $a = 18mm$ and the discretization of the domain is adopted as 1934 regular and irregular elements.

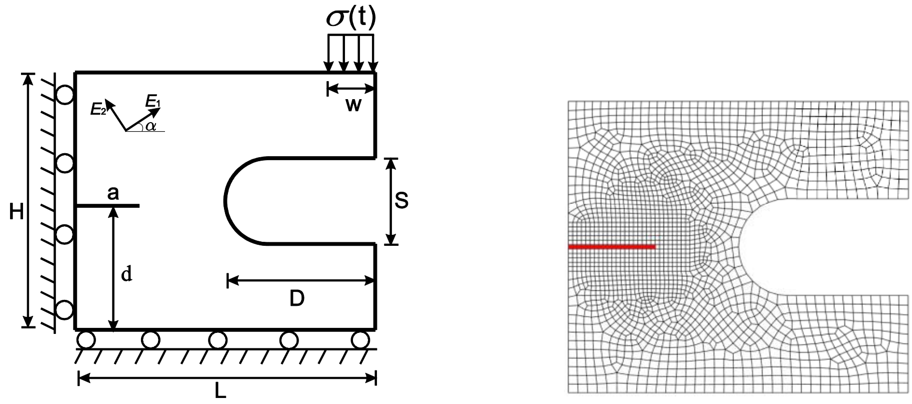

Fig. 6.15 Sophisticated geometry and discretization of edge cracked specimen.

6.7.1 Isotropic Case

The isotropic material properties are adopted as: Young's modulus$E = 2.1\text{x}10^{11}$Pa, mass density $\rho = 7850kg/m^3$ and Poisson's ratio $\upsilon = 0.285$. The same problem has been resolved numerically by [Nguyen et al., 2016] using the extended meshfree radial point interpolation method (X-RPIM). The corresponding results are used as the reference to verify the capability and performance of the proposed XCQ4 method.

The dynamic fracture behavior calculated by XCQ4 under two types of loading condition are collected and presented in Fig. 6.16 and Fig. 6.17. The ordinate coordinate is the normalized DSIFs with respect to $\sigma_o(\sqrt{\pi a})$ and the horizontal axis is time history. Upon comparing with reference solution, there is a satisfactory agreement between two results and it can be found out that the results solved under sine loading condition present smooth dynamic behavior whereas the obvious oscillation can be observed in those under step loading.

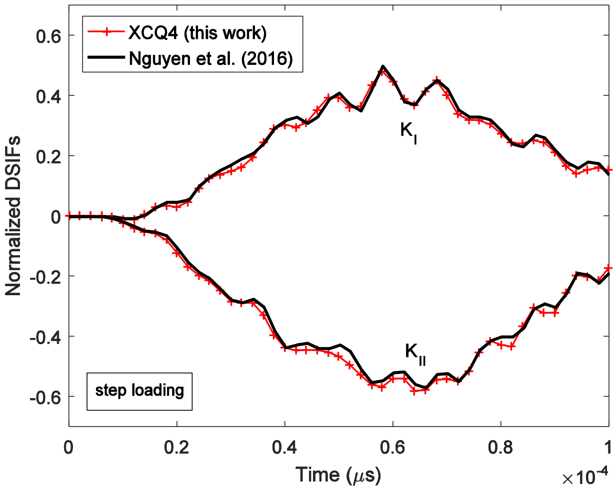

Fig. 6.16 Comparison of the normalized DSIFs by XCQ4 and reference solution under step loading condition in isotropic material.

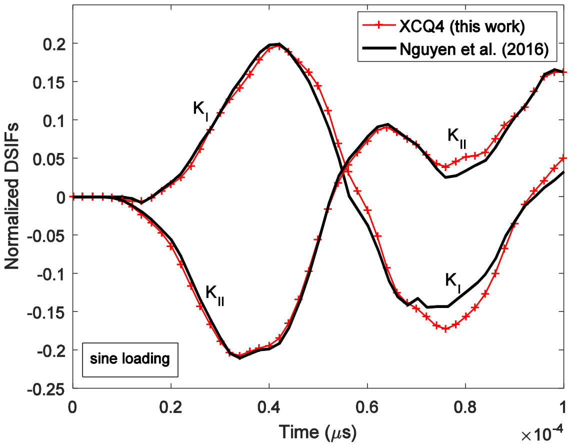

Fig. 6.17 Comparison of the normalized DSIFs by XCQ4 and reference solution under sine loading condition in isotropic material.

6.7.2 Orthotropic Case

Then, orthotropic material parameters in this example are chosen as the same material constants in the second example and plane stress condition is assumed. The orthotropic material property is assigned to this structure and the corresponding dynamic fracture behavior is probed with variation of orthotropic angles such as 0^o, 15^o, 30^o, $45^o$and 60^o. Fig. 6.18 shows time variations of DSIFs K_I and K_{II} normalized by $\sigma_o(\sqrt{\pi a})$ under a step loading. The earlier initial time can be found in the case of inclination material angle α equal to 45^o for both failure modes of DSIFs. In the same manner, the relationship between two variables are evaluated under sine loading condition are shown in Fig. 6.19, similar tendency of dynamic fracture response can be obtained and no evident oscillation exists.

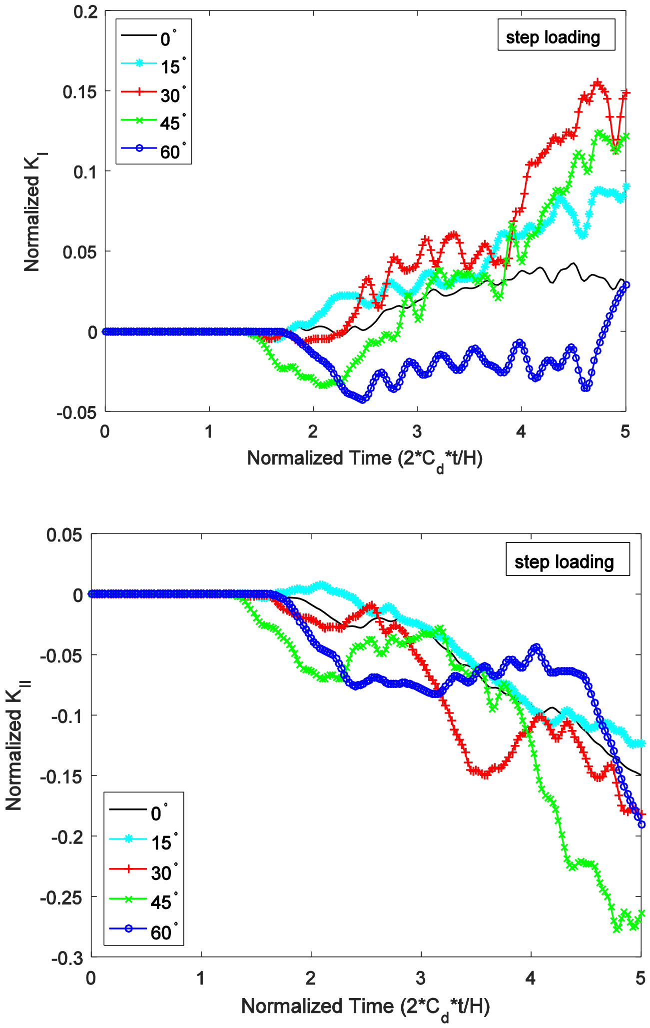

Fig. 6.18 The predicted normalized DSIFs history for anisotropic case under step loading.

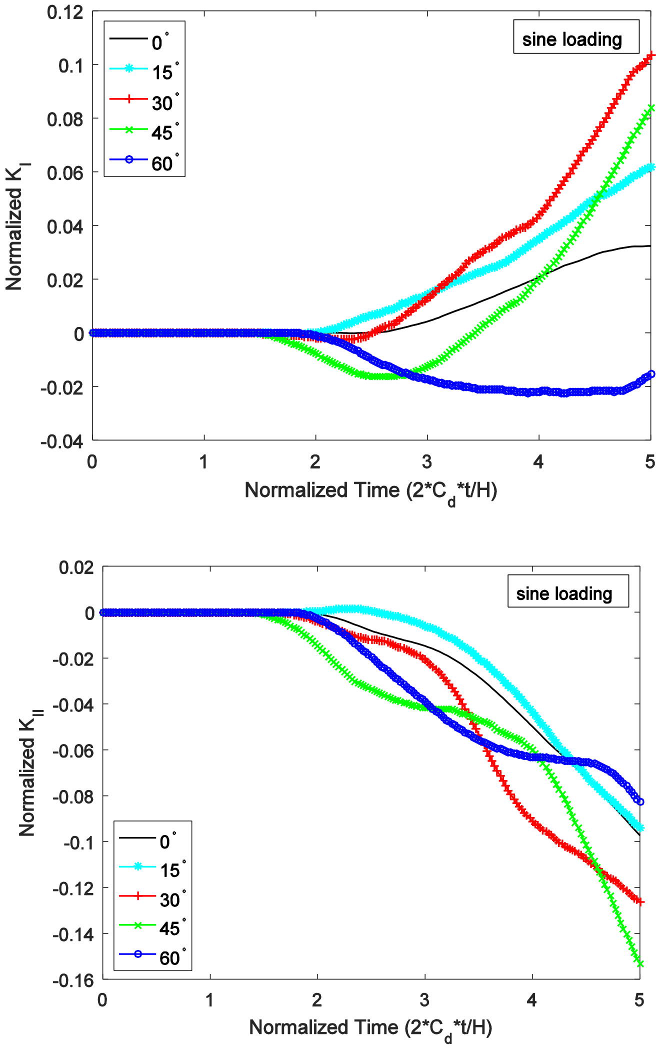

Fig. 6.19 The predicted normalized DSIFs history for anisotropic case under sine loading.

To reveal the effect of crack length on the characteristics of dynamic fracture behavior in orthotropic material, provides a visualization on the correlation of normalized DSIFs and time history on condition that the principle axis of material 1 is perpendicular to the normal of crack orientation. Five values of the crack length $a = 9{,}14{,}18{,}21mm$ are considered in this investigation. Based on the numerical results in Fig. 6.20, the initial time of each case almost the same, however it is interesting that the normalized values of both failure modes arise with decreasing the crack length. As expected, oscillation problem occur more frequently in step loading condition than in sine loading condition because of the propagation and reflection of the elastic stress waves in solids [Nguyen et al., 2016].

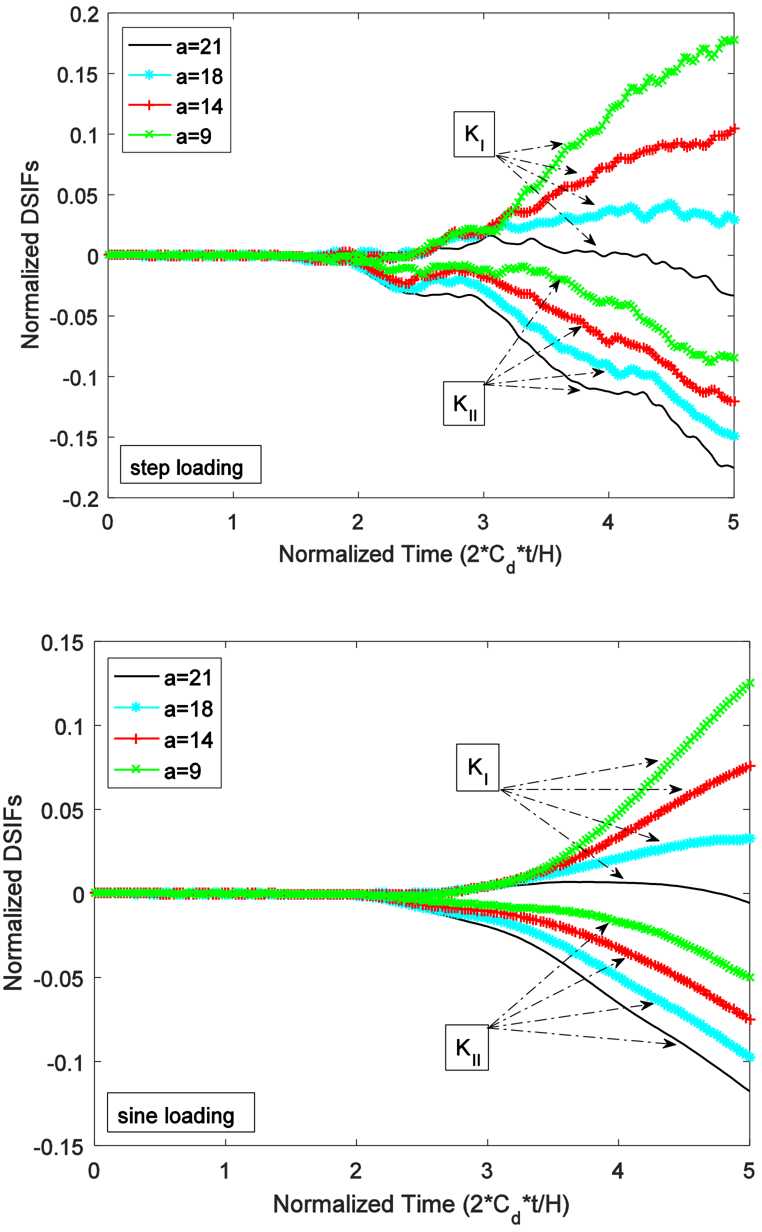

Fig. 6.20 The prediction for the influence of crack length on the normalized DSIFs history under different loading conditions.

6.8 Plate with a Central Hole and Two Cracks

Final example to be considered is a plate with geometry size of height $H = 60mm$ and width $W = 30mm$. One central hole with radius $r = 3.75mm$ and two cracks located at each horizontal side of the hole are set as shown in Fig. 6.21. The distance between two crack tips is $2a = 15mm$. A step loading introduced in Fig. 6.21(a) and plane stress condition is assumed without any other boundary constraints. Totally the plate is discretized into 1842 elements as illustrated in Fig. 6.21(b).

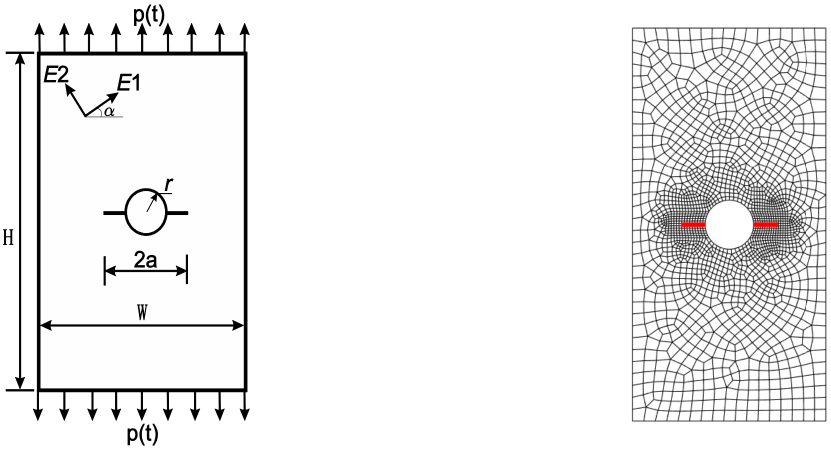

Fig. 6.21 Configuration of the plate with a central hole and two cracks.

6.8.1 Quasi-isotropic and Orthotropic Material

Two types of material with respect to $\alpha = 0^o$ are taken into account to capture the dynamic fracture response of this case. First the Quasi-isotropic material parameters are: Young's modulus$E_1 = 220GPa, E_2 = 219GPa,$ shear modulus $G_{12} = 76.92GP,$ density $\rho = 5000kg/m^3$ and Poisson's ratio $\upsilon_{12} = 0.4286$. For the orthotropic case, the longitudinal elastic moduli are taken as $E_1 = 220GPa, E_2 = 440GPa$ and other material properties keep identical with the quasi-isotropic case. The numerical simulations proceed with setting the time step $\Delta t = 0.28\text{x}10^{-6}s$ for quasi-isotropic material and $\Delta t = 0.4\text{x}10^{-6}s$ for the orthotropic material and full integration scheme are required.

The numerical results reflecting the time history of normalized mode-I DSIF with respect to $\sigma_o(\sqrt{\pi a})$ are illustrated in Fig. 6.22. The reference solutions for isotropic case are supported by [Agnantiaris et al., 1996] using the dual reciprocity principle and [Albuquerque et al., 2004] in terms of Dual boundary element method (DBEM). In the results comparison of orthotropic case, [Albuquerque et al., 2004] offers the reference solution obtained by the discretization of one quarter of the plate via traction singular quarter point element. Both cases provides similar dynamic fracture response between numerical results gained by XCQ4 and reference solutions, although some slight deviation in regard of peak values can be found in each case. Due to the stiffer material property along longitudinal orientation in orthotropic material, the initial time of the dynamic fracture response is earlier than that of the quasi-isotropic case. Besides, the peak value of the normalized mode-I DSIFs in quasi-isotropic case is larger than those in orthotropic case.

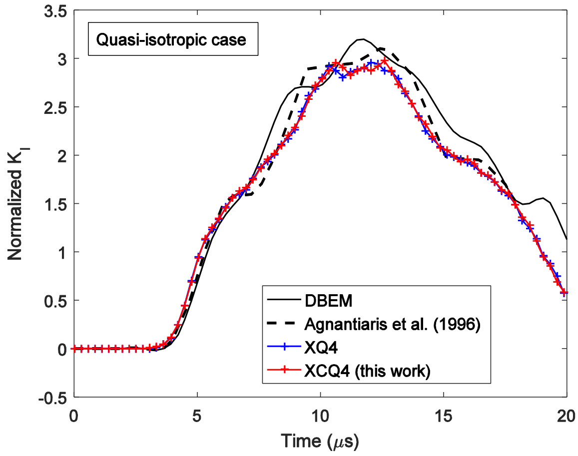

(a)

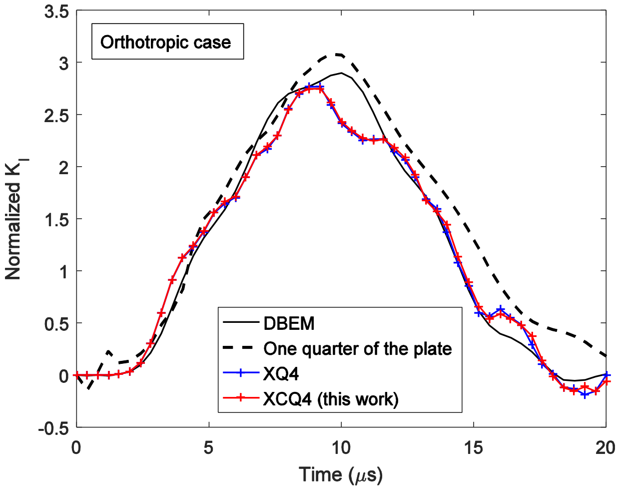

(b)

Fig. 6.22 The predicted normalized mode-I DSIF history for quasi-isotropic case (a) and orthotropic case (b) under step loading.

6.9 Summary

In this chapter, the dynamic fracture issues in isotropic and anisotropic solids using a new developed finite element method (XCQ4) featuring the consecutive-interpolation procedure (CIP) including both nodal values and averaged nodal gradients were solved. The higher accuracy of XCQ4 for calculating SIFs in static fracture problem has been demonstrated in section 4, the better performance of XCQ4 was proven compared with tradition extended finite element (XFEM). The purpose of this study is to extend the application of XCQ4 for solving transient dynamic problem and convince the robustness and feasibility of new approach in various materials involving discontinuity. In conjunction with the physical fields such as displacement, stress etc. close to the crack tip in orthotropic solid, the instantaneous dynamic problems are figured out in terms of an average acceleration integration theme (Newmark method) with the zero damping matrix to determine the dynamic stress intensity factors under the framework of XCQ4. As mentioned before, main desirable characteristics of XCQ4 can be listed as (1) unlike traditional FEM, remeshing procedure is no longer needed for solving crack propagation issue; (2) modelling of discontinuity is arbitrary without alignment to finite element mesh; (c) the stress recovery can be achieved inherently etc.

CHAPTER 7

FRACTURE ANALYSIS OF POROUS MEDIA

7.1 Introduction

In Chapter 7, the numerical analysis for the deformable porous media by using XCQ4 method is conducted and the feasibility of fracture mapping procedure in the context of XCQ4 is investigated to obtain the variant of displacement and pressure field in fractured porous solid. It is known that the dual continuum concept [Barenblatt et al., 1960] is made up of the dual porosity and dual permeability approaches. The dual porosity method considers that the porous matrix domain is discontinuous and flow inside the domain is reflected by the fractured network. The simulated fluid flow is directly influenced by fractured network connectivity and distribution. On the contrary, the dual permeability model assumes that the matrix domain is continuous and fluid flow distributes within both the matrix and fracture domains. And the fracture network connectivity is not necessary for the dual permeability method. An alternative method comparing with the dual continuum concept is the discrete fracture flow model approach [Tran et al., 2007; Lee et al., 1999]. Fractures are modelled inside the domain in a spatially explicit manner and are discretized with the matrix domain. In spite of the consideration of real fracture geometry and orientation in this approach, challenging mesh and more computational time results in the restriction to domains with low fracture density. However, the fracture mapping approach [Lamb et al., 2013] integrates the advantage of both the discrete and continuum approaches such as a) fracture geometry can be embedded in the simulation domain; b) elements intersected by facture are regarded as two overlapping parts of fracture and matrix domain. c) the related fracture porous material parameters are assigned with fracture elements. In particular, the fracture mapping method adopts transfer function proposed by [Barenblatt et al., 1960] to explain the interaction between the matrix and fracture domain.

7.2 Biot’s Theroy

The algorithm of the coupled displacement and water pressure behavior in porous media is introduced in [Biot, 1941]. The detailed formulation makes the material skeleton as a single elastic porous solid and combine its deformation to the laminar flow of the pore fluid through compressibility and continuity. This theme also is available for evaluating the fractured porous media containing discrete fractions with same solid compressibility and permeability. Accordingly, the basic knowledge from [Lewis et al., 1998] with respect to the porous media is introduced briefly.

7.2.1 Physical Mode

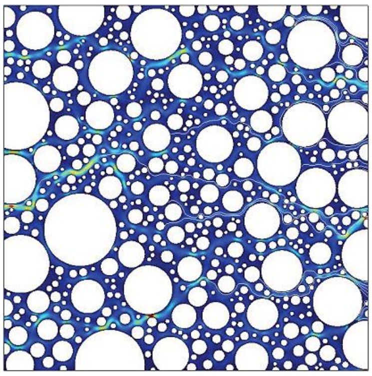

Fig. 7.1 Presence of different components.

The voids of the skeleton are filled partly with water and partly with moist air that is a mixture of dry air and water vapor as shown in Fig. 7.1. The degree of water saturation S_w is defined as the ration between the pore space filled with water and the total pore volume in a prescribed volume element (PVE). Hence the relationship is given as

$$S_w = \frac{dv^w}{dv^w + dv^g} \tag{7.1}$$

Here, define the superscript π as the generic phase and $\pi = w, g, s$ denotes water phase, gas phase and solid phase, respectively. The volume of the PVE domain is $\mathrm{d}v$, so thhe partial volumes of each phase is given as dv^w, dv^g and dv^s.

The expression of the degree of gas saturation S_g is

$$S_g = \frac{dv^g}{dv^w + dv^g} \tag{7.2}$$

and both degrees of saturation sum to one, i.e. $S_w + S_g = 1$.

The porosity is defined as the ratio between the volume of voids and the total volume of the (PVE)

$$n = \frac{dv^w + dv^g}{\mathrm{d}v} \tag{7.3}$$

Stress is defined as tension positive for the solid phase; pore pressure is defined as compressive positive for fluids. The water pressure P^w and the gas pressure P^g are related through the capillary pressure P^e:

$$P^g - P^w = P^e \tag{7.4}$$

The constitutive law of the solid phase is introduced in terms of the notion of effective stress:

$$\boldsymbol{\sigma}' = \boldsymbol{\sigma} + \mathbf{I}P^{av} \tag{7.5}$$

where $\boldsymbol{\sigma}$ is total stress tensor, $\mathbf{I}$ is the second-order unit tensor and P^{av} is the average pressure of both the water and air surrounding the grains. This equation reflects the main characteristics of the solid-phase constitutive relationship.

For the fluid phase, the stress tensor can be defined as

$$\boldsymbol{\sigma}^{\pi} = \boldsymbol{\tau}^{\pi} - \mathbf{I}P^{\pi} \tag{7.6}$$

where $\boldsymbol{\tau}^{\pi}$ is the shear stress.

Under the assumption that the shear stress $\boldsymbol{\tau}^{\pi}$ is negligible in fluids and based on the definition of averaged pressure P^{av} for fluid phase

$$P^{av} = S_g P^g + S_w P^w \tag{7.7}$$

Then, the stress tensor for fluid phase is comprised of two components: 1) the pore pressure effect; 2) the portion that deforms the solid skeleton, i.e., the effective stress

$$\boldsymbol{\sigma} = \boldsymbol{\sigma}' - \mathbf{I}P^{av} \tag{7.8}$$

where effective stress $\boldsymbol{\sigma}'$ for fluid phase is given by

$$\boldsymbol{\sigma}' = (1 - n)(\boldsymbol{\sigma}^{s} + \mathbf{I}P^{av}) \tag{7.9}$$

To extend the generality, a corrective term termed as Biot's constant has to be introduced to explain the deformability of the grains [Roscoe et al., 1963]. Hence, a more general expression of the effective stress is formulated as

$$\boldsymbol{\sigma}'' = \boldsymbol{\sigma} + \mathbf{I}\alpha\left(S_g P^g + S_w P^w\right) \tag{7.10}$$

where the corrective coefficient α will be explained in next section.

7.2.2 Constitutive Equations

The effective stress results in all relevant deformation of the solid skeleton. The constitutive relationship can be written as [Lewis et al., 1998]

$$d\boldsymbol{\sigma}' = \boldsymbol{D}_{\mathrm{T}}[(d\boldsymbol{\varepsilon} - d\boldsymbol{\varepsilon}^{c} - d\boldsymbol{\varepsilon}_{v}^{s} - d\boldsymbol{\varepsilon}^{0})] \tag{7.11}$$

where $d\boldsymbol{\sigma}'$ denotes the stress accountable for all deformations in addition to the grain compressibility. $d\boldsymbol{\varepsilon}$ is the total strain of the solid, $d\boldsymbol{\varepsilon}^{c}$ represents the creep strain and $d\boldsymbol{\varepsilon}^{0}$ stands for all other strains in the solid skeleton not directly dependent on effective stress. $\boldsymbol{D}_{\mathrm{T}}$ is the tangent constitutive tensor. $d\boldsymbol{\varepsilon}_{v}^{s}$ signifies the incremental form of a purely volumetric strain.

Considering a modified effective stress which allows for grain compression and Biot's constant α, Eq. (7.11) can be rewritten as

$$\begin{aligned} d\sigma_{ij} &= d\sigma''_{ij} - \left(1 - \frac{K_T}{K_S}\right)\delta_{ij} dP^{av} \\ &= d\sigma''_{ij} - \alpha\delta_{ij} dP^{av} \end{aligned} \tag{7.12}$$

where K_T and K_S is the bulk modulus of the skeleton and grain material, respectively.

7.2.3 Governing Equations

The Biot's theory accounts for the physical process of elastic deformation and fluid flow in porous media. The stress and strain tensors for two-dimensional domain can be written in Voigt notation as

$$\begin{aligned} \boldsymbol{\sigma} &= \left[\sigma_x, \sigma_y, \tau_{xy}\right]^{\mathrm{T}} \\ \boldsymbol{\varepsilon} &= \left[\varepsilon_x, \varepsilon_y, \gamma_{xy}\right]^{\mathrm{T}} \end{aligned} \tag{7.13}$$

A saturated soil or rock mass can be regarded as a two-phase deformable porous medium in which the pores are filled with a liquid. Thus the strong form of equilibrium equation is given by:

$$\nabla_s^T \cdot \boldsymbol{\sigma} + \rho \mathbf{g} = 0 \tag{7.14}$$

where $\boldsymbol{\sigma}$ is the total stress tensor, ρ is the averaged density of a multiphase system, $\mathbf{g}$ is gravity and ∇_s is the symmetric gradient operator matrix given by

$$\nabla_s = \begin{bmatrix} \frac{\partial}{\partial x} & 0 \\ 0 & \frac{\partial}{\partial y} \\ \frac{\partial}{\partial y} & \frac{\partial}{\partial x} \end{bmatrix} \tag{7.15}$$

The total stress of the system under the assumption that tension is positive can be written as

$$\boldsymbol{\sigma} = \boldsymbol{\sigma}'' - \alpha \mathbf{m} P^w \tag{7.16}$$

where $\boldsymbol{\sigma}''$ is the denotation of effective stress, P^w is the water pore pressure inside the porous media, $\mathbf{m} = [1\ 1\ 0]^T$ for two dimensional domain and α is the Biot's compressibility coefficient that is usually given as

$$\alpha = 1 - \frac{K_T}{K_S} \tag{7.17}$$

To obtain the governing equation, some basic physical quantities associated with the inward interaction between each phase are introduced. The Darcy's seepage velocity is

$$v_d = \frac{\mathbf{K}_m}{\mu_w}(-\nabla \cdot P^w + \rho \mathbf{g}) \tag{7.18}$$

Then the relationship between the pore flow through the domain and the reduction of the volume can be defined as

$$\nabla \cdot v_d = -\alpha \mathbf{m}^{\mathrm{T}} \frac{\partial \boldsymbol{\varepsilon}}{\partial t} \tag{7.19}$$

Another important variable quantity is the rate of change of grain volume resulted from the pressure changes within the domain and can be given as

$$\left(\frac{\alpha - n}{K_s} + \frac{n}{K_w}\right)\frac{\partial P^w}{\partial t} \tag{7.20}$$

where μ_w stands for the fluid viscosity, $\mathbf{K}_m$ and K_w is the material permeability and the bulk modulus of water, respectively.

Finally, through considering all three physical quantities, the general mass balance equation can be represented as [Lewis et al., 1998]

$$\nabla \cdot \left(\frac{\mathbf{K}_m}{\mu_w}(-\nabla \cdot P^w + \rho \mathbf{g})\right) + \alpha \mathbf{m}^{\mathrm{T}} \frac{\partial \boldsymbol{\varepsilon}}{\partial t} + \left(\frac{\alpha - n}{K_s} + \frac{n}{K_w}\right)\frac{\partial P^w}{\partial t} = 0 \tag{7.21}$$

7.2.4 Boundary Conditions

As shown in Fig. 7.2, boundary conditions for solid only comprise of the displacement and traction on the edge of domain. At $t = 0$, the initial conditions can be given as

$$\begin{aligned} \mathbf{u} &= \bar{\mathbf{u}} \quad \text{on } \Gamma_u \\ \boldsymbol{\sigma} \cdot \mathbf{n} &= \bar{\mathbf{t}} \quad \text{on } \Gamma_t \\ \boldsymbol{\sigma} \cdot \mathbf{n} &= 0 \quad \text{on } \Gamma_c \end{aligned} \tag{7.22}$$

where $\bar{\mathbf{u}}$ denotes the prescribed displacement on boundary Γ_u, $\boldsymbol{\sigma}$ is the total stress computed by Eq. (7.16) and $\bar{\mathbf{t}}$ is the traction vector on boundary Γ_t. Particularly, the traction is free on the both sides of the crack surface.

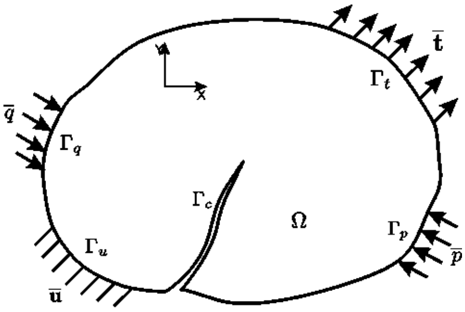

Fig. 7.2 Body containing a crack.

Boundary conditions for the fluid flow in the porous medium can be written as:

$$
\begin{aligned}
p &= \bar{p} \quad \text{on } \Gamma_p \\
\rho_w \frac{\mathbf{K}_m}{\mu_w} (-\nabla \cdot P^w + \rho \mathbf{g})^{\mathrm{T}} \cdot \mathbf{n} &= \bar{q} \ \text{ on } \Gamma_q
\end{aligned}
\tag{7.23}
$$

where $\bar{p}$ is the prescribed pressure on the boundary Γ_p and $\bar{q}$ is the volumetric flux on the boundary Γ_q. These boundary conditions are Dirichlet and Neumann boundary conditions. The Dirichlet boundary condition indicates the displacement and pressure at the matrix domain boundary, and the Neumann boundary condition specify the stress and flow rate at the domain boundary.

The initial conditions can be obtained by the initial values of pore pressure and displacement. If the pore pressure reaches equilibrium at the initial time, there is no pressure gradient anywhere.

7.3 Numerical Implementation

Numerical solution is introduced in this section using the general case of fluid-solid interaction, which is isothermal consolidation in small strain assumption. The benchmark example associated with water pressure distribution in fractured porous media and the coupled deformation of solid phase and flow of pore fluid using the transfer function to accounts for the interaction of the fluid flow interaction between the matrix and the fracture are considered. The analysis is conducted for the case of saturated, one-phase flow problems in deformable porous media.

7.3.1 Approximation of Displacement and Water Pressure

As introduced in chapter 2, two level set functions are considered here to describe the crack face in porous media, i.e. normal and tangent level sets. The level sets approach in XCQ4 can represent crack in terms of the signed functions, which makes the crack modelling unnecessary to comply with the background mesh. By virtue of this advantage, XCQ4 method becomes more capable of dealing with complicated geometry of cracks. Therefore the general form of XCQ4 approximation can be given as

$$\begin{aligned}\mathbf{u}^h(\mathbf{x}) = \sum_{i\in W_s} \tilde{N}_i(\mathbf{x})\mathbf{u}_i + \sum_{j\in W_c} \tilde{N}_j(\mathbf{x})\left[H(\mathbf{x}) - H(\mathbf{x}_j)\right]\mathbf{a}_j \\ + \sum_{k\in W_t} \tilde{N}_k(\mathbf{x})\sum_{\alpha=1}^{4}\left[F^{\alpha}(\mathbf{x}) - F^{\alpha}(\mathbf{x}_k)\right]\mathbf{b}_k^{\alpha}\end{aligned} \tag{7.24}$$

where $\widetilde{N}_i(\mathbf{x})$ represents CQ4 shape function for node i. Heaviside and asymptotic enrichment functions are adopted to enrich the discontinuity. Other related parameters can refer to the interpretation in section 3.5.

For permeable natural fracture, assume that the pressure field is continuous at the fracture surface, while the flow rate, i.e. the derivative of pressure is discontinuous. For a node associated with a split element that is intersected by the discontinuity completely, the absolute singed distance function is selected as enrichment function

$$F(\mathbf{x}) = |\phi(\mathbf{x})| \tag{7.25}$$

For the node in the crack tip element which contains the crack tip, the branch function is considered as asymptotic enrichment function

$$B_\alpha(\mathbf{x})|_{\alpha=1,2,3} = \left[rcos\frac{\theta}{2},\quad r^2cos\frac{\theta}{2},\quad \sqrt{r}os\frac{\theta}{2}\right] \tag{7.26}$$

in which (r,θ) is the polar coordinate system.

Based on these two sets of enrichment functions, the pressure approximation for a single fracture can be written as

$$\begin{aligned} p^h(\mathbf{x}) &= \sum_{i\in W_s} \tilde{N}_i(\mathbf{x}) p_i + \sum_{j\in W_c} \tilde{N}_j(\mathbf{x})\left[F(\mathbf{x}) - F(\mathbf{x}_j)\right]\mathbf{a}_j \\ &+ \sum_{k\in W_t} \tilde{N}_k(\mathbf{x}) \sum_{\alpha=1}^{3}\left[B_\alpha(\mathbf{x}) - B_\alpha(\mathbf{x}_k)\right]\mathbf{b}_k^\alpha \end{aligned} \tag{7.27}$$

where p_i is the nodal value of pore pressure in the porous media.

7.3.2 Transfer Function

A fractured porous media such as rock includes pores and permeable blocks which are separated with each other by a set of fractures. The dimensions of the block is different based on the generated fracture within the rock and the widths of the blocks are quite greater than the volume of the pores. Therefore, the permeability of the fracture system indeed exceeds the one of the pores system in the individual block. If the system fracture is well developed, the motion of the liquid in fractured porous media can be investigated by means of a non-steady-state model which accounts for the average pressure of the liquid in the fracture and the pressure in the pores [Barenblatt et al., 1960].

A prominent feature of the model is the transfer of liquid between the blocks and the fracture. The process of the liquid’s transfer motion from the pores and the blocks is under a smooth change of pressure, thus, it is assumed that this pressure is quasi-stationary. Here one transfer function which describes the fluid flow interaction between the matrix and fracture domain is introduced as shown in Fig. 7.3.

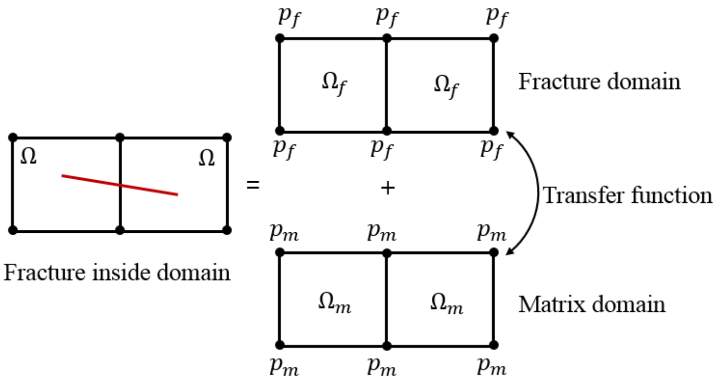

Fig. 7.3 The role of transfer function in matrix and fracture domain.

Assume the function is proportional to the difference between the matrix pore pressure P^m and the fracture fluid pressure P^f, so the relationship based on the quasi steady-state function can be given as

$$T=\frac{\bar{r}\mathbf{K}_f}{\mu_w}(P^m-P^f) \tag{7.28}$$

where T represents the transfer function, $\mathbf{K}_f$ is the fracture permeability and $\bar{r}$ denotes a shape factor associated with the width and geoemtry of the existing fracture as explained in [Barenblatt et al., 1960]. Because the width of the fracture is not considered in this approach, $\bar{r}$ is not required here.

7.4 Spatial Discretization

Based on the concept of transfer function and the Galerkin-based finite element method, assume that the effect of gravity is ignored and the Biot's coefficient $\alpha=1$, then the continuity equations can be rewritten as [Lamb et al., 2013]

$$\nabla\cdot\left(-\frac{\mathbf{K}_m}{\mu_w}\nabla\cdot P^w\right)+\frac{\mathbf{K}_f}{\mu_w}(P^m-P^f)+\mathbf{m}^{\mathrm{T}}\frac{\partial\boldsymbol{\varepsilon}}{\partial t}+\left(\frac{1-n}{K_s}+\frac{n}{K_w}\right)\frac{\partial P^w}{\partial t}=0 \tag{7.29}$$

Particularly, the continuity equation for porous matrix can be separated from Eq. (7.29) as

$$\nabla\cdot\left(-\frac{\mathbf{K}_m}{\mu_w}\nabla\cdot P^m\right)+\frac{\mathbf{K}_f}{\mu_w}(P^m-P^f)+\mathbf{m}^{\mathrm{T}}\frac{\partial\boldsymbol{\varepsilon}}{\partial t}+\left(\frac{1-n}{K_s}+\frac{n}{K_w}\right)\frac{\partial P^m}{\partial t}=0 \tag{7.30}$$

for the fracture part, the continuity equation can be given as

$$\nabla \cdot \left(-\frac{\mathbf{K}_f}{\mu_w}\nabla \cdot P^f\right) + \frac{\mathbf{K}_f}{\mu_w}(P^m - P^f) + \frac{n}{K_w}\frac{\partial P^f}{\partial t} = 0 \tag{7.31}$$

In the following, consider the basic variables of the displacements $\mathbf{u}$ and pore water pressure P^w, the approximation can be obtained as

$$\begin{aligned} \mathbf{u} &= \widetilde{N}_u \bar{\mathbf{u}} \\ P^w &= \widetilde{N}_p \bar{\mathbf{P}}^w \end{aligned} \tag{7.32}$$

where $\bar{\mathbf{u}}$ and $\bar{\mathbf{P}}^w$ are the vectors of the nodal values of the unknowns. $\widetilde{N}_u$ and $\widetilde{N}_p$ is the CQ4 shape function for the displacement and pressure field, respectively.

Take into account Eq. (7.16) and Eq. (7.29), and apply the integral form:

$$\begin{aligned} \int_\Omega \mathbf{B}^{\mathrm{T}} \boldsymbol{\sigma}'' \, d\Omega - \mathbf{Q}\bar{\mathbf{P}}^w &= \mathbf{f}^u \\ \mathbf{H}\bar{\mathbf{P}}^w + \mathbf{H}_T(\bar{\mathbf{P}}^m - \bar{\mathbf{P}}^f) + \mathbf{Q}^{\mathrm{T}}\frac{\partial \bar{\mathbf{u}}}{\partial t} + \mathbf{S}\frac{\partial \bar{\mathbf{P}}^w}{\partial t} &= \mathbf{f}^p \end{aligned} \tag{7.33}$$

where $\mathbf{B}$ is the strain operator, $\mathbf{Q}$ is the coupling matrix, $\mathbf{H}$ is the permeability matrix, $\mathbf{H}_T$ is the transfer permeability matrix and $\mathbf{S}$ is the compressibility matrix. $\mathbf{f}^u$ and $\mathbf{f}^p$ is the external boundary condition on Γ_u and Γ_p.

7.5 Discretization in Time

For the issue, the finite differences in time are adopted for the solution of the initial value problem. This approach provides an identical system of equations achieved with the weighted residual method in time with point collocation.

Thus, the spatial discretization mechanism can be written as

$$\mathbf{A}\frac{d\mathbf{X}}{dt} + \mathbf{B}\mathbf{X} = \mathbf{C} \tag{7.34}$$

Then, applying an implicit time discretization approach:

$$\begin{aligned} \left(\frac{d\mathbf{X}}{dt}\right)_{n+\theta} &= \frac{\mathbf{X}_{n+1} - \mathbf{X}_n}{\Delta t} \\ \mathbf{X}_{n+\theta} &= (1-\theta)\mathbf{X}_n + \theta \mathbf{X}_{n+1} \end{aligned} \tag{7.35}$$

Based on the Eq. (7.34) and Eq. (7.35) at time $t_{n+\theta}$ can be given as

$$(\mathbf{B}+\mathbf{A}\Delta t\theta)\mathbf{X}_{n+1}=\big(\mathbf{B}-\mathbf{A}\Delta t(1-\theta)\big)\mathbf{X}_n+\mathbf{C}\Delta t \tag{7.36}$$

where

$$\mathbf{A}=\begin{bmatrix}0&0&0&0&0\\0&0&0&0&0\\0&0&0&0&0\\0&0&0&\mathbf{H}_m+\mathbf{H}_T&-\mathbf{H}_T\\0&0&0&-\mathbf{H}_T&\mathbf{H}_f+\mathbf{H}_T\end{bmatrix}$$

$$\mathbf{B}=\begin{bmatrix}\mathbf{K}^{uu}&\mathbf{K}^{ua}&\mathbf{K}^{ub}&-\mathbf{Q}_u&0\\\mathbf{K}^{au}&\mathbf{K}^{aa}&\mathbf{K}^{ab}&-\mathbf{Q}_a&0\\\mathbf{K}^{bu}&\mathbf{K}^{ba}&\mathbf{K}^{bb}&-\mathbf{Q}_b&0\\\mathbf{Q}_u^{\mathrm{T}}&\mathbf{Q}_a^{\mathrm{T}}&\mathbf{Q}_b^{\mathrm{T}}&\mathbf{S}_m&0\\0&0&0&0&\mathbf{S}_f\end{bmatrix} \tag{7.37}$$

$$\mathbf{C}=\begin{bmatrix}d\mathbf{f}^u\\d\mathbf{f}^a\\d\mathbf{f}^b\\\mathbf{f}^p\\0\end{bmatrix}$$

After some simple manipulations, the final discrete equation can be given as

$$\begin{bmatrix}\mathbf{K}^{uu}&\mathbf{K}^{ua}&\mathbf{K}^{ub}&-\mathbf{Q}_u&0\\\mathbf{K}^{au}&\mathbf{K}^{aa}&\mathbf{K}^{ab}&-\mathbf{Q}_a&0\\\mathbf{K}^{bu}&\mathbf{K}^{ba}&\mathbf{K}^{bb}&-\mathbf{Q}_b&0\\\mathbf{Q}_u^{\mathrm{T}}&\mathbf{Q}_a^{\mathrm{T}}&\mathbf{Q}_b^{\mathrm{T}}&\Delta t\theta(\mathbf{H}_m+\mathbf{H}_T)+\mathbf{S}_m&-\mathbf{H}_T\Delta t\theta\\0&0&0&-\mathbf{H}_T\Delta t\theta&\big(\mathbf{H}_f+\mathbf{H}_T\big)\Delta t\theta+\mathbf{S}_f\end{bmatrix}\begin{bmatrix}u\\a\\b\\\bar{P}^m\\\bar{P}^f\end{bmatrix}_{n+1}$$

$$=\begin{bmatrix}\mathbf{K}^{uu}&\mathbf{K}^{ua}&\mathbf{K}^{ub}&-\mathbf{Q}_u&0\\\mathbf{K}^{au}&\mathbf{K}^{aa}&\mathbf{K}^{ab}&-\mathbf{Q}_a&0\\\mathbf{K}^{bu}&\mathbf{K}^{ba}&\mathbf{K}^{bb}&-\mathbf{Q}_b&0\\\mathbf{Q}_u^{\mathrm{T}}&\mathbf{Q}_a^{\mathrm{T}}&\mathbf{Q}_b^{\mathrm{T}}&\mathbf{S}_m-\Delta t(1-\theta)(\mathbf{H}_m+\mathbf{H}_T)&\mathbf{H}_T\Delta t(1-\theta)\\0&0&0&\mathbf{H}_T\Delta t(1-\theta)&\mathbf{S}_f-\Delta t(1-\theta)\big(\mathbf{H}_f+\mathbf{H}_T\big)\end{bmatrix}\begin{bmatrix}u\\a\\b\\\bar{P}^m\\\bar{P}^f\end{bmatrix}_n$$

$$+\begin{bmatrix}d\mathbf{f}^u\\d\mathbf{f}^a\\d\mathbf{f}^b\\\mathbf{f}^p\\0\end{bmatrix}\Delta t \tag{7.38}$$

where

$$\mathbf{K}^{rs}=\int_{\mathbf{\Omega}}(\mathbf{B}^{r})^{\mathrm{T}}\mathbf{m}\mathbf{B}^{s}d\Omega_{e}\quad r=\boldsymbol{u},\boldsymbol{a},\mathbf{b}$$

$$\mathbf{Q}_{r}=\int_{\mathbf{\Omega}}(\mathbf{B}^{r})^{\mathrm{T}}\mathbf{m}N_{p}d\Omega_{e}\quad r=\boldsymbol{u},\boldsymbol{a},\mathbf{b}$$

$$\mathbf{H}_{r}=\int_{\mathbf{\Omega}}\left(\nabla\tilde{N}_{p}\right)^{\mathrm{T}}\frac{\mathbf{K}_{r}}{\mu_{w}}\nabla\tilde{N}_{p}d\Omega_{e}\quad r=m,f$$

$$\mathbf{H}_{T}=\int_{\mathbf{\Omega}}\left(\tilde{N}_{p}\right)^{\mathrm{T}}\frac{\mathbf{K}_{f}}{\mu_{w}}\tilde{N}_{p}d\Omega_{e}$$

$$\mathbf{S}_{r}=\int_{\mathbf{\Omega}}\left(\tilde{N}_{p}\right)^{\mathrm{T}}\frac{n^{r}}{\mathbf{K}_{w}}\tilde{N}_{p}d\Omega_{e}\quad r=m,f$$

$$\mathbf{f}^{u}=-\int_{\mathbf{\Gamma}}\left(\tilde{N}_{p}\right)^{\mathrm{T}}\bar{\mathbf{t}}d\Gamma$$

$$\mathbf{f}^{a}=-\int_{\mathbf{\Gamma}}\left(H(\mathbf{x})-H(\mathbf{x}_{i})\right)\left(\tilde{N}_{p}\right)^{\mathrm{T}}\bar{\mathbf{t}}d\Gamma$$

$$\mathbf{f}^{b}=-\int_{\mathbf{\Gamma}}\left(F_{\alpha}(\mathbf{x})-F_{\alpha}(\mathbf{x}_{i})\right)\left(\tilde{N}_{p}\right)^{\mathrm{T}}\bar{\mathbf{t}}d\Gamma\quad\alpha=1,2,3,4$$

$$\mathbf{f}^{p}=\int_{\mathbf{\Omega}}\left(\tilde{N}_{p}\right)^{\mathrm{T}}\frac{\mathbf{K}_{m}}{\mu_{w}}\rho_{w}\mathbf{g}d\Omega_{e}-\int_{\mathbf{\Gamma}_{q}}\left(\tilde{N}_{p}\right)^{\mathrm{T}}\frac{q^{w}}{\rho_{w}}d\Gamma\tag{7.39}$$

$$\mathbf{B}^{u}=\nabla_{s}\tilde{N}_{u}=\begin{bmatrix}\frac{\partial}{\partial x}&0\\0&\frac{\partial}{\partial y}\\\frac{\partial}{\partial y}&\frac{\partial}{\partial x}\end{bmatrix}\tilde{N}_{u}$$

$$\mathbf{B}^{a}=\nabla_{s}\tilde{N}_{u}\left(H(\mathbf{x})-H(\mathbf{x}_{i})\right)=\begin{bmatrix}\frac{\partial}{\partial x}&0\\0&\frac{\partial}{\partial y}\\\frac{\partial}{\partial y}&\frac{\partial}{\partial x}\end{bmatrix}\tilde{N}_{u}\left(H(\mathbf{x})-H(\mathbf{x}_{i})\right)$$

$$\mathbf{B}^{b}=\nabla_{s}\tilde{N}_{u}\left(F_{\alpha}(\mathbf{x})-F_{\alpha}(\mathbf{x}_{i})\right)=\begin{bmatrix}\frac{\partial}{\partial x}&0\\0&\frac{\partial}{\partial y}\\\frac{\partial}{\partial y}&\frac{\partial}{\partial x}\end{bmatrix}\tilde{N}_{u}\left(F_{\alpha}(\mathbf{x})-F_{\alpha}(\mathbf{x}_{i})\right)\quad\alpha=1,2,3,4$$

$$\nabla \tilde{N}_p = \begin{bmatrix} \dfrac{\partial}{\partial x} \\ \dfrac{\partial}{\partial y} \end{bmatrix} \tilde{N}_p$$

7.6 Numerical Simulation

To verify the proposed XCQ4 formulation and the effect of sealed fractures on flow behavior in the fractured porous media, one example with a single crack is considered. In Section 7.6.1, the fluid flow in the porous media and the fluid exchange between the fracture and the porous medium surrounding the fracture is simulated. In section 7.6.2, the coupled hydro-mechanical problem associated with flow in cracked deformable porous media is studied to numerically reflect the motion of displacement and pressure field.

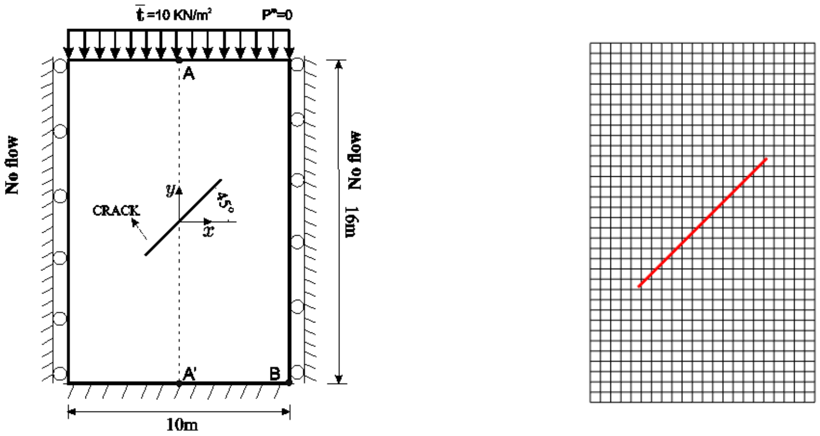

Fig. 7.4 Schematic geometry of single fracture model.

For a two-dimensional fractured domain with an independent fissure shown in Fig. 7.4, the available numerical results of discrete fracture mode (DFM) and fracture mapping with mesh free (FM-MF) can be found in [Lamb et al., 2013], so the correctness of the proposed XCQ4 approach is verified through comparing with reference solution. The prescribed domain has an area of 10m x 16m, and the length of center fracture is 8m with an inclined angle 45^o. Except the top side, other sides are supposed to be undrained. The horizontal displacement of lateral boundaries of the specimen are restricted and the bottom is fixed fully. Static load is applied on the top side and maintained throughout the duration of the simulation. The input parameters are listed in Table 7.1

Table 7.1 Input material parameters

Parameter	Definition	Magnitude	Unites
E	Young's modulus	40	MPa
υ	Poisson's ratio	0.3	-
n^m	Matrix porosity	0.1	-
n^f	Fracture porosity	0.05	-
$\mathbf{K}_m/\mu_w$	Matrix mobility	1x10^{-6}	m^{3}s/kg
$\mathbf{K}_f/\mu_w$	Fracture mobility	1x10^{-1}	m^{3}s/kg

7.6.1 The Comparison in Flow Pressure Field

In this case, there is no consideration of the external load and the bottom initial pressure value is applied as $P = 286$ KPa to obtain the pressure distribution to compare with reference solution from [Fei et al., 2015]. Fig. 7.5 shows the numerical results of the pressure field in the fractured porous media by FEM (5856 elements), XQ4 (104 elements), XCQ4 (104 elements) and XCQ4 (770 elements). It can be indicated that the pressure field derived from XCQ4 is smoother than that of XQ4 under the same coarse mesh. Accordingly the specific values of vertical nodes in the center of the specimen along $A - A'$ are collected in Fig. 7.4 to explain the longitudinal variation of the pressure profile. Both qualitatively identical results turned out that XCQ4 method is one reliable and accurate method for analyzing the fractured porous media.

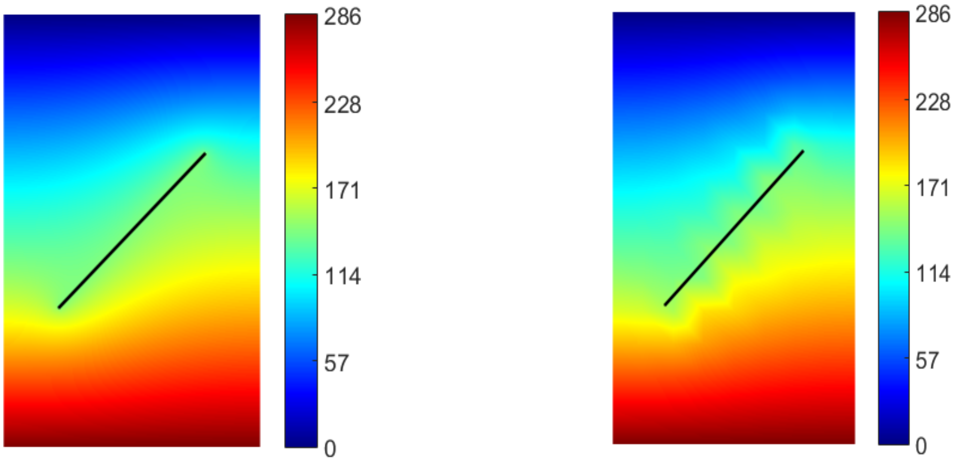

FEM (5856 elements)

XQ4 (104 elements)

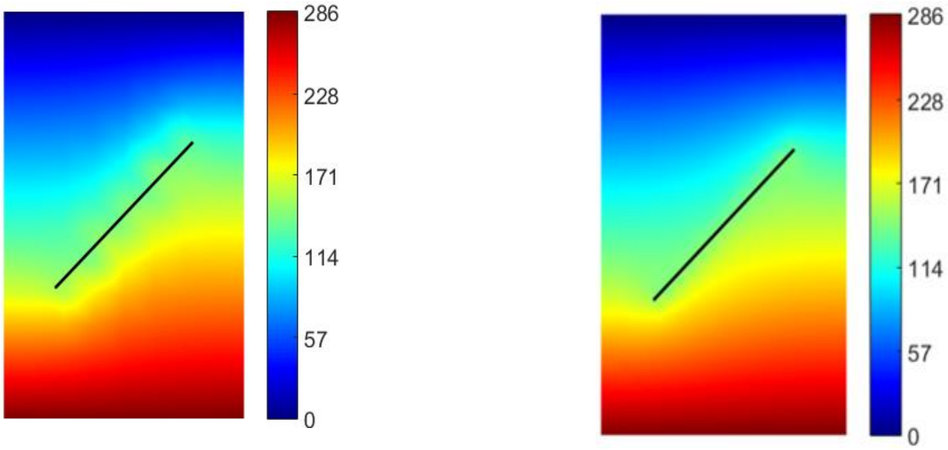

XCQ4 (104 elements)

XCQ4 (770 elements)

Fig. 7.5 The numerical results of pore pressure obtained by different methods.

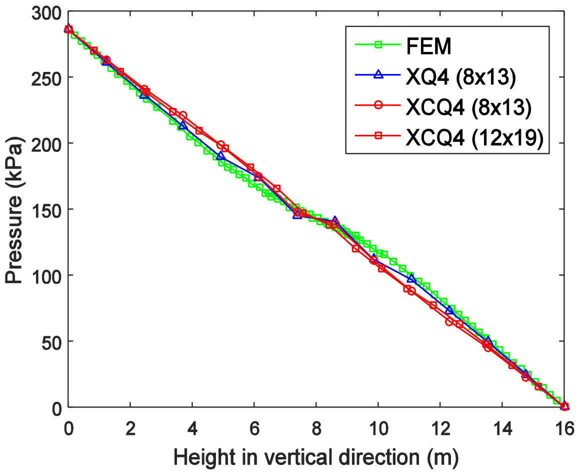

Fig. 7.6 Vertical nodal values of flow pressure extracted from the center of the domain by different methods.

In addition, the time history of the fluid pressure is plotted in Fig 7.7 to visualize the process of water change over the fractured porous domain. It can be observed that the water pressure tend to be stable with the increasing of the step.

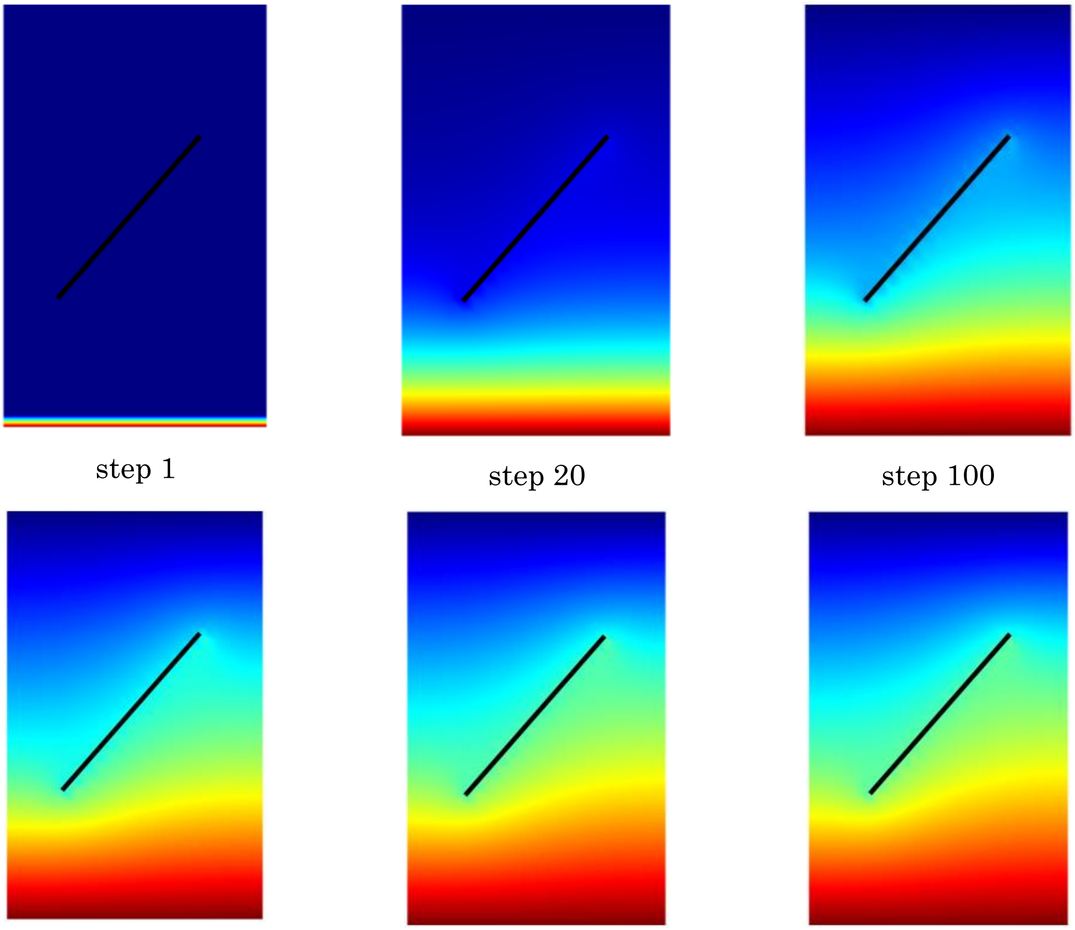
step 1 step 20 step 100

step 500 step 1000 step 1500

Fig. 7.7 Time history of the fluid pressure.

7.6.2 The Comparison in Displacement

In this case, the XCQ4 method is coupled with fracture mapping procedure to simulate the fluid flow in the deformable porous media. The domain is fully saturated and allowed to freely drain at the top, that is, excess pore water pressure is equal to zero. Also the static loading $\bar{t} = 10\ \mathrm{KN/m^2}$ is applied at the top boundary of the specimen. Here, the variation of the normalized pore pressure at point B located at the right corner of the bottom boundary is plotted as shown in Fig. 7.8. It is clearly shown that the time history of pore pressure obtained by the

XCQ4 method is similar with the reference solution from [Lamb et al., 2013]. During the initial stage of the pore pressure dissipation, it can be found out that an increasing tendency occurred on the pore pressure variation. This phenomenon of the initial increase then decrease in excess pore pressure can be regarded as Mandel-Cryer effect [Mandel et al., 1953; Cryer et al., 1963], that is to say, the initial augment of the pore pressure takes place since the fluid at the top region of the domain dissipate rapidly, which causes an increase of pore pressure above the initial pressure value at the bottom region of the domain.

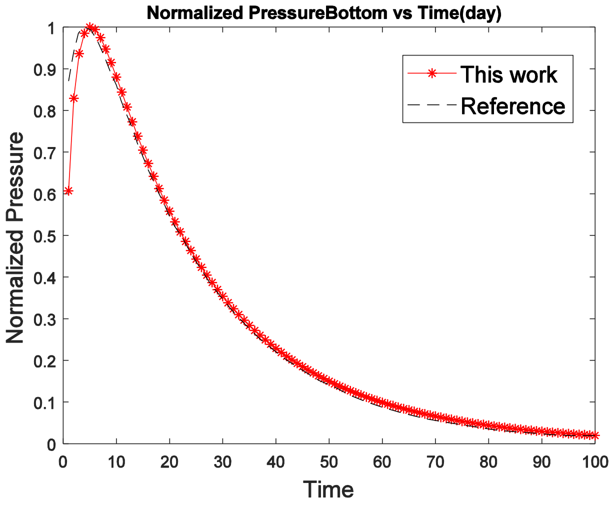

Fig. 7.8 Body containing a crack.

7.7 Summary

In this section, the XCQ4 is used to simulate the fluid flow in saturated porous media without requiring the discretization to comply with the geometry of the sealed fractures. Both absolute signed distance function and new proposed asymptotic crack tip enrichment function which is continuous in the interpolation function while its derivative is discontinuous. These enrichment functions can accurately capture the fracture behavior of fluid flow in the vicinity of permeable natural fracture. Furthermore, a mathematical description named transfer function is coupled with XCQ4 to reflect the fluid flow interaction between the matrix and fracture domain and simulate the fluid-solid coupling problems in terms of Biot’s theory.

Upon the validation of numerical experiment, it is confirmed that the proposed XCQ4 method is both stable and reliable for solving the issue related to fluid pressure in fractured porous media and the combination of XCQ4 method and fracture mapping procedure has the ability to accurately describe the coupled hydro-mechanical behavior in a domain containing sealed fracture.

CHAPTER 8

CONCLUSIONS AND FUTURE WORK

8.1 Conclusions

In this study, the CQ4 element enhanced by enrichments is further developed for handling the solutions of non-smooth problems like cracks. The new element (XCQ4) can thus eliminate the difficulty of meshing issue, the crack geometry is independent of finite element mesh, and more importantly the post-processing for stress recovery is no longer required. By integrating the interaction integral in terms of J-domain, the fracture parameters are estimated, and adopt the maximum hoop stress criterion to determine the direction of growing crack. To extend the validation, the proposed XCQ4 has been developed for modelling dynamic fracture behavior of isotropic and anisotropic material. Coupling with the transfer function, the XCQ4 approach is applied for demonstrating the fluid pore pressure and displacement filed in the fractured deformable porous media. Several representative benchmark problems associated with static SIFs analysis, crack growth, dynamic fracture response and fluid flow motion in 2D elastic solids with different material property are considered to show the accuracy and performance of the present approach. In the following, the achievements and conclusions of this work can be briefly summarized as:

(1) Static analysis with respect to evaluation of SIFs calculation.

The extended CQ4 element (XCQ4), which particularly suits for crack modeling, is used to analyze the stress intensity factors of several linear elastic fracture mechanic problems in 2D space. The main goal in this study by how accurately the SIFs can be computed with the new XCQ4 element. In each case of the study, the SIFs and their convergence rates under applied loads are estimated and they have been found to agree well with the corresponding analytical results, the common XQ4, or with the literature solutions derived from other numerical methods. Generally, the present numerical results reveal a good performance of the XCQ4 element as it offers higher accuracy than that computed with the common element.

(2) Prediction of the crack growth path investigated using XCQ4.

For solving crack propagation issue, several examples are considered and the numerical results have been found closely resemble the related reference solution in literatures solved by numerical or experimental techniques. According to the present work, XCQ4 yields a good performance as it offers higher accuracy with respect to SIFs compared with that calculated by XQ4 method. For visualizing the discrepancy of stress distribution around crack tip obtained by different approaches, the normal stress contour plots are illustrated in some cases. Through the comparison of stress contour plots it is evidently detected that the XCQ4 method is outstanding for recovering the nodal stresses without requiring any post-processing.

(3) Estimation of computational time in assembling process of global stiffness matrix.

In this study the computational time of the new XCQ4 element in the procedure of assembling global stiffness matrix is investigated. Since the solver time is relevant with the bandwidth of the global stiffness matrix and the bandwidth of XCQ4 is larger than that of XQ4, hence the computational time cost by XCQ4 is nearly 2.5 times as that of XQ4. However the improvement of accuracy about the SIFs is satisfactory. Basically, the computational time of the whole procedure based on the CIP element gains a higher cost as compared to that computed with the standard element. The main reason induced the higher cost of the new element almost lies in the CIP procedure, but one must pay attention to its high accuracy and the need for not using a post-processing of any smoothing operation.

(4) Exploration of coupling XCQ4 with ramp function.

Two types of ramp function in this work are assessed as an alternative crack tip enrichment function in conjunction with the proposed XCQ4 and XQ4. Stress intensity factors computed by different combinations between the ramp functions and original numerical methods are analyzed. The results indicate that the ramp functions along with Heaviside function are capable of capturing the discontinuity inside the crack tip element as same as the classical asymptotic fourfold functions. The predicted crack growth paths obtained by the new enrichment schemes of ramp functions are in a good agreement with the reference solution. In particular, the computational time of different numerical schemes involving ramp functions is investigated. Because only two degrees of freedom are demanded at each crack tip enriched node in 2D solids issues, the cost of computational time will be reduced prominently for some cases adopting finer mesh or small incremental crack size.

(5) Analysis of dynamic fracture behavior in isotropic and anisotropic solids.

Upon the application of Newmark time integration theme in orthotropic material, the DSIFs history are analyzed by XCQ4 for single and mixed mode fracture problems. Furthermore, the sensitivity of the orientations of the orthotropy on the behavior of the DSIFs history is investigated to validate the feasibility of XCQ4 with respect to intricate material properties. Based on the numerical investigation in isotropic and orthotropic solids, it is concluded that XCQ4 can offer satisfactory capability on the solution of the DSIFs in cracked isotropic and anisotropic solids. Moreover different loading conditions and shape complexity are explored to take an insight look of DSIFs in special and complicated cases. Eventually, outstanding performance of XCQ4 method for reporting dynamic fracture response in isotropic and anisotropic media make us confident to implement next further research.

(6) Investigation on the fluid flow in saturated porous media containing sealed crack.

The coupled deformation and fluid flow in fractured porous media based on Biot’s theory has been simulated by the present XCQ4 approach. Through introducing the transfer function that mathematically demonstrates the flow interaction between the porous matrix and existing fracture, the superposition of the two domains containing matrix and fracture element is considered. Through numerical validation, it can be proven that present approach has ability to accurately capture the fluid flow and deformation in porous media without the need to embed the fracture mesh within the domain. Moreover, XCQ4 method coupling with fracture mapping procedure performs well to simulate the hydro-mechanical behavior in the fractured porous media.

8.2 Recommendations and Future Work

This research shall be continued in the following aspects:

a. Based on the achievements of the higher accurate approximation of physical fields and smooth gradient fields which are continuous across element boundary for the two-dimensional fracture problems, develop a new element using the concept of consecutive-interpolation procedure (CIP) to analyze the three-dimensional (3-D) linear solids and composite structures.

b. Improve the algorithm of calculating the consecutive-interpolation shape function $\widetilde{N}_f$ to reduce the cost of computational time for assembling the global stiffness matrix. The procedure of weight function w_e to average the derivative of $\widetilde{N}_f$ has already been modified in this study by alleviating the iteration of detecting the neighboring element area.

c. To further develop the application of XCQ4 approach in simulating the dynamic fracture with respect to moving crack and mixed mode crack. Since the accuracy of computed stress intensity factors has been elevated, the improved dynamic crack path can be obtained possibly. And the form explicit central difference method and the critical time step for the issue of dynamic crack growth should be considered.

d. The XCQ4 approach should be used for the discrete approximation of the partial differential equations governing the two-phase issue of simulating water and air flow in deformable porous media with fully or partially saturated conditions. In this problem, the pressure of water and of air and the displacement of the solid skeleton are assumed as the free variables.

e. The fracture analysis for the advanced materials using XCQ4 approach is worth recommending. Like, functionally graded material is one advanced composite with smoothing variation in the mechanical and thermal properties. Piezoelectric material is suitable for medical imaging and non-destructive testing, etc. Based on the advantages of XCQ4, the computational efforts for analyzing the fracture behavior in advanced materials may be alleviated.

REFERENCES

Agnantiaris, J.P., Polyzos, D. and Beskos, D.E. (1996) Some studies on dual reciprocity BEM for elastodynamics. *Computational Mechanics*, **17**, 270-277.

Albuquerque, E.L., Sollero, P. and Aliabadi, M.H. (2004) Dual boundary element method for anisotropic dynamic fracture mechanics, *Int. J. Numer. Methods Eng.*, **59**, 1187-1205.

Asadpoure, A., Mohammadi, S. and Vafai, A. (2006) Crack analysis in orthotropic media using the extended finite element method, *Thin Wall Struct.*, **44**, 1031-1038.

Asadpoure, A. and Mohammadi, S. (2007) Developing new enrichment functions for crack simulation in orthotropic media by the extended finite element method, *Int. J. Numer. Methods Eng.*, **69**, 2150-2172.

Ayatollahi, M.R. and Akhavan-Safar, A. (2015) Failure load prediction of single lap adhesive joints based on a new linear elastic criterion. *Theor. Appl. Fract. Mech.*, 80, 210-217.

Azocar, D., Elgueta, M. and Rivara, M.C. (2010) Automatic LEFM crack propagation method based on local lepp-delaunay mesh refinement. *Adv Eng Softw.*, **41**, 111-119.

Babuska, I. and Melenk, J.M. (1997) The partition of unity method. *Int. J. Numer. Meth. Eng.*, **40**,727-58.

Barati, E. and Azimi, M. (2016) Use of J-integral for prediction of critical fracture load in plates with U-notches under mixed mode loading. *Theor. Appl. Fract. Mech.*, **82**, 51-58.

Barenblatt, G.I., Zheltov, I.P. and Kochina I.N. (1960) Basic concepts in the theory of seepage of homogeneous liquids in fissured rocks [strata]. *Journal of Applied Mathematics and Mechanics*, **24**(5), 1286-1303.

Bayesteh, H., Afshar, A. and Mohammdi, S. (2015) Thermo-mechanical fracture study of inhomogeneous cracked solids by the extended isogeometric analysis method. *Eur. J. Mech. A. Solids.*, **51**, 123-139.

Belytschko, T. and Black, T. (1999) Elastic crack growth in finite elements with minimal remeshing. *Int. J. Numer. Meth. Engng.*, **45**, 601-620.

Belytschko, T., Chen, H., Xu, J. and Zi, G. (2003) Dynamic crack propagation based on loss of hyperbolicity and a new discontinuous enrichment. *Int. J. Numer. Meth. Eng.*, **58**,1873-1905.

Bechet, E., Minnebo, H., Moës, N. and Burgardt, B. (2005) Improved implementation and robustness study of the X-FEM for stress analysis around cracks. *Int. J. Numer. Meth. Eng.*, **64**, 1033-1056.

Bhardwaj, G., Singh, I.V., Mishra, B.K. and Bui, Q.T. (2015) Numerical simulation of functionally graded cracked plates using NUBRS based XIGA under different loads and boundary conditions. *Compos. Struct.*, **126**, 347-359.

Biot, M.A. (1941) General theory of three-dimensional consolidation. *Journal of Applied Physics*, **12**(2), 155-164.

Bittencourt, T.N., Wawrzynek, P.A. and Ingraffea, A.R. (1996) Quasi-automatic simulation of crack propagation for 2d LEFM problems. *Eng. Fract. Mech.*, **55**, 321-334.

Budyn, E., Zi, G., Moës, N. and Belytschko, T. (2004) A method for multiple crack growth in brittle materials without remeshing. *International Journal for Numerical Methods in Engineering*, **61**, 1741-1770.

Bui, Q.T. and Zhang, Ch. (2012) Extended finite element simulation of stationary dynamic cracks in piezoelectric solids under impact loading. *Comput. Mater. Sci.*, **62**,243-257.

Bui, Q.T. and Zhang, C.Z. (2013) Analysis of generalized dynamic intensity factors of cracked magnetoelectroelastic solids by X-FEM. *Finite Elem. Anal. Des.*, **69**, 19-36.

Bui, Q.T., Khosravifard, A., Zhang, C.Z., Hematiyan, M.R. and Golub, M.V. (2013) Dynamic analysis of sandwich beams with functionally graded core using a truly meshfree radial point interpolation method. *Eng Struct.*, **47**, 90-104.

Bui, Q.T., Vo, Q.D., Zhang, Ch. and Nguyen, D.D. (2014) A consecutive-interpolation quadrilateral element (CQ4): Formulation and applications. *Finite Elem. Anal. Des.*, **84**,14-31.

Bui, Q.T. (2015) Extended isogeometric dynamic and static fracture analysis for cracks in piezoelectric materials using NURBS. *Comput. Methods Appl. Mech. Engrg.*, **295**, 470-509.

Bui, Q.T., Hirose, S., Zhang, Ch., Rabczuk, T., Wu, C.T., Saitoh, T. and Lei, J. (2016) Extended isogeometric analysis for dynamic fracture in multiphase piezoelectric/piezomagnetic composites. *Mech Mater.*, **97**, 135-1693.

Carloni, C., Piva, A. and Viola, E. (2003) An alternative complex variable formulation for an inclined crack in an orthotropic medium. *Eng. Fract. Mech.*, **70**, 2033-2058.

Carpinteri, A. and Monetto, I. (1990) Snap-back analysis of fracture evolution in multi-cracked solids using boundary element method. *International Journal of Fracture*, **98**, 225-241.

Cruse, T.A. and Swedlow, J.L. (1971) Interactive program for analysis and design problems in advanced composites. Technical Report, Carnegie-Mellon University.

Cryer, C.W. (1963) A comparison of the three-dimensional consolidation theories of Biot and Terzaghi. *The Quarterly Journal of Mechanics and Applied Mathematics*, **16**(4), 401-412.

Dineva, P., Rangelov, T. and Gross, D. (2005) BIEM for 2D steady-state problems in cracked anisotropic materials, *Engng Anal Bound Elem*, **29**, 689-698.

Duarte, C.A. and Oden, J.T. (1996) An H-p adaptive method using clouds, *Comput Methods Appl Mech Eng*, **139**, 237-262.

Erdogan, F. and Sih, G.C. (1963) On the crack extension in plates under plane loading and transverse shear. *Journal of Basic Engineering*, **85**, 519-527.

Ewalds, H. and Wanhill, R. (1989) Fracture Mechanics; Edward Arnold: *New York*, *USA*.

Fei, L., Liqiang, Z., Pingli, L., Zhifeng, L., Nianyin, L. and Peishan, Wang. (2015) An extended finite element model for fluid flow in fractured porous media. *Mathematical Problems in Engineering*, 1-10, Article ID 604212.

Fries, T.P. and Belytschko, T. (2010) The extended/generalized finite element method: An overview of the method and its applications. *Int. J. Numer. Meth. Eng.*, **84**,253-304.

Fries, T.P. (2008) A corrected XFEM approximation without problems in blending elements. *Int. J. Numer. Meth. Eng.*, **75**,503-532.

Felipe, G.S., Zhang, Ch. and Saez, A. (2008) A two-dimentional time-domain boundary element method for dynamic crack problems in anisotropic solids, *Eng. Fract. Mech*., **75**, 1412-1430.

Gifford, Jr. L.N. and Hilton. P.D. (1978) Stress intensity factors by enriched finite elements. *Eng. Fract. Mech*., **10**,485-496.

Hattori, G., Rojas, R., Saez, A. and Sukumar, N. (2012) New anisotropic crack-tip enrichment functions for the extended finite elment method, *Comput Mecc*., **50**, 591-601.

Hematiyan, M. R., Khosravifard, A. and Bui, Q.T. (2013) Efficient evaluation of weakly/strongly singular domain integrals in the BEM using a singular nodal integration method. *Eng. Anal. Bound. Elem*., **37**, 691-698.

Irwin, G.R. (1957) Analysis of stresses and strains near the end of a crack transversing a plate. *Journal of Applied Mechanics*, *Transactions ASME*, **24**, 361-364.

Jacob, F. and Belytschko, T. (2007) A first course in finite elements. *John Wiley & Sons, Ltd, England*.

Kang, Z.Y., Bui, T.Q., Nguyen, D.D., Saitoh, T. and Hirose, S. (2015) An extended consecutive-interpolation quadrilateral element (XCQ4) applied to linear elastic fracture mechanics. *Acta Mech.*, **226**, 3991-4015.

Kang, Z.Y., Bui, T.Q., Saitoh, T. and Hirose, S. (2017) Quasi-static crack propagation simulation by an enhanced nodal gradient finite element with different enrichments. *Theor. Appl. Fract. Mech.*, **87**, 61-77.

Kitagawa, H. and Yuuki, R. (1979) A fracture mechanics approach to high-cycle fatigue crack growth under in-plane biaxial loads. *Fatigue Fract. Eng. M.*, **2**,195-206.

Kumar, S., Singh, I.V. and Mishra, B.K. (2015) A homogenized XFEM approach to simulate fatigue crack growth problems. *Comput. Struct.*, **150**, 1-22.

Kumar, S., Singh, I.V., Mishra, B.K. and Singh, A. (2016) New enrichments in XFEM to model dynamic crack response of 2-D elastic solids. *Int J Impact Eng.*, **87**, 198-211.

Kwon, Y.W. and Akin, J.E. (1989) Development of a derivative singular element for application to crack propagation problems. *Comput. Struct*, **31**,467-471.

Khoei, R.A. (2015) Extended Finite Element Method – Theory and Applications. *John Wiley & Sons, Ltd, United Kingdom*.

Lamb, A.R., Gorman, G.J. and Elsworth, D. (2013) A fracture mapping and extended finite element scheme for coupled deformation and fluid flow in fractured porous media. *Int. J. Numer. Anal. Meth. Geomech.*, **37**, 2916-2936.

Lee, J., Choi, S-U and Cho, W. (1999) A comparative study of dual-porosity model and discrete fracture network model. *KSCE Journal of Civil Engineering*, **3**(2), 171-180.

Lee, Y.J. and Freund, L.B. (1990) Fracture initiation due to asymmetric impact loading of an edge cracked plate. *ASME Journal of Applied Mechanics.*, **57**, 104-111.

Lewis R.W. and Schrefler B.A. (1998) Finite element method in the static and dynamic deformation and consolidation of porous media. *University of Wales Swansea, UK.*

Liu, P., Bui, Q.T., Zhang, Ch., Yu, T.T., Liu, G.R. and Golub, M.V. (2012) The singular edge-based smoothed finite element method for stationary dynamic crack problems in 2D elastic solids. *Comput. Meth. Appl. Mech. Eng.*, **233-236**, 68-80.

Li, C.X., Yao, T.Y., He, X.H. and Zhou, C.Y. (2017) Stress analysis for the orthotropic pressurized structure of the cylindrical shell and spherical head. *Thin Wall Struct*, **111**, 29-37.

Lowerey, M.J. (1993) Elasticity/Strip solutions for orthotropic plate systems: static and dynamic case studies. *Thin Wall Struct*, **15**, 65-79.

Mandel, J. (1953) Consolidation des sols. *Geotechnique*, **3**(7), 287-299.

Mars, J., Wali, M., Jarraya, A., Dammak, F. and Dhiab, A. (2015) Finite element implementation of an orthotropic plasticity model for sheet metal in low velocity impact simulations, *Thin Wall Struct*, **89**, 93-100.

Melenk, J.M. and Babuska, I. (1996) The partition of unity finite element method: basic theory and applications. *Comput. Methods Appl. Mech. Engrg.*, **139**, 289-314.

Menouillard, T. and Belytschko, T. (2010) Dynamic fracture with meshfree enriched XFEM, *Acta Mech*, **213**, 53-69.

Miranda, A.C.O., Meggiolaro, M.A., Castro, J.T.P., Martha, L.F. and Bittencourt, T.N. (2002) Fatigue crack propagation under complex loading in arbitrary 2D geometries. In: Braun AA, McKeighan PC, Lohr RD, editors. Applications of Automation Technology in Fatigue and Fracture Testing and Analysis, **4**. *ASTM STP 1411*, 120-46.

Miranda, A.C.O., Meggiolaro, M.A., Castro, J.T.P., Martha, L.F. and Bittencourt, T.N. (2003) Fatigue life and crack path predictions in generic 2D structural components. *Eng. Fract. Mech.*, **70**, 1259-1279.

Moës, N., Dolbow, J. and Belytschko, T. (1999) A finite element method for crack growth without remeshing. *Int. J. Numer. Meth. Eng.*, **46**, 131-150.

Mohammadi, S. (2008) Extended finite element method for fracture analysis of structures. *Blackwell publishing Ltd, UK.*

Muskhelishvili, N. I. (1977) Some basic problems on the mathematical theory of elasticity. *Springer Science & Business Media, New York.*

Natarajan, S., Chakraborty, S., Ganapathi, M. and Subramanian, M. (2014) A parametric study on the buckling of functional graded material plates with internal discontinuities using the partition of unity method. *Eur. J. Mech. A. Solids.*, **44**, 136-147.

Nguyen, T.N., Bui, Q.T., Zhang, C.Z. and Truong, T.T. (2014) Crack growth modeling in elastic solids by the extended meshfree Galerkin radial point interpolation method. *Eng Anal Bound Elem*., **44**, 87-97.

Nguyen, N.T., Bui, T.Q. and Truong, T.T. (2016) Transient dynamic fracture analysis by an extended meshfree method with different crack-tip enrichments. *Meccanica*, 1-28.

Nobile, L. and Carloni, C. (2005) Fracture anslysis for orthotropic cracked plates. *Comp. Struct*., **68**, 285-293.

Ooi, E.T., Man, H., Natarajan, S. and Song, C. (2015) Adaptation of quadtree meshes in the scaled boundary finite element method for crack propagation modelling. *Eng. Fract. Mech*., **144**, 101-117.

Osher, S. and Sethian, J.A. (1988) Fronts propagating with curvature-dependent speed: algorithms based on Hamilton-Jacobi formulations. *Journal of Computational Physics*, **79**(1), 12-49.

Phongthanapanich, S. and Dechaumphai, P. (2004) Adaptive Delaunay triangulation with object-oriented programming for crack propagation analysis. *Finite Elem. Anal. Des*., **40**, 1753-1771.

Piva, A., Viola, E. and Tornabene, F. (2005) Crack propagation in an orthotropic medium with coupled elastodynamic properties. *Mechanics Research Communications*, **32**, 153-159.

Racz, D. and Bui, Q.T. (2012) Novel adaptive meshfree integration techniques in meshless methods. *Int. J. Numer. Methods Eng*, **90**, 1414-1434.

Rice, J.R. (1968) A path independent integral and the approximate analysis of strain concentration by notches and cracks. *Journal of Applied Mechanics*. *Transactions ASME*, **35**(2), 379-386.

Roscoe, K.H. and Poorooshasb, H.B. (1963) A theoretical and experimental study of strains in triaxial compression tests on normally consolidated clays. *Geotechnique*, **13**(1), 12-34.

Rubio-Gonzalez, C. and Manzon, J.J. (1999) Response of finite cracks in orthotropic materials due to concentrated impact shear load. *Journal of Applied Mechanics (ASME)*, **66**, 485-491.

Saboori, B., Ayatollahi, M.R., Torabi, A.R. and Berto, F. (2016) Mixed mode I/III brittle fracture in round-tip V-notches. *Theor. Appl. Fract. Mech*., **83**, 135-151.

Shan, C.L. and Yi, Y.H. (2017) An experimental and numerical study on the behavior of a continuous orthotropic bridge deck with sandwich construction, *Thin Wall Struct*, **111**, 138-144.

Sharma, K., Bui, Q.T., Zhang, C.Z. and Bhargava, R.R. (2013) Analysis of a subinterface crack in piezoelectric biomaterials with the extended finite element method. *Eng. Fract. Mech.*, **104**, 114-139.

Shi, L., Yu, T.T. and Bui, Q.T. (2015) Numerical modelling of hydraulic fracturing in rock mass by XFEM. *Soil Mechanics and Foundation Engineering.*, **52**, 74-83.

Sih,G.C., Paris, P. and Irwin, G. (1965) On cracks in rectilinearly anisotropic bodies. *International Journal of Fracture Mechanics*, **1**(3), 189-203.

Sih, G.C. (1973) Handbook of stress intensity factors for researchers and engineers. *Lehigh University, Bethlehem, PA, USA.*

Sih, G.C. (1974) On cracks in rectilinearly anisotropic bodies. *International Journal of Fracture Mechanics*, **1**(3), 189-203.

Song, C. and Wolf, J.P. (1997) The scaled boundary finite-element method-alias consistent infinitesimal finite-element cell method – for elastodynamics. *Comput. Methods Appl. Mech. Engrg.*, **147**, 329-355.

Song, S.H. and Paulino, G.H. (2006) Dynamic stress intensity factors for homogeneous and smoothly heterogeneous materials using the interaction integral method. *Int. J. Solids Struct.*, **43**, 4830-4866.

Srawley, J.E. (1976) Wide range stress intensity factor expresssions for ASTM E 399 standard fracture toughness specimens. *Int. J. Fract.*, **12**,475-476.

Stazi, F.L., Budyn, E., Chessa, J. and Belytschko, T. (2003) An extended finite element with higher-order elements for curved cracks. *Comput. Mech.*, **31**,38-48.

Stolarska, M., Chopp, D.L., Moës, N. and Belytschko, T. (2001) Modelling crack growth by level sets in the extended finite element method. *International Journal for Numerical Methods in Engineering*, **51**, 943-960.

Strouboulis, T., Babuska, I. and Copps, K. (2000) The design and analysis of the generalized finite element method. *Comput. Methods Appl Mech Engrg.*, **181**, 43-96.

Tabbara, M.R. and Stone, C.M. (1998) A computational method for quasi-static fracture. *Comput. Mech.*, **22**, 203-210.

Tanaka, S., Suzuki, H., Ueda, S. and Sannomaru, S. (2015) An extended wavelet galerkin method with a high-order B-spline for 2D crack problems. *Acta Mech*, **226**, 2159-2175.

Tanaka, S., Suzuki, H., Sadamoto, S., Imachi, M. and Bui, Q.T. (2015) Analysis of cracked shear deformable plates by an effective meshfree plate formulation. *Eng. Fract. Mech.*, **144**, 142-157.

Tan, A., Hirose, S., Zhang, Ch. and Wang, C.Y. (2005) A time-domain BEM for transient wave scattering analysis by a crack in anisotropic solids. *Engng Anal Bound Elem.*, **29**, 610-623.

Tan, A., Hirose, S. and Zhang, Ch. (2005) A time-domain collocationi-Galerkin BEM for transient dynamic crack analysis in anisotropic solids. *Engng Anal Bound Elem*, **29**, 1025-1038.

Thomas, J.C. and Van, A.L. (2013) An exact solution for inflated orthotropic membrane tubes. *Thin Wall Struct*, **67**, 116-120.

Tran, N.H. and Ravoof, A. (2007) Coupled fluid flow through discrete fracture network: a novel approach. *International Journal of Mathematics and Computers in Simulation*, **1**(3), 295-299.

Ventura, G., Xu, J.X. and Belytschko, T. (2002) A vector level set method and new discontinuity approximation for crack growth by EFG. *Int J Numer Meth Engng.*, **54**, 923-944.

Wu, J. and Cai, Y.C. (2014) A partition of unity formulation referring to the NMM for multiple intersecting crack analysis. *Theor. Appl. Fract. Mech.*, **72**, 28-36.

Wu, S.C., Zhang, W.H., Peng, X. and Miao, B.R. (2012) A twice-interpolation finite element method (TFEM) for crack propagation problems. *Int. J. Comput. Meth.*, **9**, 1250055.

Xia, L., Haim, W. and Jacob, F. (2012) A new crack tip enrichment function in the extended finite element method for general inelastic materials. *Int J Mult Comp Eng.*, **10**(4), 343-360.

Yang, Y.T., Tang, X.H. and Zheng, H. (2014) A three-node triangular element with continuous nodal stress. *Comput. Struct.*, **141**,46-58.

Yin, S.H., Yu, T.T., Bui, Q.T., Xia, S.F. and Hirose, S. (2015) A cutout isogeometric analysis for thin laminated composite plates using level sets. *Compos. Struct.*, **127**, 152-164.

Yu, T.T., Bui, Q.T., Liu, P., Zhang, Ch and Hirose, S. (2015) Interfacial dynamic impermeable cracks analysis in dissimilar piezoelectric materials under coupled electromechanical loading with the extended finite element method. *Int. J. Solids Struct.*, **67-68**, 205-218.

Yu, T.T., Bui, Q.T., Liu, P. and Hirose, S. (2016) A stabilized discrete shear gap extended finite element for the analysis of cracked Reissner-Mindlin plate vibration problems involving distorted mesh. *Int. J. Mech. Mater. Des*., **12**, 85-107.

Yu, T.T., Bui, Q.T., Yin, S.H., Doan, H.D., Wu, C.T., Do, V.T. and Tanaka, S. (2016) On the thermal buckling analysis of functionally graded plates with internal defects using extended isogeometric analysis. *Compos Struct*., **136**, 684-695.

Zhang, X.D. and Bui, Q.T. (2015) A fictitious crack XFEM with two new solution algorithms for cohesive crack growth modeling in concrete structures. *Eng. Comput*., **32**, 473-497.

Zheng, C., Wu, S.C., Tang, X.H. and Zhang, J.H. (2010) A novel twice-interpolation finite element method for solid mechanics problems. *Acta Mech. Sin*., **26**(2), 265-278.